X-RAY DEBYE-WALLER FACTOR MEASUREMENTS OF HELIUM CRYSTALS

BY

DOHN ALEXANDER ARMS

B.S., University of Florida, 1993
M.S., University of Illinois at Urbana-Champaign, 1995

THESIS

Submitted in partial fulfillment of the requirements
for the degree of Doctor of Philosophy in Physics
in the Graduate College of the
University of Illinois at Urbana-Champaign, 1999

Urbana, Illinois

X-RAY DEBYE-WALLER FACTOR MEASUREMENTS OF HELIUM CRYSTALS

Dohn Alexander Arms, Ph.D.
Department of Physics
University of Illinois at Urbana-Champaign, 1999
Dr. Ralph O. Simmons, Advisor

Helium crystals have long been studied as prototype quantum solids, due to the large zero-point motion of the atoms. This large motion causes the harmonic approximation of non-interacting phonons in the crystal to become severely strained, and the multi-phonon processes present have been hard to account for in theory and computation. The measurement of the mean square atomic deviation of helium can give insight into its anharmonic nature.

X-ray synchrotron radiation was used to measure Debye-Waller factors of helium. Helium crystals were grown in a beryllium cell at a high pressure and low temperature, through the use of a refrigerator. Both ^{3}He and ^{4}He crystals in the hcp and fcc phases were studied. The range of molar volumes used for investigating ^{3}He and ^{4}He crystals was 11.52–12.82 cm^3 and 10.95–12.13 cm^3, respectively. The temperature ranges used were 11.5–18.2 K and 12.0–20.3 K, respectively. The Debye-Waller measurements were used to determine the mean square atomic deviation, the equivalent Debye temperature, and the Lindemann ratio for each measurement.

The measured results agree well with computational values, made using path integral Monte Carlo methods. The Lindemann ratios were around 0.19 for both isotopes, with the ^{3}He values being larger at similar densities. A ^{3}He-^{4}He mass-scaling factor of $\sqrt{4/3}$ for the equivalent Debye temperature for the measured Debye-Waller factor was observed. This Debye temperature falls with increasing temperature, contrary to what would be expected for a quasi-harmonic model, most likely due to multi-phonon processes being present in the crystals.

Acknowledgments

I would like to thank my advisor, Professor Ralph O. Simmons, for his encouragement and support during my research. His tireless research into basic physics has been inspiring, and I particularly enjoyed the many discussions we have had, about both physics and things in general. I am honored to be his final doctoral student.

Without my family, this thesis would not have been possible. They have been a constant source of both encouragement and support, and this thesis is dedicated to them.

I have made many friends as a graduate student, and all have been instrumental in my seeing graduate school through. I would like to thank Tara Cameron, Adam & Deb Abeyta, Balijeet Bains, and Raj Shah for being my closest friends and helping me in my (many) times of need. I would also like to thank Alijeet Bains, Phil Hession, Craig Milling, Markus Schwoerer-Böhning, Christian Seyfert, Harald Sinn, and Chitra Venkataraman for their friendship and help.

I would like to thank Al Macrander for making my stay at the APS possible and giving me encouragement. For an interesting first summer of research, I would also like to thank Jack Mochel.

I am also very grateful for all the help George Srajer and the rest of 1-BM gave me during my beamtimes on their beamline. I would like to thank the staff of the MRL business office and machine shop, as it was always a pleasure to work with them.

I would like to thank our colleagues, Erik Draeger and David Ceperley, who made PIMC calculations corresponding to my samples, and also gave me access to their paper before its publication.

This research was supported by the U. S. Department of Energy, Basic Energy Sciences, Division of Materials Sciences, under contract DOE-DE-FG02-96ER45439.

Contents

Chapter

Chapter 1

Introduction

1.1 The Quantum Nature of Helium Crystals

Helium has been a very interesting element to study over the years, for many reasons. A helium atom is simple from a structure standpoint, with only two electrons (and protons); the two electrons compose a filled, spherically symmetric electronic shell, making it very unreactive with other atoms. As a gas, the formation of diatomic molecules is limited by mass-action considerations, and no excited vibrational states have been identified [1]. It has either one or two neutrons, and both isotopes are stable. From a quantum mechanical standpoint, it is second only to the hydrogen atom in its simplicity. However, when it comes to forming liquids or crystals, helium becomes one of the most difficult elements to understand and predict. The discussion of crystals is strongly influenced by Dobbs [2].

The phase diagrams of the two isotopes are very different at lower pressure and temperature, primarily in the bcc phase. The ^{4}He phase diagram has a very small region of bcc phase that is bounded on all sides by either hcp phase solid or fluid; the ^{3}He phase diagram has a much larger region of bcc phase, only partially surrounded by hcp phase solid and fluid, as it extends to zero temperature. These differences of the phase diagrams are due to the zero-point energy of the nuclei and the differing atomic masses.

In the case of liquids, the enormous variety of phenomena is remarkable [3]. For each isotope, there are both normal liquids and also superfluid phases, persistent to absolute zero at pressures below tens of atmospheres.

In the case of solids, the main complication is the zero-point energy of the atoms. The basic theory of phonons in solids is founded on the principle that the potential applicable to an individual atom, due to the surrounding atoms, is parabolic in nature to a good approximation; this is known as the harmonic approximation. The atoms vibrate, which comes from the zero-point energies of

the atoms and the thermal energy of the crystal. The harmonic approximation works as long as the ratio of atomic vibrational amplitude to interatomic distance is kept small; a quantity of this type normally used for this is the Lindemann ratio,

$$\text{Lindemann Ratio} \equiv \frac{\sqrt{\langle {u_3}^2 \rangle}}{r}\,, \tag{1.1}$$

where $\langle {u_3}^2 \rangle$ is the three-dimensional mean square deviation of the atom from its equilibrium position, and r is the nearest atomic neighbor distance. In usual solids, this ratio is a few percent.

The atoms of a noble gas have closed electronic shells and a spherical symmetry. The crystals form from the weak van der Waals attraction, where two atoms are attracted to each other by the dipoles induced in the other's electronic distribution, which goes as r^{-6} where r is the distance between the two atoms. This attraction is countered by the repulsion of the two atoms' electronic clouds, as electrons of the same spin can't occupy the same position due to the Pauli exclusion principle. A model used to express this potential is the Lennard-Jones potential,

$$\Phi(r) = 4\epsilon \left[\left(\frac{\sigma}{r}\right)^{12} - \left(\frac{\sigma}{r}\right)^{6} \right], \tag{1.2}$$

where σ represents the "hard core" radius of the atom and ϵ represents the binding energy of the pair. For helium, Aziz et al. determined these parameters as $\sigma = 2.556$ Å and $\epsilon = 10.22\ k_{\mathrm{B}}\mathrm{K}$ [4]. A graph of the Lennard-Jones potential for the noble gases is in Fig. 1.1.

A measure of the quantum nature of a crystal is the reduced de Broglie wavelength [6],

$$\Lambda^* = \frac{h}{\sigma\sqrt{m\epsilon}}\,. \tag{1.3}$$

This dimensionless parameter, used to express the zero-point energy, is larger for crystals that are more quantum in nature. Λ^* for helium is 3.08 (^{3}He) and 2.68 (^{4}He). For comparison, the value for Ne is 0.594 and for Ar is 0.186 [5].

The molar volume of the crystal is also affected by the zero-point motion, which tends to expand the crystal. If the Lennard-Jones potential is used to compute the molar volume of a helium crystal, while ignoring the zero-point energy, it would have a value of 12 cm^3 at zero pressure. However, helium doesn't even solidify unless an external pressure is applied. If the lowest pressure needed

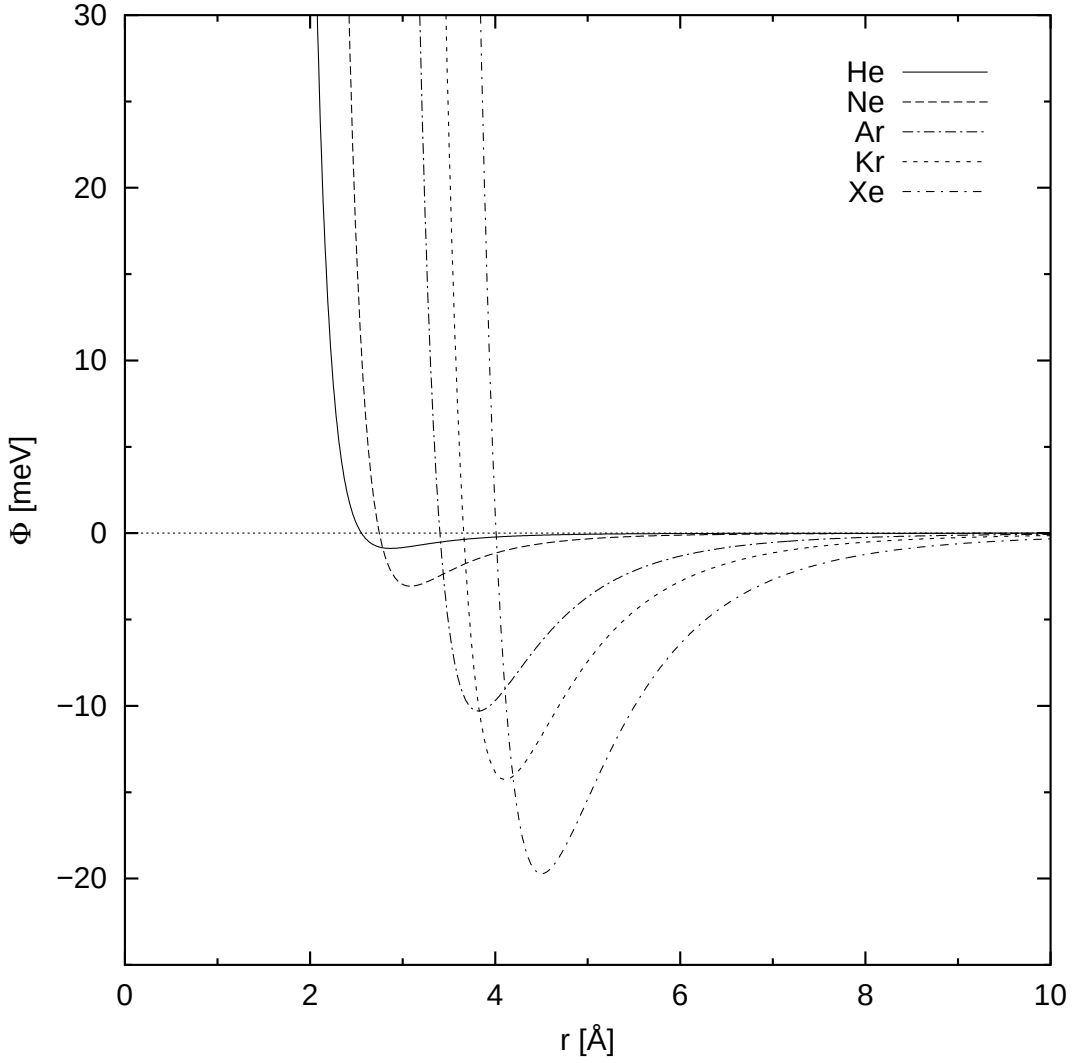

Figure 1.1: Lennard-Jones potentials for He and the other noble gases. The L-J potential is $\Phi(r) = 4\epsilon[(\sigma/r)^{12} - (\sigma/r)^6]$, where r is the internuclear separation. The values for ϵ and σ are from Aziz et al. [5]

to create a crystal is used, the two different isotopic crystals will have a molar volumes of 25 cm^3 (^{3}He) and 21 cm^3 (^{4}He), which is still much higher than expected. If a reduced atomic volume is introduced [6],

$$V^* = \frac{V}{N_A \, \sigma^3} \, , \tag{1.4}$$

where V is the measured molar volume, it can be used to indicate how much larger the molar volume is, compared to a classically expected value. The resulting V^* values for helium are roughly 2.6 (^{3}He) and 2.1 (^{4}He), while they are close to unity for Ar and Ne.

This expansion can be shown, using the harmonic oscillator potential and the quantum mechanical solution. For a particle in a harmonic oscillator [7], the zero-point energy is $\hbar\omega/2$, where ω is the quantum frequency. This frequency has an inverse mass dependence, $\omega \propto m^{-1/2}$, making lighter atoms have a larger zero-point energy. This larger zero-point energy in turn results in a larger mean square deviation of the particle inside the potential. This deviation, in terms of a crystal, will cause the atoms, with their encompassing electronic distributions, to push each other away from the classical distances, resulting in an expansion of the crystal from its classical value. The lighter the atom, the larger the crystal expansion. For crystals that have a weak binding energy, such as the noble gases with the van der Waals force, this expansion is even more pronounced. Since helium is the lightest noble gas, its volume is expanded more than any other elemental crystal.

The large zero-point energy of the atoms causes significant overlap of the electronic wave functions. Helium has a spherical, filled outer shell, making such an overlap repulsive due to the Pauli exclusion principle. The Lennard-Jones potential, useful as a qualitative tool, falls short in several respects. This potential has too stiff of a repulsive term for helium. This potential also does not give a good fit to empirical data. Several different potentials have been used, but the best description is the HFD (Hartree-Fock plus damped dispersion) potential, proposed by Aziz et al. [4, 5].

If for an assumed static helium crystal of a sufficiently large actual molar volume, the potential applicable to an atom due to all the surrounding atoms is summed from the individual pair potentials, the result is a local maximum at the supposed equilibrium site (which is explained in more detail in several books [8, 9]). This "bump" in the middle makes this total potential very anharmonic, especially since the atom would be at an unstable site. If conventional harmonic Born-von Kármán theory is applied to the potential, the resulting phonon frequencies are imagi-

nary for the entire Brillouin zone [10]. This failure is not borne out by experiment, since inelastic scattering using both neutrons and X-rays has been used to directly measure the dispersion curves of the phonons in both ^{3}He and ^{4}He (discussed in Chapter 5). The problem comes from the model assuming that the atoms are static at the equilibrium positions, which is unrealistic since there is a large zero-point energy for the atoms. If the molar volume decreases, this bump disappears, and the total potential becomes less anharmonic. Helium at high pressures and the other noble gases are in this regime.

The method developed by Born and Hooton to take the anharmonic well and the large zero-point energy into account was SCP (self-consistent phonon) theory, which is described fully in several books [8, 9, 11]. With this method, the atom is represented by a distribution, not by a point. It discards the total potential as calculated from a static lattice of atoms, and calculates the total potential as coming from atoms with an atomic distribution identical to that of the atom in question. A trial wave function with adjustable parameters is used with some starting values, and these values are refined by use of a variational principle. Such models work well for the heavier noble gases, but they begin to break down with helium [8]. These models have been produced for helium with various degrees of self-consistency, but they generally address some specific phonon issue, such as heat capacity, thermal expansion, etc. None have been applied to overall Debye-Waller measurements.

Other computational techniques have been developed to compute various properties of quantum solids. These are GFMC (Green function Monte Carlo) [12] applicable to the ground state, and PIMC (path integral Monte Carlo) [13] applicable at finite temperatures. PIMC computations provide the best theoretical agreement to the average kinetic energy of a nucleus measured with neutron Compton scattering [14]. Recent PIMC work, done in conjunction with this thesis, has shown that larger sample sizes than previously used in calculations are needed in order to agree with direct $\langle u^2 \rangle$ measurements [15].

1.2 Phase Diagram

Solid helium exists in three different forms for both ^{3}He and ^{4}He: hcp, bcc, and fcc. The actual form of the phase diagrams differs substantially at low pressures and temperatures. A listing of the measured values discussed in this section is in Appendix D.2.

For ^{3}He, there is a substantial region of bcc phase at the lowest pressures of the solid. At higher pressures, above the bcc-hcp-liquid triple point, there exists a huge region of hcp phase. At higher pressures, above the hcp-fcc-liquid triple point, there exists a narrow fcc phase that widens as pressure increases.

For ^{4}He, the phase is hcp at the lowest pressures of the solid. A very narrow region of bcc phase exists at slightly higher pressures, extending from one hcp-bcc-liquid triple point to another. At higher pressures, a region of fcc phase similar to that of ^{3}He exists, but it has been seen recently that this fcc region closes in upon itself at very high pressures [16], giving two hcp-fcc-liquid triple points.

The hcp-fcc transition for both isotopes are similar in shape and nature. At the hcp-fcc-liquid triple point, the transition is sharp, but as the pressure increases, a hysteresis in the phase transformation appears and becomes more pronounced with rising pressure. After an initial curvature in this transition curve above the triple point, the curve becomes fairly straight within the region of hysteresis for the pressures studied in this thesis.

A graph of the phase diagrams for both ^{3}He and ^{4}He, with the pressure and temperature ranges applicable to this thesis, is given in Fig. 1.2. The melting curves for ^{3}He and ^{4}He come from Mills and Grilly [17]. The approximate fcc-hcp transition line for ^{3}He comes from Ryschkewitsch et al. [18], while the line for ^{3}He comes from Franck [19].

1.3 Experimental Overview

Using X-rays it is possible to measure the mean squared atomic displacement, $\langle u^2 \rangle$, for a helium crystal directly, as well as the nearest neighbor distances, enabling a Lindemann ratio to be found. The $\langle u^2 \rangle$ is found by means of the Debye-Waller factor, M, which gives a relationship for the scattered intensity as

$$\ln\left(\frac{I}{I_0}\right) \propto -2M(Q) \equiv -Q^2\langle u^2 \rangle\,, \tag{1.5}$$

where I_0 and I are the initial and scattered intensities, and Q is the magnitude of the change of wave vector between an incoming photon and a scattered photon.

For a crystal at a constant temperature, (I/I_0) is measured for several different reflections of differing Q values. A linear relation between $\ln(I/I_0)$ and Q^2 should be seen, where the negative

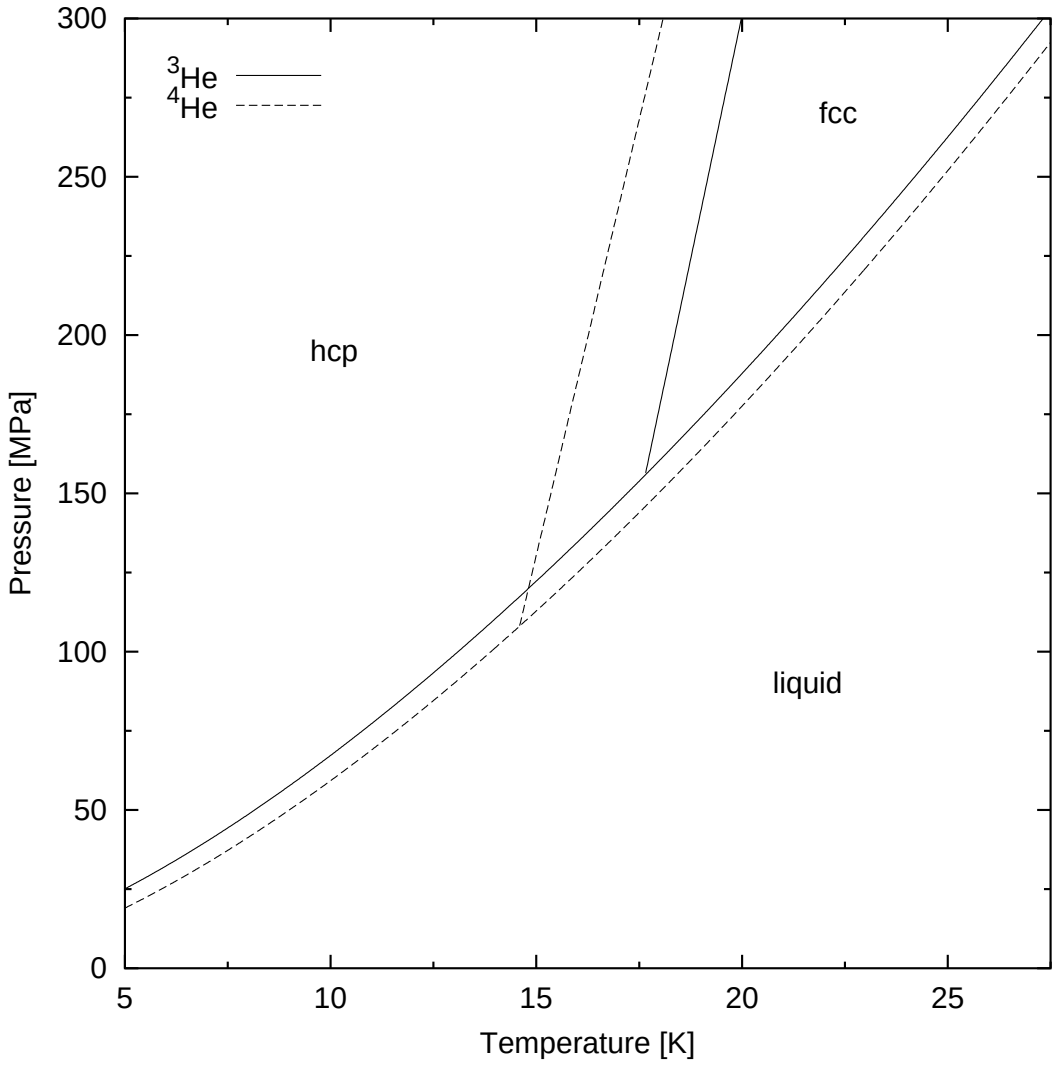

Figure 1.2: Phase diagram of both ^{3}He and ^{4}He for the pressure and temperature ranges applicable to this thesis. The melting curves for ^{3}He and ^{4}He come from Mills and Grilly [17]. The hcp-fcc transition lines are shown schematically for ^{3}He [18] and ^{4}He [19]. The real solids show a hysteresis in this phase transformation, which increases with increasing pressure. Also, very near the respective triple points the actual texture of a given sample depends upon the thermal and pressure history of the sample. The triple point for ^{3}He is 17.8 K and 158.0 MPa, while for ^{4}He it is 14.9 K and 111.6 MPa.

of the slope is the $\langle u^2 \rangle$ value for the crystal. The Debye temperature is calculated by means of

$$T\langle u^2 \rangle = \frac{3\hbar^2}{mk_{\rm B}} \left[\frac{1}{4x} + \frac{1}{x^3} \int_0^x \frac{\epsilon \, d\epsilon}{e^\epsilon - 1} \right] \qquad \text{and} \qquad x \equiv \frac{\Theta_M}{T} \, . \tag{1.6}$$

The temperature dependence of the Debye temperature can be found by taking Debye-Waller measurements for the same crystal at different temperatures.

The goals of this thesis are fourfold. One is to carry out the first direct measurements of the Debye-Waller factor for ^{3}He, in both hcp and fcc phases, resulting in values for the mean square atomic deviation, $\langle u^2 \rangle$, and the corresponding Debye temperature, Θ_M. The next goal is to make similar direct measurements for ^{4}He, for comparison, in both the hcp and fcc phases. Temperature dependencies of both $\langle u^2 \rangle$ and Θ_M are to be studied for both ^{3}He and ^{4}He. The last goal is to compare the measured values to values computed using path integral Monte Carlo techniques.

References

[1] Y. Xu, W. Jaeger, and M. C. L. Gerry, J. Chem. Phys. **100**, 4174 (1994).

[2] E. R. Dobbs, *Solid Helium Three* (Clarendon, Oxford, 1994).

[3] J. Wilks and D. S. Betts, *An Introduction to Liquid Helium* (Clarendon, Oxford, 1987).

[4] R. A. Aziz, A. R. Janzen, and M. R. Moldover, Phys. Rev. Lett. **74**, 1586 (1995).

[5] R. A. Aziz, A. R. Janzen, and R. O. Simmons, in *Encyclopedia of Applied Physics*, edited by G. L. Trigg (VCH, New York, 1996), Vol. 16, p. 71.

[6] J. de Boer, Physica **14**, 139 (1948).

[7] S. Gasiorowicz, *Quantum Physics* (Wiley, New York, 1974).

[8] T. R. Koehler, in *Dynamical Properties of Solids*, edited by G. K. Horton and A. A. Maradudin (North-Holland, New York, 1975), Vol. 2, p. 1.

[9] H. R. Glyde, *Excitations in Liquid and Solid Helium* (Clarendon, Oxford, 1994).

[10] F. W. de Wette and B. R. A. Nijboer, Phys. Lett. **18**, 19 (1965).

[11] N. R. Werthamer, in *Rare Gas Solids*, edited by M. L. Klein and J. A. Venables (Academic Press, New York, 1976), Vol. 1, p. 265.

[12] P. A. Whitlock and R. M. Panoff, Can. J. Phys. **65**, 1409 (1987).

[13] D. M. Ceperley, Rev. Mod. Phys. **67**, 279 (1995).

[14] R. A. Blasdell, Ph.D. thesis, University of Illinois at Urbana-Champaign, 1992.

[15] E. Draeger and D. M. Ceperley, Bull. Am. Phys. Soc. **44**, 655 (1999), to be published.

[16] P. Loubeyre, R. LeToullec, J. P. Pinceaux, H. K. Mao, J. Hu, and R. J. Hemley, Phys. Rev. Lett. **71**, 2272 (1993).

[17] R. L. Mills and E. R. Grilly, Phys. Rev. **99**, 480 (1955).

[18] M. G. Ryschkewitsch, J. P. Franck, B. J. Duch, and W. B. Daniels, Phys. Rev. B **26**, 5276 (1982).

[19] J. P. Franck, Phys. Rev. B **22**, 4315 (1980).

Chapter 2

Theory

2.1 X-ray Diffraction

Extensive use of X-ray diffraction has been made with this experiment. This section is strongly influenced by Warren [1].

2.1.1 Elastic Scattering

Elastic X-ray diffraction is very similar to interference patterns using visible light and a periodic grating, and several analogies can be made between the two.

In the case of visible light, photons are scattered by a periodic grating, such as slits for one dimension or holes for two dimensions. On the far side of this grating, the waves from different slits combine together, and because of the periodicity of the grating, the waves interfere either constructively or destructively. This interference results in bands if a one dimensional grating was used, or in dots if a two dimensional grating was used. The higher the number of apertures in the grating, the better the resolution of the resulting peaks.

In the case of X-ray diffraction, the scatterer of the photons is the electronic distribution that surrounds the nucleus. The crystal lattice, due to its periodic nature, acts essentially as a three dimensional grating, and the elastic peaks are the resulting interference. Since the number of scatterers in a crystal is normally quite large, the peaks are very sharp.

This obviously oversimplifies elastic X-ray scattering, but it is essentially correct.

2.1.2 Bragg's Law

The most important law of X-ray diffraction is Bragg's Law. It is used to find the angle needed to find a elastic peak corresponding to a given planar spacing. There are several ways to derive this law, such as geometrical (the way Bragg formulated it), classical electrodynamical, and quantum

mechanical. It will be derived below using quantum mechanics.

Scattering occurs since the electrons of the atom couple with the electromagnetic field of photons. Since the scattering is between high energy photons and a weakly coupling electronic potential, the Born approximation allows the scattering to be described as a change of state for the photons, with the asymptotic states represented as plane waves, $\Psi(\mathbf{r}) \propto e^{i\mathbf{k}\cdot\mathbf{r}}$. These states are described by their wave vectors $\mathbf{k}$, with $\Psi_{\mathbf{k}}(\mathbf{r})$ representing the initial state and $\Psi_{\mathbf{k}'}(\mathbf{r})$ representing the final state.

The transition rate is described by Fermi's Golden Rule and is proportional to the square of the matrix element

$$T_{\mathbf{k}'\mathbf{k}} \equiv \langle \Psi_{\mathbf{k}'}(\mathbf{r}) | U(\mathbf{r}) | \Psi_{\mathbf{k}}(\mathbf{r}) \rangle = \int \Psi^*_{\mathbf{k}'}(\mathbf{r}) U(\mathbf{r}) \Psi_{\mathbf{k}}(\mathbf{r}) d\mathbf{r} \tag{2.1}$$

where $U(\mathbf{r})$ is the electronic potential to which the photons couple. This potential is periodic since the atoms are in a crystal structure, $U(\mathbf{r}) = U(\mathbf{r} + \mathbf{R})$ where $\mathbf{R} \equiv n_1\mathbf{a}_1 + n_2\mathbf{a}_2 + n_3\mathbf{a}_3$ is a lattice vector of the crystal. Due to the periodic nature of the electronic potential, $U(\mathbf{r})$ can be represented by a Fourier series as $U(\mathbf{r}) = \sum_{\mathbf{K}} U_{\mathbf{K}} e^{i\mathbf{K}\cdot\mathbf{r}}$, where $\mathbf{K} \equiv h\mathbf{b}_1 + k\mathbf{b}_2 + \ell\mathbf{b}_3$ is a reciprocal lattice vector of the crystal. The matrix element then becomes

$$T_{\mathbf{k}'\mathbf{k}} = \sum_{\mathbf{K}} U_{\mathbf{K}} \int e^{-i\mathbf{k}'\cdot\mathbf{r}} e^{i\mathbf{K}\cdot\mathbf{r}} e^{i\mathbf{k}\cdot\mathbf{r}} d\mathbf{r} = \sum_{\mathbf{K}} U_{\mathbf{K}} \int e^{i(\mathbf{k}+\mathbf{K}-\mathbf{k}')\cdot\mathbf{r}} d\mathbf{r}\,. \tag{2.2}$$

There is a standard definition of $\mathbf{Q} \equiv \mathbf{k}' - \mathbf{k}$ for the change of the photon's wave vector (the "crystal momentum", since $\mathbf{p} = \hbar\mathbf{k}$). This leaves

$$T_{\mathbf{k}'\mathbf{k}} = \sum_{\mathbf{K}} U_{\mathbf{K}} \int e^{i(\mathbf{K}-\mathbf{Q})\cdot\mathbf{r}} d\mathbf{r} = \sum_{\mathbf{K}} U_{\mathbf{K}} \delta_{\mathbf{K}\mathbf{Q}} = \begin{cases} U_{\mathbf{K}} & \text{if } \mathbf{Q} = \mathbf{K} \text{ for one value of } \mathbf{K} \\ 0 & \text{if } \mathbf{Q} \neq \mathbf{K} \text{ for all values of } \mathbf{K} \end{cases} \tag{2.3}$$

as the matrix element. From this, the only reflections allowed are those where $\mathbf{Q} = \mathbf{K}$, meaning that the change in the photon's wave vector needs to equal a reciprocal lattice vector. The peak in actuality is not a infinitely thin peak, since the Fourier series was formed assuming an infinitely large crystal; in reality, the finite nature of the crystal produces intensity maxima, with a finite width and height, where $\mathbf{Q} = \mathbf{K}$.

For elastic scattering, there is no change in the photon energy, so $|\mathbf{k}| = |\mathbf{k}'|$. From simple geometry, this results in $K = 2k\sin\theta$. The reciprocal lattice vector $\mathbf{K}$ is related to the interplanar distance of the direct crystal lattice, d, by $K = 2\pi n/d$. Also, $k = 2\pi/\lambda$. Combining these results in

$$2d\sin\theta = n\lambda \qquad \textbf{(Bragg's Law)} \tag{2.4}$$

where n is the order of the reflection for a given lattice spacing. The energy of the photons, E, is sometimes known, instead of the wavelength; the relation between the two is

$$\lambda = \frac{hc}{E}\,. \tag{2.5}$$

2.1.3 Scattered Intensity

The atomic form factor is an important concept that is used in X-ray diffraction. It is the amplitude of the elastic scattering of the photons from a single atom for a given $\mathbf{Q}$, in terms of electron units. It is a function whose value decreases from the total number of electrons in the atom, as $\mathbf{Q}$ increases. The decrease comes the fact that there is an electron density distribution about the nucleus, and the photons scattering from one part of the distribution can interfere destructively with photons scattering from another part of the distribution. The form factor, assuming the electron density distribution is spherical (a good approximation for helium), can be computed by

$$f = \sum_n \int_0^\infty 4\pi r^2 \rho_n(r) \frac{\sin(kr)}{kr}\, dr \tag{2.6}$$

where ρ_n is the electron density distribution for electron n of the atom.

If the scattered intensity is calculated for the static ideal model of a crystalline lattice, the result is

$$I(\mathbf{Q}) = I_e\, P(Q) \sum_{l,n} f_n(Q) e^{i\mathbf{Q}\cdot\mathbf{R}_{ln}} \sum_{l',n'} f^*_{n'}(Q) e^{-i\mathbf{Q}\cdot\mathbf{R}_{l'n'}} \tag{2.7}$$

where

$$P(Q) = \begin{cases} (1+\cos^2(2\theta))/2 & \text{unpolarized incident beam} \\ 1 & \text{horizontally polarized incident beam} \end{cases} \tag{2.8}$$

and

$$I_e = I_0 \frac{e^4}{{m_e}^2 c^4 {R_{\rm obs}}^2} \,. \tag{2.9}$$

The indices l and n together count every atom in the crystal, with l labelling the individual unit cells and n labelling each atom within the unit cell, and f_n is the form factor of atom n. $P(Q)$ is a polarization factor, with its Q dependence coming from $Q \equiv |\mathbf{Q}| = (4\pi/\lambda)\sin(\theta)$. I_e is a constant where I_0 is the intensity of the incident beam, e is the electronic charge, m_e is the mass of the electron, c is the speed of light, and $R_{\rm obs}$ is the distance from the crystal to the point of observation.

In order to solve Eq. (2.7), one assumes a crystal where the atoms are at the lattice positions $\mathbf{R} \equiv n_1\mathbf{a}_1 + n_2\mathbf{a}_2 + n_3\mathbf{a}_3$ and the crystal is finite such that $-N_i/2 < n_i \leq N_i/2$, making the total number of atoms $N = N_1 N_2 N_3$. Eq. (2.7) then becomes

$$I(\mathbf{Q}) = I_e \, P(Q) \, F(\mathbf{Q})^2 \, B(\mathbf{Q}) \tag{2.10}$$

where $F(\mathbf{Q})$ is the structure factor and

$$B(\mathbf{Q}) = \frac{\sin^2([N_1/2]\mathbf{Q}\cdot\mathbf{a}_1)}{\sin^2([1/2]\mathbf{Q}\cdot\mathbf{a}_1)} \frac{\sin^2([N_2/2]\mathbf{Q}\cdot\mathbf{a}_2)}{\sin^2([1/2]\mathbf{Q}\cdot\mathbf{a}_2)} \frac{\sin^2([N_3/2]\mathbf{Q}\cdot\mathbf{a}_3)}{\sin^2([1/2]\mathbf{Q}\cdot\mathbf{a}_3)} \,. \tag{2.11}$$

The function $B(\mathbf{Q})$ (which is nonstandard notation) peaks when the Laue condition $\mathbf{Q} = \mathbf{K}$ is satisfied for some reciprocal lattice vector $\mathbf{K}$; this maximum value of $B(\mathbf{Q})$ at the Laue condition is ${N_1}^2{N_2}^2{N_3}^2$ (or N^2). The peaks have a finite width, although they become sharper as N increases; in a normal crystal sample, N is quite large, making the Bragg peaks very sharp.

The structure factor is of the form

$$F(\mathbf{Q}) = \sum_n f_n(Q) e^{i\mathbf{Q}\cdot\mathbf{r}_n} = (\text{at Bragg reflections}) \sum_n f_n(Q) e^{2\pi i(hx_n + ky_n + \ell z_n)} \tag{2.12}$$

where the sum is over all the atoms within the unit cell, where the atoms are at positions $\mathbf{r}_n \equiv x_n\mathbf{a}_1 + y_n\mathbf{a}_2 + z_n\mathbf{a}_3$ where x_n, y_n, and z_n are all between zero and unity. The factor f_n is the form factor of the atom at position $\mathbf{r}_n$. The structure factor gives a value for any particular $(h\,k\,\ell)$ reflection, and only needs to be computed where there is more than one atom per unit cell, since $F(\mathbf{Q}) = f(Q)$ otherwise. The structure factor can cause reflections corresponding to a reciprocal lattice point to not appear; these peaks are then considered to be "forbidden".

2.1.4 Debye-Waller Factor

The above derivation assumes that the electronic distributions are perfectly periodic, which is not the case.

Crystal nuclei oscillate about their "ideal" positions, due to the quantum fluctuations of the atoms and the crystal temperature. If these oscillations are small enough that they are harmonic, this motion of the nuclei can be broken down into normal modes, called phonons. Even at absolute zero, there is still motion due to the zero-point oscillations of the nuclei; in the harmonic model, the zero-point energy of each phonon mode is $\hbar\omega/2$. The harmonic model will be assumed at this point and it will be assumed that the electron distribution follows the nuclei's position instantaneously.

Because of the presence of these oscillations, the instantaneous spacings between nuclei are not at the ideal value, even though the average value is at the lattice site $\mathbf{R}$. These small instantaneous deviations of the nuclei positions from the ideal cause the interference to be less than perfect, reducing the peak's maximum value.

The instantaneous position of a nucleus can be expressed as

$$\mathbf{r}(t) = \mathbf{R} + \mathbf{u}(t)\,, \tag{2.13}$$

where $\mathbf{u}(t)$ is the deviation of the nucleus from its lattice position $\mathbf{R}$. If this time-dependent $\mathbf{r}$ is substituted for $\mathbf{R}$ in Eq. (2.7), the result is

$$I(\mathbf{Q},t) = I_e\, P(Q) \sum_{l,n} f_n(Q) e^{i\mathbf{Q}\cdot(\mathbf{R}_{ln}+\mathbf{u}_{ln})} \sum_{l',n'} f^*_{n'}(Q) e^{-i\mathbf{Q}\cdot(\mathbf{R}_{l'n'}+\mathbf{u}_{l'n'})}\,. \tag{2.14}$$

If time averaged in order to obtain an experimentally obtained intensity, the result is

$$I(\mathbf{Q}) = I_e\, P(Q) \sum_{l,n} \sum_{l',n'} f_n(Q) f^*_{n'}(Q)\, e^{i\mathbf{Q}\cdot(\mathbf{R}_{ln}-\mathbf{R}_{l'n'})} \left\langle e^{i\mathbf{Q}\cdot(\mathbf{u_{ln}}-\mathbf{u_{l'n'}})} \right\rangle . \tag{2.15}$$

Let $\mathbf{Q}\cdot\mathbf{u}_{ln} = Q\,u_{Qln}$, where u_{Qln} is the component of $\mathbf{u}_{ln}$ along $\mathbf{Q}$, thus the component of displacement normal to the diffracting planes. If $(u_{Qln} - u_{Ql'n'})$ is small and has equal probability of being positive or negative, or if it has a Gaussian distribution (making the following an exact expression),

$$\left\langle e^{iQ(u_{Qln}-u_{Ql'n'})} \right\rangle = e^{-\frac{1}{2}Q^2\langle(u_{Qln}-u_{Ql'n'})^2\rangle}\,. \tag{2.16}$$

In the case of helium, the displacements are not small, so the distribution needs to be Gaussian in order to use this expression. Using inelastic neutron scattering at high momentum transfers, the momentum distribution, $n(\mathbf{p})$, has been measured and found to be Gaussian even at low densities, within small experimental uncertainties [2].

If the displacements deviate from a Gaussian distribution, the simplification is more complex, being

$$\begin{aligned} \langle e^{iQ(u_{Qln}-u_{Ql'n'})}\rangle &= \exp\left(-\frac{1}{2}Q^2\langle(u_{Qln}-u_{Ql'n'})^2\rangle\right)\times \\ &\quad \exp\left(\frac{1}{24}Q^4\Big[\langle(u_{Qln}-u_{Ql'n'})^4\rangle - 3\langle(u_{Qln}-u_{Ql'n'})^2\rangle^2\Big]\right)\times O(Q^6)\,. \end{aligned} \tag{2.17}$$

Analysis of X-ray intensity data can reveal an estimation of an anharmonic effect through the non-Gaussian terms.

If the exponent in Eq. (2.16) is expanded and a Gaussian displacement is assumed,

$$\langle e^{iQ(u_{Qln}-u_{Ql'n'})}\rangle = e^{-\frac{1}{2}Q^2\langle {u_{Qln}}^2\rangle}e^{-\frac{1}{2}Q^2\langle {u_{Ql'n'}}^2\rangle}e^{Q^2\langle u_{Qln}u_{Ql'n'}\rangle}. \tag{2.18}$$

The abbreviation

$$M_{ln} \equiv \frac{1}{2}Q^2\langle {u_{Qln}}^2\rangle \tag{2.19}$$

is used along with

$$e^{Q^2\langle u_{Qln}u_{Ql'n'}\rangle} = 1 + \left(e^{Q^2\langle u_{Qln}u_{Ql'n'}\rangle} - 1\right) \tag{2.20}$$

in Eq. (2.15), resulting in

$$\begin{aligned} I(\mathbf{Q}) &= I_e\,P(Q)\sum_{l,n}\sum_{l',n'} f_n(Q)\,e^{-M_{ln}}\,f^*_{n'}(Q)\,e^{-M_{l'n'}}\,e^{i\mathbf{Q}\cdot(\mathbf{R}_{ln}-\mathbf{R}_{l'n'})} + \\ &\quad I_e\,P(Q)\sum_{l,n}\sum_{l',n'} f_n(Q)\,e^{-M_{ln}}\,f^*_{n'}(Q)\,e^{-M_{l'n'}}\,e^{i\mathbf{Q}\cdot(\mathbf{R}_{ln}-\mathbf{R}_{l'n'})}\left(e^{Q^2\langle u_{Qln}u_{Ql'n'}\rangle} - 1\right). \end{aligned} \tag{2.21}$$

Considering the second term, $\langle u_{Qln}u_{Ql'n'}\rangle$ approaches zero the further apart the atomic sites $\mathbf{R}_{ln}$ and $\mathbf{R}_{l'n'}$ are from each other; consequently, this term results in scattering that does not form sharp peaks, since the large $|\mathbf{R}_{ln}-\mathbf{R}_{l'n'}|$ values are what create the sharpness of peaks. This second term represents a diffuse contribution, called temperature diffuse scattering; this is actually

a misnomer in the case of low temperature helium crystals, since most of the motion is due to the zero-point energy of the crystal, not the phonons.

The first term is the same as Eq. (2.7), giving sharp peaks as before, but reduced by factors $e^{-M_{ln}} e^{-M_{l'n'}}$, both of which make up the Debye-Waller factor. It can again be represented by

$$I(\mathbf{Q}, M) = I_e \, P(Q) \, F_T(\mathbf{Q}, M)^2 \, B(\mathbf{Q}) \tag{2.22}$$

with the structure factor now including the Debye-Waller factor:

$$\begin{aligned} F_T(\mathbf{Q}, M) &= \sum_n f_n(Q) \, e^{-M_n} e^{i\mathbf{Q}\cdot\mathbf{r}_n} \\ &= \text{(at Bragg reflections)} \sum_n f_n(Q) \, e^{-M_n} e^{2\pi i(hx_n + ky_n + \ell z_n)} \, . \end{aligned} \tag{2.23}$$

When the crystal is composed of only one type of atom, all the M_n are the same, the expression for the structure factor can be simplified to $F_T(\mathbf{Q}, M)^2 = e^{-2M} F(\mathbf{Q})^2$, where $F(\mathbf{Q})$ is the structure factor for the static case. Changing M back to its definition, this first order intensity can be represented by

$$I(\mathbf{Q}, M) = I_e \, P(Q) \, F(\mathbf{Q})^2 \, e^{-2M} \, B(\mathbf{Q}) = I_e \, P(Q) \, F(\mathbf{Q})^2 \, e^{-Q^2 \langle {u_Q}^2 \rangle} \, B(\mathbf{Q}) \tag{2.24}$$

Just as before, $\langle {u_Q}^2 \rangle$ refers to the atomic motion that is perpendicular to the reflecting plane specified by $\mathbf{Q}$.

2.1.5 Integrated Intensity

When the intensity of a peak is desired, it is normally the integrated intensity that is measured, not the maximum intensity value of the peak.

In practice, the measurement of the maximum intensity value of a peak is difficult, since only photons reflecting at the exact Bragg angle would then be measured. This implies that the detector has an infinitely small solid angle, which would not work since there would be no counts, and the crystal is at the exact Bragg angle, which is impossible to attain. If the solid angle is increased to increase the count rate, photons corresponding to slightly off of the peak's maximum are then also measured, compromising the measurement. If the Bragg angle of the crystal is even slightly off,

the maximum value of the peak decreases. Both of these problems disappear when the intensity of the entire peak is integrated.

Even if one could measure the maximum value, there would be problems if the crystal was slightly mosaic. With the sub-crystals only slightly misaligned, there are multiple peaks in the θ rotation of the crystal. It would be impossible to pick a true maximum value, and with integrated intensity measurements, this is not a problem.

An integrated intensity scan over a peak is done by centering the peak into the detector. Slits in front of the detector are opened wide, allowing the detector to catch all the scattered intensity. The crystal is then rotated in the θ direction until the peak is gone. Then the crystal is rotated through the entire peak, while recording the detector measurements. The integration occurs simultaneously due to the detector, where the entire peak is measured at any given time, and the rotation, where the crystal is rotated through the Bragg angle. This assumes no background, no incoming flux variations, and no detector count rate corrections.

When the resulting scan is integrated, the intensity proportionality that is found is

$$I_{\text{int}} \propto I_0 \, L(Q) \, F(\mathbf{Q})^2 \, e^{-Q^2 \langle {u_Q}^2 \rangle} \,, \tag{2.25}$$

where

$$L(Q) = \frac{P(Q)}{\sin(2\theta)} \,. \tag{2.26}$$

The factor $L(Q)$ is the Lorentz polarization factor, which absorbs the polarization factor $P(Q)$.

2.1.6 Further Effects

For single perfect crystal X-ray diffraction, there are two additional effects that are normally taken into account, absorption and extinction. They are not taken into account for helium crystals of the size used in this thesis.

Absorption is the attenuation of the X-ray beam by the crystal itself. For helium crystals with the molar volumes seen in this thesis, the distance in the crystal for the intensity to be attenuated by half is around 10 cm (see Appendix A); the diameter of the crystal is less than one mm. Because of this, absorption can be neglected.

Extinction is another effect that sometimes needs to be taken into account. It is additional

interference effects caused by the multiple scattering of reflections within a crystal, and requires thick, perfect crystals. The main observable effect is a flattening of Bragg peaks. The flattening effect is not seen in the peaks, which is understandable since the helium crystals were not thick (when considering the very small scattering cross-section of helium) or perfect crystals; Polaroids of Bragg spots revealed multiple crystals. Because of this, extinction effects are neglected.

2.2 Analysis of the Debye-Waller Factor

In order to represent the measured mean square deviation as an equivalent Debye temperature, Θ_M, a more detailed analysis of the lattice dynamics is needed [3, 4].

2.2.1 Formulation of Debye-Waller Factor

As shown before, the equation

$$\mathbf{r}(t) = \mathbf{R} + \mathbf{u}(t) \tag{2.27}$$

shows how to represent the instantaneous position of a nucleus, $\mathbf{r}$, with a reciprocal lattice point, $\mathbf{R}$, and a time dependent deviation, $\mathbf{u}$. Again, assuming a harmonic model, phonons will be present in the crystal. However, $\mathbf{u}$ for one nucleus can be represented as a superposition of all the phonon modes present in the crystal, such as by

$$\mathbf{u}(t) = \sum_{g,j} a_{gj} \hat{\mathbf{e}}_{gj} \cos(\omega_{gj} t - \mathbf{g} \cdot \mathbf{R} - \delta_{gj}) \tag{2.28}$$

where $\mathbf{g}$ is a phonon wave vector with vibration directions $\hat{\mathbf{e}}_j$, a is the amplitude of the wave, ω is the phonon angular frequency, t is time, δ is an arbitrary phase factor, and the summation is over all phonon wave vectors g and vibration directions j. Using Eq. 2.28, the Debye-Waller factor, $2M$, can be shown to be

$$2M = Q^2 \langle {u_Q}^2 \rangle = \frac{1}{2} \sum_{g,j} (\mathbf{Q} \cdot \hat{\mathbf{e}}_{gj})^2 \langle {a_{gj}}^2 \rangle \,. \tag{2.29}$$

The next step is to express the mean square amplitude of a wave in terms of its thermal energy.

The kinetic energy of the crystal is

$$E_{\text{kinetic}} = \frac{1}{2}\sum_{n,l} m\,\dot{u}_{nl}^2 \tag{2.30}$$

where

$$\dot{u}_n = -\sum_{g,j} a_{gj}\omega_{gj}\sin(\omega_{gj}t - \mathbf{g}\cdot\mathbf{R} - \delta_{gj})\,. \tag{2.31}$$

From these equations, the mean kinetic energy is given by

$$\langle E_{\text{kinetic}}\rangle = \frac{1}{2}Nm\,\langle\dot{u}^2\rangle = \frac{1}{4}Nm\sum_{g,j}\langle {a_{gj}}^2\rangle {\omega_{gj}}^2\,. \tag{2.32}$$

The mean total energy is twice the mean kinetic energy, and $\langle\varepsilon_{gj}\rangle$ is the average energy of mode gj, giving

$$\langle E_{\text{total}}\rangle = \frac{1}{2}Nm\sum_{g,j}{\omega_{gj}}^2\langle {a_{gj}}^2\rangle = \sum_{g,j}\langle\varepsilon_{gj}\rangle\,, \tag{2.33}$$

giving

$$\langle\varepsilon_{gj}\rangle = \frac{1}{2}Nm{\omega_{gj}}^2\langle {a_{gj}}^2\rangle\,. \tag{2.34}$$

The energy of a phonon mode is

$$\varepsilon_{gj} = \hbar\omega_{gj}(n+1/2)\,, \tag{2.35}$$

where n is the number of phonons in a given mode; since only the average energy is needed, the number of phonons can be represented by the Bose-Einstein distribution, resulting in

$$\langle\varepsilon_{gj}\rangle = \hbar\omega_{gj}\left[\langle n(\omega_{gj},T)\rangle + \frac{1}{2}\right] = \hbar\omega_{gj}\left[\frac{1}{\exp(\hbar\omega_{gj}/k_{\text{B}}T)-1} + \frac{1}{2}\right]\,. \tag{2.36}$$

Putting all of this together gives the general form of the Debye-Waller factor for the harmonic model,

$$\begin{aligned} 2M &= \frac{1}{2}\sum_{g,j}(\mathbf{Q}\cdot\hat{\mathbf{e}}_{gj})^2\langle {a_{gj}}^2\rangle = \sum_{g,j}(\mathbf{Q}\cdot\hat{\mathbf{e}}_{gj})^2\frac{\langle\varepsilon_{gj}\rangle}{Nm{\omega_{gj}}^2} \\ &= \frac{\hbar}{Nm}\sum_{g,j}\frac{(\mathbf{Q}\cdot\hat{\mathbf{e}}_{gj})^2}{\omega_{gj}}\left[\frac{1}{\exp(\hbar\omega_{gj}/k_{\text{B}}T)-1} + \frac{1}{2}\right]\,. \end{aligned} \tag{2.37}$$

2.2.2 Debye Approximation

In order to represent the Debye-Waller factor (Eq. 2.37) by a single parameter, simplifications need to be made. One set of simplifications was introduced by Debye.

The atomic displacement is assumed to be isotropic (the magnitude of the displacement is the same regardless of direction), which is normally the case for a structure with a cubic symmetry. All phonon modes are assumed to be acoustic, with optic modes being accomodated by expanding the volume of the Brillouin zone. All wave oscillation directions are assumed to be either purely longitudinal or purely transverse. The phonon dispersion relation for each of the three oscillation directions is assumed to be linear in nature, such as

$$\omega_j = c_j k \,, \tag{2.38}$$

which implies a velocity that is independent of the wavelength of the phonon.

The Brillouin zone is replaced by a sphere of radius k_{D}, which has a volume equal to that of the Brillouin zone:

$$V_{\mathrm{BZ}} = \frac{4}{3}\,\pi\,{k_{\mathrm{D}}}^3 \,. \tag{2.39}$$

The density of phonon points is N/V_{BZ}, and the summation over k can be replaced by an integral over the sphere. Since the values of ω_j are independent of angle, the element of volume is a spherical shell of thickness $4\pi k^2\,dk$. For each oscillation direction, the direction $\hat{\mathbf{e}}_{kj}$ takes an equal probability over the entire shell; integrating this angularly over the shell and dividing by the area gives an average value of

$$\left\langle (\mathbf{Q}\cdot\hat{\mathbf{e}}_{kj})^2 \right\rangle = Q^2/3 \,. \tag{2.40}$$

Equation 2.37 becomes

$$2M = \frac{\hbar Q^2}{3Nm} \sum_j \int_0^{k_{\mathrm{D}}} \frac{1}{\omega_{kj}} \left[\frac{1}{\exp(\hbar\omega_{kj}/k_{\mathrm{B}}T) - 1} + \frac{1}{2} \right] \frac{N}{V_{\mathrm{BZ}}} 4\pi k^2\,dk \,. \tag{2.41}$$

There has to be a change of variable from k to ω_j in the integral before it can be solved; using Eq. 2.38,

$$k^2\,dk = \frac{{\omega_j}^2}{{c_j}^3}\,d\omega_j \,. \tag{2.42}$$

The V_{BZ} also needs to be changed, resulting in

$$V_{\mathrm{BZ}} = \frac{4}{3}\pi \left(\frac{\omega_{\mathrm{D}j}}{c_j} \right)^3 , \tag{2.43}$$

where $\omega_{\mathrm{D}j}$ is the Debye frequency, the maximum frequency for a given oscillation direction j. Putting these equations into Eq. 2.41 gives

$$2M = \frac{\hbar Q^2}{m} \sum_j \frac{1}{{\omega_{\mathrm{D}j}}^3} \int_0^{\omega_{\mathrm{D}j}} \left[\frac{1}{\exp(\hbar\omega/k_{\mathrm{B}}T) - 1} + \frac{1}{2} \right] \omega \, d\omega \, . \tag{2.44}$$

Let

$$\epsilon \equiv \frac{\hbar\omega}{k_{\mathrm{B}}T} \qquad \text{and} \qquad x_j \equiv \frac{\hbar\omega_{\mathrm{D}j}}{k_{\mathrm{B}}T} \, . \tag{2.45}$$

The Debye integral is introduced as

$$\Phi(x) \equiv \frac{1}{x} \int_0^x \frac{\epsilon \, d\epsilon}{e^{\epsilon} - 1} \, . \tag{2.46}$$

The use of these definitions, and a partial integration, results in

$$2M = \frac{\hbar^2 Q^2}{m k_{\mathrm{B}} T} \sum_j \frac{1}{{x_j}^2} \left[\Phi(x_j) + \frac{x_j}{4} \right] . \tag{2.47}$$

The Debye temperature is defined as

$$\Theta_{\mathrm{D}} \equiv \frac{\hbar\omega_{\mathrm{D}}}{k_{\mathrm{B}}} \, , \tag{2.48}$$

and in this thesis, Θ_{D} is a general Debye temperature, while Θ_x is a Debye temperature of type x (with the D subscript implicit). In order to see how Eq. 2.47 depends on Θ_j, x_j needs to be redefined as

$$x_j \equiv \frac{\Theta_j}{T} \, ; \tag{2.49}$$

for each type of oscillation direction, longitudinal or transverse, there is a characteristic Debye temperature. Expanding the series in Eq. 2.47 gives

$$2M = \frac{\hbar^2 Q^2}{m k_{\mathrm{B}} T} \left\{ \frac{1}{{x_l}^2} \left[\Phi(x_l) + \frac{x_l}{4} \right] + \frac{2}{{x_t}^2} \left[\Phi(x_t) + \frac{x_t}{4} \right] \right\} . \tag{2.50}$$

In order to combine the terms in brackets, some approximations need to be made. Expanding the exponential in Eq. 2.46 gives

$$\left[\Phi(x) + \frac{x}{4}\right] = 1 + \frac{x^2}{36} - \frac{x^4}{3600} + \cdots . \tag{2.51}$$

If $x < 2$, meaning $T > \Theta_{\mathrm{D}}$, $[\Phi(x) + x/4]$ is very similar for both transverse and longitudinal waves. An average Θ_M is introduced according to

$$\frac{3}{{\Theta_M}^2} \equiv \frac{1}{{\Theta_l}^2} + \frac{2}{{\Theta_t}^2} . \tag{2.52}$$

With the average temperature Θ_M and the expansion, the Debye-Waller factor becomes

$$2M = \frac{3\hbar^2 Q^2}{m k_{\mathrm{B}} T x^2}\left[\Phi(x) + \frac{x}{4}\right] = \frac{3\hbar^2 Q^2}{m k_{\mathrm{B}}}\left(\frac{T}{{\Theta_M}^2}\right)\left[\Phi(x) + \frac{x}{4}\right] . \tag{2.53}$$

2.2.3 Structure Considerations

The Debye-Waller factor in its general form,

$$2M = Q^2 \langle {u_Q}^2 \rangle , \tag{2.54}$$

has a directional dependence which comes from the fact that $\langle {u_Q}^2 \rangle$ is the mean squared atomic displacement in the $\mathbf{Q}$ direction. The form of this dependence for fcc and hcp needs to be discussed.

The equation for the oscillation can be broken into

$$u_Q = u_x \cos(\mathbf{Q}, \mathbf{x}) + u_y \cos(\mathbf{Q}, \mathbf{y}) + u_z \cos(\mathbf{Q}, \mathbf{z}) , \tag{2.55}$$

where $\cos(\mathbf{Q}, \mathbf{i})$ is cosine of the angle between $\mathbf{Q}$ and the i-axis. If the approximation that $\langle {u_x}^2 \rangle$, $\langle {u_y}^2 \rangle$, and $\langle {u_z}^2 \rangle$ are independent is used when forming the square and taking the average, the result is

$$\langle {u_Q}^2 \rangle = \langle {u_x}^2 \rangle \cos^2(\mathbf{Q}, \mathbf{x}) + \langle {u_y}^2 \rangle \cos^2(\mathbf{Q}, \mathbf{y}) + \langle {u_z}^2 \rangle \cos^2(\mathbf{Q}, \mathbf{z}) . \tag{2.56}$$

The fcc structure can be based on the cubic basis. For cubic crystals, all three directions are equal since there is no differentiation between the a, b, and c axes, expressed by $\langle {u_x}^2 \rangle = \langle {u_y}^2 \rangle =$

$\langle {u_z}^2 \rangle$. Since $\cos^2(\mathbf{Q},\mathbf{x}) + \cos^2(\mathbf{Q},\mathbf{y}) + \cos^2(\mathbf{Q},\mathbf{z}) = 1$, it follows that $\langle {u_Q}^2 \rangle$ is independent of the direction of u_Q. So, for the cubic case, $\langle {u_Q}^2 \rangle$ is isotropic, which was one of the conditions for the Debye approximation. For the cubic case, because of this isotropy, $\langle {u_Q}^2 \rangle$ is normally referred to as just $\langle u^2 \rangle$.

The hcp structure is based on the hexagonal basis. Let the projection of $\mathbf{Q}$ on the x-y plane have the direction $\mathbf{r}$. Equation 2.56 then becomes

$$\langle {u_Q}^2 \rangle = \Big(\langle {u_x}^2 \rangle \cos^2(\mathbf{r},\mathbf{x}) + \langle {u_y}^2 \rangle \cos^2(\mathbf{r},\mathbf{y}) \Big) \cos^2(\mathbf{Q},\mathbf{r}) + \langle {u_z}^2 \rangle \cos^2(\mathbf{Q},\mathbf{z}) \,. \tag{2.57}$$

For hexagonal crystals, the $\mathbf{x}$ and $\mathbf{y}$ directions are equal since there is no differentiation between the a and b axes, and this is expressed by $\langle {u_r}^2 \rangle = \langle {u_x}^2 \rangle \cos^2(\mathbf{r},\mathbf{x}) + \langle {u_y}^2 \rangle \cos^2(\mathbf{r},\mathbf{y})$. Using this relation results in

$$\langle {u_Q}^2 \rangle = \langle {u_r}^2 \rangle \sin^2(\mathbf{Q},\mathbf{z}) + \langle {u_z}^2 \rangle \cos^2(\mathbf{Q},\mathbf{z}) \,, \tag{2.58}$$

where $\langle {u_z}^2 \rangle$ and $\langle {u_r}^2 \rangle$ are the components parallel and perpendicular to the z-axis. In general, for an hcp crystal, $\langle {u_z}^2 \rangle$ and $\langle {u_r}^2 \rangle$ are different (see Appendix E).

2.3 Thermodynamic Properties

Several measurable properties of crystals, such as M, M', and C_V, can be expressed using a density of states, $g(\omega)$. The density of states replaces a summation over all phonon modes. Using these expressions, it is possible to relate these different types of measurements.

The relations given are for the Debye-Waller factor [5],

$$M = \frac{Q^2}{6Nm} \int_0^{\omega_{\max}} \frac{\langle \varepsilon \rangle \, g(\omega)}{\omega^2} \, d\omega \,, \tag{2.59}$$

the temperature derivative of the Debye-Waller factor [6],

$$M' = \frac{dM}{dT} = \frac{Q^2}{6Nm} \int_0^{\omega_{\max}} \frac{d}{dT} \left(\frac{\langle \varepsilon \rangle \, g(\omega)}{\omega^2} \right) d\omega \,, \tag{2.60}$$

and the heat capacity [7],

$$C_V = \int_0^{\omega_{\max}} \left(\frac{\partial \langle \varepsilon \rangle}{\partial T} \right)_V g(\omega) d\omega \,. \tag{2.61}$$

The density of states used is normalized to the total number of phonon modes in the crystal,

$$\int_0^{\omega_{\max}} g(\omega) d\omega = 3N \,, \tag{2.62}$$

where $\omega_{\max}$ is the maximum frequency of the density of states. The average energy of each phonon mode is given by

$$\langle \varepsilon(\omega, T) \rangle = \hbar\omega \left[\frac{1}{\exp(\hbar\omega / k_{\mathrm{B}} T) - 1} + \frac{1}{2} \right] = \frac{\hbar\omega}{2} \coth\left(\frac{\hbar\omega}{2 k_{\mathrm{B}} T} \right) . \tag{2.63}$$

Measurements of these three types can be expressed in terms of a temperature dependent Debye temperature. This is accomplished by using the Debye model as described in Section 2.2.2. In this model, the density of states is

$$g(\omega) = \left(\frac{9N}{{\omega_{\mathrm{D}}}^3} \right) \omega^2 \tag{2.64}$$

and $\omega_{\mathrm{D}} = \omega_{\max}$. In order to get the Debye temperature, the measured value is set equal to the Debye model relation. Then the relation is solved for ω_{D}, with the Debye temperature being

$$\Theta_{\mathrm{D}}(T) = \frac{\hbar \omega_{\mathrm{D}}(T)}{k_{\mathrm{B}}} \,. \tag{2.65}$$

The temperature dependence comes from the fact that the Debye temperature assumes an unrealistic Debye model and the anharmonic effects of a physical crystal are also unaccounted for. There are three Debye temperatures corresponding to the three relations, Θ_M, $\Theta_{M'}$, and Θ_{C_V}; they will not have the same values in general for each temperature, since these relations weight different regions of the density of states.

A similar type of quantity to the thermodynamic relations are the moments of the frequency distribution [8],

$$\mu(n) = \frac{1}{3N} \int_0^{\infty} \omega^n g(\omega) \, d\omega \,, \tag{2.66}$$

where there is a weighting of ω to the order n. In this form they are unwieldy, since they can vary over several orders of magnitude, so what is generally done is equate the right side of Eq. 2.66 where $g(\omega)$ is the (unknown) density of states of the material to a copy where $g(\omega)$ is that of the Debye

model (Eq. 2.64). This equation is solved for the nth-order Debye frequency, $\omega_{\mathrm{D}}(n)$, resulting in

$$\omega_{\mathrm{D}}(n) = \left[\left(\frac{n+3}{3}\right)\mu(n)\right]^{\frac{1}{n}} \qquad (n > -3, n \neq 0)\,. \tag{2.67}$$

The $n = -3$ and $n = 0$ cases can be found in an asymptotic limit to each, and normally the maximum n considered is $n = 6$.

The Equations 2.59 to 2.61 can be expanded in terms of the Debye moments of the distribution for both the high temperature and low temperature limits. From this, a limiting value of the Debye Temperature can be found as a Debye moment. This has been done for Θ_M [5], $\Theta_{M'}$ [9], and Θ_{C_V} [10], with the results being

$$\Theta_M(T \to 0) = (\hbar/k_{\mathrm{B}})\,\omega_{\mathrm{D}}(-1) \qquad \Theta_M(T \to \infty) = (\hbar/k_{\mathrm{B}})\,\omega_{\mathrm{D}}(-2) \tag{2.68}$$

$$\Theta_{M'}(T \to 0) = (\hbar/k_{\mathrm{B}})\,\omega_{\mathrm{D}}(-3) \qquad \Theta_{M'}(T \to \infty) = (\hbar/k_{\mathrm{B}})\,\omega_{\mathrm{D}}(-2) \tag{2.69}$$

$$\Theta_{C_V}(T \to 0) = (\hbar/k_{\mathrm{B}})\,\omega_{\mathrm{D}}(-3) \qquad \Theta_{C_V}(T \to \infty) = (\hbar/k_{\mathrm{B}})\,\omega_{\mathrm{D}}(+2)\,. \tag{2.70}$$

No two Debye temperatures have agreeing values in both limits.

If data for one type of measurement over a broad range of temperature can be taken, the moments of the distribution can be extracted. This has been shown for the C_V case [10, 5], with moments from $n = -3$ to $n = 6$ being found, with the lower moments being more accurate than the higher. For the case of helium, it is not possible to collect enough M or M' data to calculate the moments due to how difficult the data is to take, leaving only the possibility of using C_V (which has been measured for helium quite well). The only caveat of this method of calculating the moments is that it assumes only one-phonon processes, which is not true for helium.

2.4 Anharmonicity

The harmonic approximation does not hold perfectly for any actual crystal. This is easily seen by considering a few of the expected properties of a purely harmonic crystal: no thermal expansion and infinite thermal conductivity [11]. In any real crystal, neither of these cases hold.

2.4.1 Thermal Expansion

Thermal expansion is caused by the fact that the interaction potential is asymmetric. As the temperature is changed, the energy and the range of motion of the nuclei increase. This increase in motion and the asymmetry causes a shift in the mean position of the nuclei relative to one another, resulting in thermal expansion. The anharmonicity behind thermal expansion can be included by the use of a dimensionless parameter, the Grüneisen parameter. With this tool, the anharmonicity can be represented as the replacement [12]

$$\omega^2 \quad \longrightarrow \quad {\omega_{\mathrm{Q}}}^2 \equiv \frac{\omega^2}{(1+2\,\gamma\,\kappa\,T)}\,, \tag{2.71}$$

where γ is the Grüneisen parameter and κ is the volume coefficient of expansion. This replacement is the basis of quasi-harmonic theory; this model assumes that the phonon frequencies depend on the volume, but a harmonic potential is still assumed.

The Grüneisen parameter, in its most general form, relates each phonon mode to the volume,

$$\gamma_{gj} = -\frac{\partial \ln \omega_{gj}}{\partial \ln V}\,. \tag{2.72}$$

There are other types of Grüneisen parameters. There is one corresponding to the moments of the distribution,

$$\gamma(n) = -\left(\frac{1}{n}\right)\frac{\partial \ln \mu(n)}{\partial \ln V} = -\frac{\partial \ln \omega_{\mathrm{D}}(n)}{\partial \ln V}\,. \tag{2.73}$$

The Grüneisen parameter corresponding to the Debye frequency is defined as

$$\gamma_D(T) = -\frac{\partial \ln \omega_{\mathrm{D}}(T)}{\partial \ln V} = -\frac{\partial \ln \Theta_{\mathrm{D}}(T)}{\partial \ln V}\,. \tag{2.74}$$

It is temperature dependent, and if the limiting cases of the Debye temperatures are considered, Eqs. 2.68 to 2.70, the Grüneisen parameters in the high and low limits become

$$\gamma_M(T\to 0) = \gamma(-1) \qquad \gamma_M(T\to \infty) = \gamma(-2) \tag{2.75}$$

$$\gamma_{M'}(T\to 0) = \gamma(-3) \qquad \gamma_{M'}(T\to \infty) = \gamma(-2) \tag{2.76}$$

$$\gamma_{C_V}(T\to 0) = \gamma(-3) \qquad \gamma_{C_V}(T\to \infty) = \gamma(+2)\,. \tag{2.77}$$

The Grüneisen parameter corresponding to the Debye frequency can be useful to relate Debye temperatures at different volumes [5] (assuming that the Grüneisen parameter is constant), using

$$\frac{\Theta_{\mathrm{D}}(V_0)}{\Theta_{\mathrm{D}}(V)} = \left(\frac{V}{V_0}\right)^{\gamma_D} . \tag{2.78}$$

2.4.2 Thermal Conductivity

Heat conduction is the process of transference of vibrational energy from one part of a material to another. In the case of harmonic crystals, this vibrational energy is transferred in the form of phonons. The discussion in this section assumes a pure crystal with no defects, and is infinitely big so that surface effects can be ignored.

Phonon states in harmonic solids are stationary states, so once a phonon distribution is created such that it carries a thermal current, it stays that way forever; the thermal conductivity is infinite. If anharmonic effects are taken into account, phonon modes interact with one another. This takes the form of phonons transferring between modes, where the total number of phonons is not conserved; this can be thought of as the creation and annihilation of phonons.

If the anharmonic effects are small, their effects may be understood in simple terms using perturbation theory. These effects are governed by conservation of both crystal momentum and energy (momentum conservation has a caveat, described later). The cubic effect involves the change of the phonon numbers of three different modes, for a net phonon gain of 1 or -1; one phonon splits into two new phonons or two phonons combine to form one phonon. The quartic effect involves the change of the phonon numbers of four different modes, for a net phonon gain of 2, 0, or -2; one phonon splits into three, two phonons change into two different phonons, or three phonons combine into one. The sizes of the cubic and quartic terms are similar, since the cubic term is a second order perturbation while the quartic term is a first order perturbation; this means that any attempt to allow for the cubic correction should also include the quartic term, especially since they are normally of opposite sign.

These anharmonic effects as discussed do not explain the finite nature of the thermal conductivity, since none of these phonon interactions change the total crystal momentum of the phonons in the crystal. The finite nature comes from umklapp processes, which are a special type of anharmonic process. Taking the cubic case as an example where two phonons merge into one, the

umklapp process would happen if the wave vector of the phonon sum would lie outside the first Brillouin zone of the crystal; in this case, a reciprocal lattice vector **K** would be subtracted from this sum such that the resultant phonon wave vector would lie inside the first Brillouin zone. A similar process is involved with the quartic cases. This subtraction of some value **K** obviously causes the total crystal momentum of the phonons involved in a umklapp process to not be conserved.

Anharmonic processes can be thought of as "collisions" between phonons (where the total number of phonons is not constant). A relaxation time τ can be used to describe the mean time between anharmonic processes, making the phonons act similar to a gas. When a temperature gradient is placed across the crystal, the more energetic phonons from the warmer side will move toward the colder side. As they do this, collisions will occur, and for each one that results in an umklapp process, the net phonon momentum towards the cold side diminishes, "impeding" the flow of heat. Thus, a crystal with anharmonic processes has a finite thermal conductivity.

References

[1] B. E. Warren, *X-ray Diffraction* (Dover, New York, 1990).

[2] R. C. Blasdell, D. M. Ceperley, and R. O. Simmons, Z. Naturforsch. **48a**, 433 (1993).

[3] B. E. Warren, in *X-ray Diffraction* (Dover, New York, 1990), Chap. 11.

[4] M. Blackman, Acta Crystallogr. **9**, 734 (1956).

[5] T. H. K. Barron, A. J. Leadbetter, J. A. Morrison, and L. S. Salter, Acta Crystallogr. **20**, 125 (1966).

[6] R. M. Nicklow and R. A. Young, Phys. Rev. **152**, 591 (1966).

[7] C. Kittel, in *Introduction to Solid State Physics* (Wiley, New York, 1986), Chap. 5.

[8] L. S. Salter, Adv. Phys. **14**, 1 (1965).

[9] R. C. Windecker, Ph.D. thesis, University of Illinois at Urbana-Champaign, 1970.

[10] T. H. K. Barron, W. T. Berg, and J. A. Morrison, Proc. R. Soc. London, Ser. A **242**, 478 (1957).

[11] N. W. Ashcroft and N. D. Mermin, in *Solid State Physics* (Harcourt Brace, New York, 1976), Chap. 25.

[12] W. F. Kuhs, Acta Crystallogr. Sect. A **48**, 80 (1992).

Chapter 3

Experimental Apparatus and Equipment

The experimental apparatus has several sections. One is the cryogenic system, consisting of the Displex head, compressor, and heaters. Another is the high pressure gas handling system, which consists of the helium supply bottle, the compressor, the valves, and all the connecting tubing. The sample cell is a very important part, being both part of the gas handling system and the cryogenic system. Also, there are electronics associated with the experiment. The last component is the X-ray source, which is in this case either the National Synchrotron Light Source at Brookhaven National Laboratory or the Advanced Photon Source at Argonne National Laboratory.

The setup of this experiment is very similar to the one used by C. T. Venkataraman in her thesis work [1]. Much of the equipment used is the same as she used [2]. The setup used by her (and subsequently the one I used) was influenced by the thesis work of A. T. Macrander [3].

3.1 Gas Handling System

The gas handling system is complex and composed of many pieces. Fig. 3.1 is a schematic of it.

Several concerns needed to be taken into consideration when the gas handling system was designed. The high 99.9999% purity of the sample gas needs to be maintained. There is also a desire to minimize the volume of the system that is not part of the sample cell. The stored energy of the system is proportional to the volume, so this is a safety concern. When using ^{3}He, the smaller volume minimizes the amount of this expensive gas that is needed. The maximum working pressure also has to be determined, so that the correct type of tubing and valves can be used.

In order to maintain the high purity of the sample gas, metal-to-metal seals are needed throughout the system, with the inside of the system being thoroughly clean. Metal-to-metal seals are also

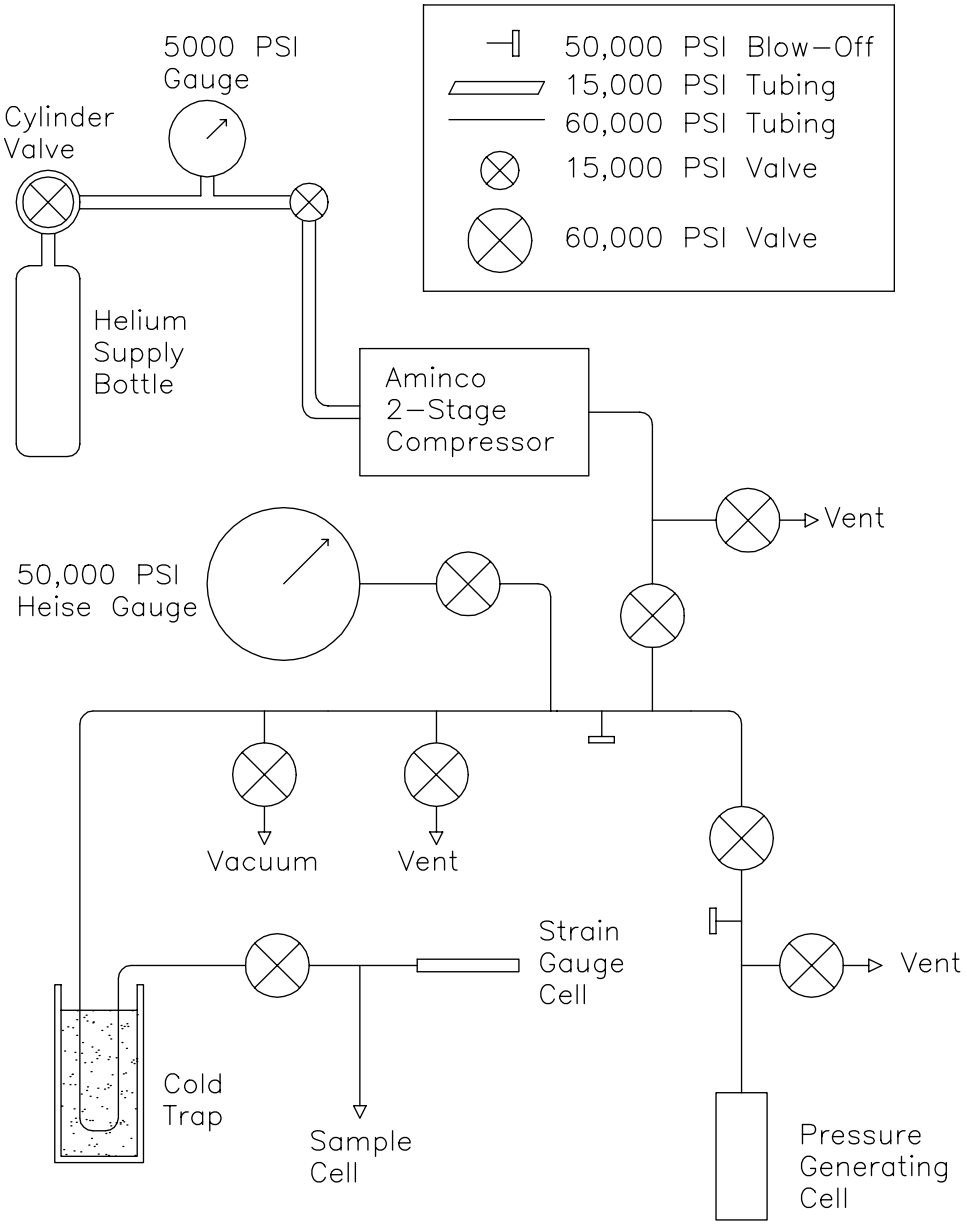

Figure 3.1: Schematic of the pressure system.

ideal for high pressure systems such as this.

To find out maximum working pressure, the needs of the desired research have to be addressed. The system needs to be able to go above the fcc-hcp-liquid triple point for helium, which is at 111.6 MPa for ^{4}He and 158 MPa for ^{3}He. Consequently, a good maximum working pressure is 300 MPa.

For this pressure, we used tubing, fittings, and valves rated up to 60,000 PSI (∼415 MPa) [4]. The standard tubing for this pressure has an outer diameter of 1/8" (3.175 mm) and an inner diameter of 0.020" (0.508 mm), and is drawn from 316 stainless steel. The valves are also made out of 316 stainless steel, and the stems are protected from leaking by Teflon. There are also two other smaller sizes of tubing in the system [5], and in order to use them, one has to vacuum braze them to a drilled plug.

To protect the system from going above the rated pressure for the system, there are two rupture disks attached at different points of the system. One is attached directly to the pressure generating cell (PGC), and the other is attached to the main line of the system.

In order for us to know what the pressure is in the system, there are two devices on the system. One is a large dial pressure gauge that is rated to 50,000 PSI (∼345 MPa) and is very precise with a resolution of 50 PSI [6]. This is a Bourdon tube style gauge, and has a smaller internal volume than similar gauges.

The other pressure device is the strain gauge cell (SGC). The SGC is a specially made part that is made of Vascomax 300 CVM maraging steel. It is cylindrical and is hollow. To minimize the volume of this device, an insert fills the hollow; however, it still allows the free movement of the outside walls. When it is under pressure, the circumference of the outer walls swells linearly with the pressure. On the outside of these outer walls are mounted two pair of strain gauges [7]. Each pair is made by the manufacturer to have the gauges perpendicular to each other. Each is mounted such that one gauge lies along the axis of the SGC, while the other lies along the circumference; this allows for compensation of temperature effects. The gauge that lies along the circumference measures the pressure effect and the temperature effect, while the axial gauge measures mostly the temperature effect. Each pair makes one half of a strain gauge bridge, and the two pairs are oriented antisymmetrically in the bridge. The voltage in the middle of the strain gauge bridge is measured by a high precision digital strain gauge meter. The measured voltage is calibrated with

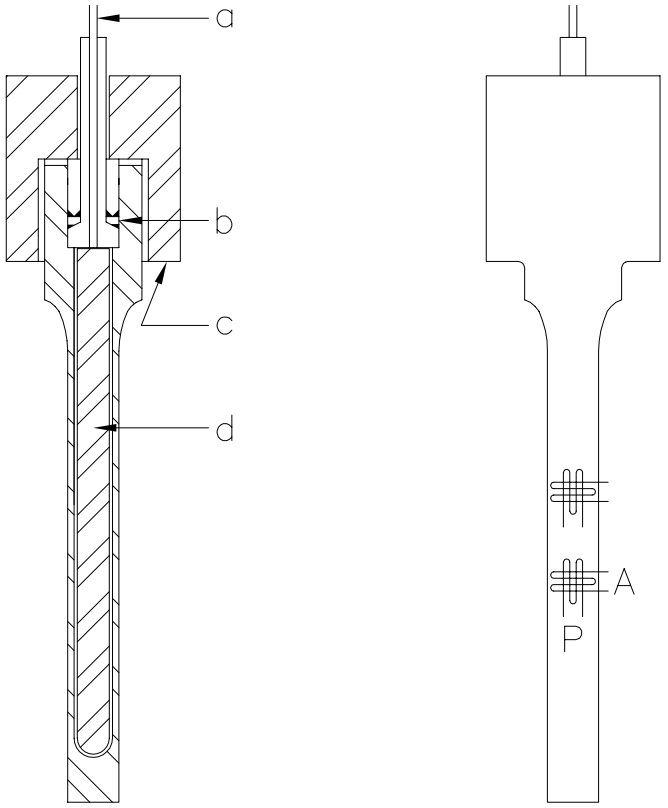

Figure 3.2: Diagram of the strain gauge cell. The right diagram shows the positions of the strain gauge pairs on the SGC. The strain gauge marked 'A' is the active one that measures both the expansion due to the gas pressure and the thermal expansion, while the strain gauge marked 'P' is the passive one that measures only the thermal expansion. The left diagram labels the metal components. a) Stainless steel fill line that leads to the pressure system. b) Sealing region. c) Maraging steel nut. d) Maraging steel insert that reduces the dead volume.

---

the Heise gauge at a wide range of pressures to get a linear slope and offset (see Appendix G.2.1. The strain gauges in practice do drift a bit, making the corresponding values not highly accurate, but their function is more for detecting small, rapid pressure changes. Figure 3.2 is a diagram of the SGC.

In order to get to the desired pressure, a compressor needs to be used. It has to be a special one that allows no foreign contamination (e.g. oil, air) to get into the gas it is pumping. The compressor used has two stages that are driven by compressed air [8]. The compression is accomplished by the action of the air upon a metal diaphragm, which in turn acts upon the helium. Each stage of the pump has an intake and outlet check valve to keep the gas from flowing backwards. This pump, however, can only pump a gas up to a maximum of 30,000 PSI ($\sim$205 Mpa). To go any

higher, another device has to be used, the PGC (described below). To protect the compressor (and system) from dirt in the helium bottle, there is a filter before the intake of the compressor. Tubing, fittings, and valves rated only to 15,000 PSI (∼103 MPa) [4] are used between the supply bottle(s) and the pump because of the lower pressure in that section.

To get to pressures above 30,000 PSI, the pressure generating cell (PGC) is used. This is a specially made part that is made of Vascomax 300 CVM maraging steel. It is cylindrical and has a large hollow volume inside of it. To use it, it is cooled down to liquid nitrogen temperatures, and then filled with helium at 30,000 PSI from the compressor. Once this is done, the compressor is valved off from the rest of the system, and is then warmed towards room temperature. This warming then raises the pressure. The PGC is also wrapped with a heater wire that can speed up the warming process if used, and can even cause the temperature go above room temperature in order to get more pressure. Once the desired pressure is attained, the PGC is valved off from the rest of the system, and is then vented. This can be done multiple times for diminishing returns.

Between the compressor and the sample cell is a cold trap, which gets filled with liquid nitrogen. The timing of the filling of the cold trap is important: it is done after the non-helium gases are pumped out and flushed, but before the system is pumped up to its final pressure, so as to capture any impurities that would otherwise go into the sample cell.

One critical piece of the gas handling system is not normally connected to the system, which is the leak detector [9]. It is crucial for finding the leaks that may occur in the system, and is extremely sensitive to such leaks. It is a small, self-contained unit, with roughing and turbo pumps built into it. If need be, it can be used as a turbo pump to pump out a section of line, but this is avoided.

The preparation of the gas handling system includes pumping out the system, purging the system with ^{4}He, checking for leaks, and finally pumping up the system with the desired sample gas. This is all described in detail in Appendix G.2.2.

3.2 Sample Cell

The sample cell has to be able to make it to the desired pressure of 300 MPa without bursting. It needs to be made of a low Z material so that it will absorb as little of the X-rays as possible. It would also be beneficial if the material was in a highly multicrystalline form, so as to create

smooth and uniform Debye-Scherrer rings. This removes the problem of having to worry about the orientation of the crystals in the cell, vastly simplifying the considerations of the background from the cell.

A good material to use is beryllium. It has a Z number of 4, and can be powdered and hot-press sintered into a strong solid. There is a grade of material of this type, I-250 [10], which is composed of 97% Be and 2.5% BeO, and has an ultimate tensile strength (σ_u) of 517 MPa and a yield strength (σ_y) of 448 MPa. This material also has grain sizes of less than 15 μm, which gives the Debye-Scherrer rings a uniform appearance.

The cell is cylindrical in shape because of the need for strength in the cell's walls. This also allows the high degree of symmetry for the crystal. This symmetry helps in the growing of a single crystal, since the cooling of the helium is uniform. This also helps keep the exposure of X-rays even over the crystal as it is rotated about the axis. This is important since there is almost no control in the orientation of a crystal as it grows.

When designing the cell, the desired bursting pressure (P_B) relates to the cell wall diameters via the following formulae [11]:

$$P_B = \sigma_u \left(1 + \frac{\sigma_y}{\sigma_u}\right)\left(\frac{K-1}{K+1}\right), \qquad K \equiv \left(\frac{\text{outer diameter}}{\text{inner diameter}}\right). \tag{3.1}$$

The cell design used is from a previous experiment and was designed by R. K. Crawford. The cell design has an inside diameter of 0.032" (0.813 mm) and an outside diameter of 0.082" (2.08 mm), which results in a bursting pressure of 423 MPa. Since the working maximum pressure is 300 MPa, this is 71% of the bursting pressure, leaving a comfortable safety margin.

When machined [12], the cell's outer diameter was kept within a narrow margin of error, so as to not stress any part of the wall more than any other, when under pressure. Similarly, when the central hole was drilled and reamed, this interior wall was given a lapped finish, since any scratch could cause the cell to fracture. The bottom of the hole was also made to be smoothly rounded.

The cell is mounted in an assembly, which is shown in Fig. 3.3. To seal the pressure cell, there are metal-to-metal seals connecting the beryllium cell to the pressure system. The cell slides through a casing made of maraging steel, with the cell's head resting at the bottom. On top of this, a stainless steel insert is placed. After this comes a mushroom fitting that is made of maraging steel that is vacuum brazed to the end of a fill line. Lastly, a threaded maraging steel nut that the

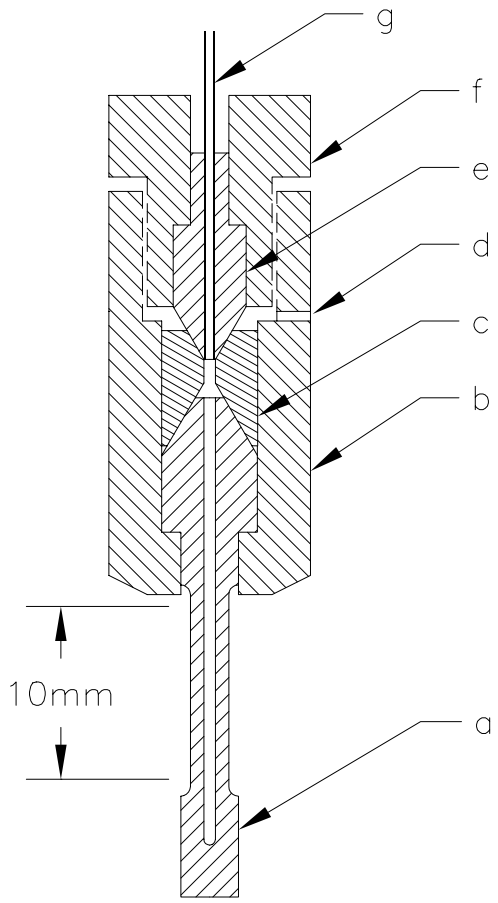

Figure 3.3: Diagram of the sample cell assembly. a) Polycrystalline beryllium sample cell (ID 0.8 mm, OD 2 mm) with a 10 mm region that is accessible to the incident beam. b) Maraging steel casing. c) Stainless steel sealing insert. d) Safety vent. e) Maraging steel mushroom fitting, which is vacuum brazed to the fill line. f) Maraging steel nut. g) Stainless steel fill line that leads to the pressure system.

---

fill line goes through is screwed into the threads inside of the casing; the turning of this applies the pressure for the seals at the stainless steel insert. In this assembly, all the pieces made out of the maraging steel were heat treated after machining to strengthen them.

3.3 Cryogenic System

The refrigerator for the experiment had to be chosen, conforming to the needs of the desired samples. In order to have access to the hcp phase with no intermediate fcc phase during the growth process, the cell has to get to a temperature lower than the fcc-hcp-liquid triple point, which is at

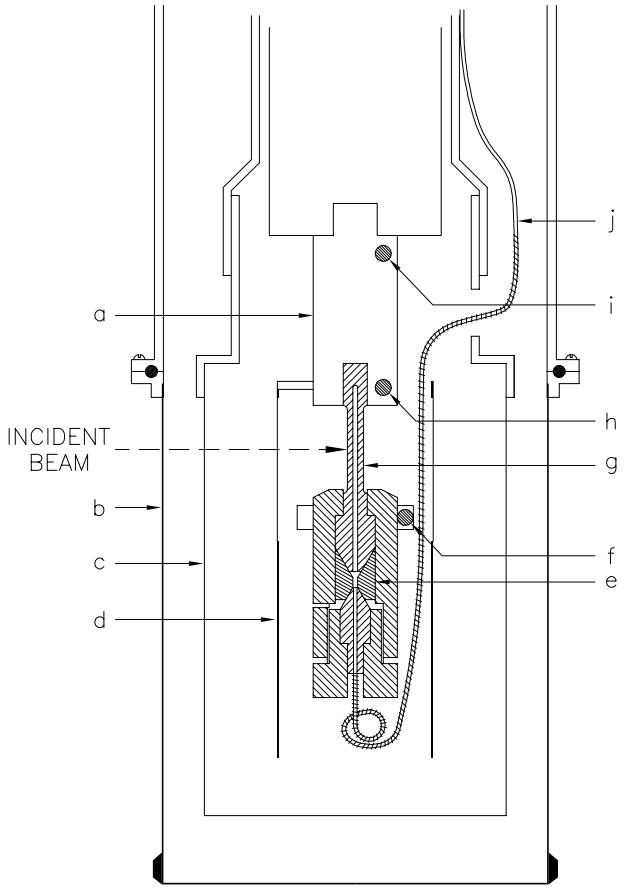

Figure 3.4: Diagram of the Displex head, with the sample cell mounted. a) Copper cold finger extension. b) Lexan vacuum shield. c) Beryllium intermediate temperature radiation shield. d) Low temperature radiation shield (Copper frame with aluminized Mylar windows). e) Sealing region of the sample cell assembly. f) Silicon diode sensor B. g) Beryllium sample cell. h) Silicon diode sensor A. i) Control silicon diode sensor. j) Fill line with heater wire.

14.9 K for ^{4}He and 17.8 K for ^{3}He.

This experiment uses a closed-cycle refrigerator that is specially adapted to fit in a Huber goniometer [13], and has Displex as its brand name. The Displex model used has the ability to reach around 10 K, which made it a reasonably good choice for this experiment. More recent Displex models can go as low as 6.5 K. Figure 3.4 is a diagram of the Displex head with the sample cell mounted.

In practice, the actual Displex used in this experiment performed quite well at reaching 10 K and staying there, assuming that there was a good vacuum inside the Displex head and also that the helium in the closed cycle of the refrigerator had no contaminants. If the vacuum is bad, such

as from a small leak, air will freeze onto the cold finger, sample cell, etc., creating a larger load that the Displex must cool. If the helium inside the refrigerator has contaminants, they will freeze inside the Displex at the piston mechanism, which causes the Displex to make an audible noise as the piston strikes the ice, and the minimum achievable temperature rises with time.

Inside the Displex head, there is a cold finger that extends towards the center of rotation of the goniometer. The cold finger ends with a screw thread, allowing the mounting of a sample. Around the circumference of the cold finger is a heater wire wrapped many times. Also, there is a silicon diode thermometer mounted at the end of the cold finger, which is the control thermometer. During normal operation, the heater and thermometer work together with a temperature controller to maintain the desired temperature.

Onto the cold finger is screwed a mounting piece of cylindrical OFHC (oxygen free, high conductivity) copper that has a C-shaped clamp at the other end, which accepts the sample cell. Mounted on this piece is a silicon diode thermometer, sensor A [14]. This thermometer measures the clamp's temperature as it touches the end of the cell.

In order to shield the sample cell from the infrared heat radiation from the outside, there are two intermediate heat shields. The innermost one is composed of copper with an aluminized Mylar window that extends for about 320 degrees around the cell. The 40 degree strut is needed for support of the end of the window mount, and is positioned so that the fill line runs along this strut, minimizing obstruction of the X-ray beam. The outer shield is a solid piece of beryllium that is machined into the shape of a hollow can that screws into the threads on the Displex, which were designed for this purpose.

To hold the vacuum required in the Displex, and also allow the passage of X-rays into the cell, there is a outermost can made of Lexan [15]. This encloses the radiation shields and the sample cell. The choice of Lexan for the material is important. The sample cell is made of beryllium, the dust of which is poisonous. The possibility of the cell shattering and creating dust causes a safety concern. Therefore, a strong enclosure is needed; making this enclosure from Lexan makes sense since it is the material bullet-proof glass is made out of. In order to reduce absorption of X-rays, the thickness of the can needs to be minimized since Lexan is a polycarbonate and will absorb X-rays more strongly than beryllium. The walls of the can were machined quite thin and still held a great deal of strength. A cell did explode during research by C. T. Venkatarman, and the Lexan

can did a good job of containing everything. The Lexan does yellow upon prolonged exposure to X-rays, but this does not degrade its performance in any noticeable way.

Mounted onto the clamp, which is at the end of the cold finger, is the sample cell and the assembly which connects it to the fill line. Mounted on the assembly closest to the cell is a copper ring that holds another Si diode thermometer, sensor B [14]. This thermometer measures the temperature of the cell and, correspondingly, the crystal.

The fill line leaves the sample cell assembly at the end farthest from the cold finger. The fill line makes a loop next to the fitting to relieve stress before following the axis of the sample cell through the region of irradiation, staying in line with the strut of the inner radiation shield. This 60 cm fill line has to leave the Displex head through a modified feed-through fitting. Since the fill line goes from room temperature at the feed-through to sample temperature at the cell, it is the major source of heat to the cell. There is no way to anchor the fill line to the cold finger to reduce heat flow, since that would cause the helium to freeze at that anchor point, causing a blockage in the fill line.

The fill line has wrapped on it a heater wire of 98 Ω/m manganin in the region from the cell to the outer radiation shield. This is connected to a variable current supply on the outside. This heater can be used to add further heat to the sample cell, by way of the fill line.

3.4 Electronics

Many pieces of electronics were used during the experiments. Most monitored and set the conditions of the measurements, such as pressure and temperature. There were electronics pertaining to the use of the X-ray source, and those will be discussed later in that section.

Two different temperature controllers are used, one for controlling the Displex's temperature and the other acting as a thermometer [16]. The one acting as the Displex controller connects to sensor A, in addition to the normal way it was connected by the manufacturer to the control thermometer and the cold finger heater wire. The other controller connects to sensor B, which is the most important sensor; this controller has the calibration curve for sensor B entered into it.

The heater wire to the fill line connects to a current supply [17]. The current is adjusted by hand and is normally used only during crystal growth.

The strain gauges that are mounted on the strain gauge cell (SGC) connect to a strain gauge

meter [18] by way of a shielded twisted-pair cable. The four strain gauges and the meter form a full strain gauge bridge, with two extra leads that compensate for the resistance in the leads themselves [19]. The meter is very accurate and is set to maximum sensitivity, as it measures the strain voltage across the bridge. It produces a voltage between -2 and 2 V, which is proportional to the strain voltage. There is also a LCD readout on the meter, but it is rarely used.

The output voltage from the strain gauge meter is connected to and measured by a digital multimeter [20]. The sensitivity of this measurement has one more digit than the readout of the strain gauge meter. This last digit is not wholly accurate, however, as it fluctuates for half the range of this last digit; this added sensitivity is needed to see the pressure drop that occurs when the helium freezes.

A PC computer running Microsoft Windows is used to interface with the Displex temperature controller. It is also used to log certain data: the strain gauge voltage; the set point temperature for the Displex; the temperatures of sensors A, B, and the control sensor; and the time. The program that acts as interface and data-taker was written using LabWindows/CVI [21]. In order for the PC to interface with the two temperature controllers and the digital multimeter, the PC has a GPIB card [22] installed inside of it, which uses special cables and the GPIB communication protocol to "talk" to these instruments.

3.5 X-ray source

The X-ray sources used in these experiments were synchrotrons. One beamline used was X-14A at the National Synchrotron Light Source, which is located at Brookhaven National Laboratory in Upton, New York. The beamline 1-BM-C was also used at the Advanced Photon Source, which is located at Argonne National Laboratory in Argonne, Illinois.

There is one reason why a synchrotron must be used instead a rotating anode source: flux. For our purposes, a synchrotron beamline is roughly six orders of magnitude brighter (for a bending magnet beamline, as described later). We need this high flux in order to see the weak, large Q-valued peaks; without these peaks, the Q range is severely limited, and the resulting Debye-Waller measurements have large errors.

There are also several reasons why a synchrotron makes this experiment much simpler. First, a synchrotron beamline's optics allow the energy of the beam at the sample to be tuned (2–40

keV for X-14A, and 6–20 keV for 1-BM-C), simply by changing the angles of the monochromator crystals; with a rotating anode source, one has to choose energies from the characteristic X-ray energies of the target element. The length of the beamline and all the optics at a synchrotron result in an X-ray beam that is less divergent and has much less background. Radiation coming from a synchrotron is naturally polarized, thus simplifying the analysis of the data afterwards. The use of a monochromator results in a high energy resolution, which gives a high Q resolution.

There are some negative things that one must contend with at a synchrotron. There are few synchrotrons and many people wanting to use them, so one can only get a limited amount of time at a beamline; if something goes wrong, you will most likely have to wait at least a half a year to try again. Since the X-rays at a synchrotron come from a current of electrons or positrons in the ring, and this current decays, the incident X-ray flux is constantly decreasing; thus, the incoming flux needs to be measured at all times with a beam monitor. Another annoyance is that the beam may 'wander', due to the current changing its position in the ring; if an experiment depends on the beam being at the exact same position at all times, this can cause problems.

At a synchrotron, there are both bending magnet beamlines and insertion device beamlines. A bending magnet is one of the many magnets that bend the current in the ring into a circle; every synchrotron has these beamlines since these magnets must be in place. An insertion device is something put into the current ring that ideally does not change the direction or energy of the particles in the ring (electrons at the NSLS or positrons at the APS), and the insertion device results in a better quality of produced X-rays. They are made by lining the beam channel with pair after pair of magnets, with each pair creating a magnetic field in one direction, and the direction of the magnetic field reversing with each subsequent pair. This alternating magnetic field causes the trajectories of the electrons or positrons in the ring to bend back and forth, creating X-rays with each bend. This results in a brighter and more focused X-ray output than that of a bending magnet. There are two different types of insertion devices, wigglers and undulators. Wigglers are optimized for sheer number of photons produced, with the energy of the resulting X-rays varying greatly. An undulator is optimized for a particular narrow energy range, but at the cost of the total number of photons produced.

Insertion device beamlines create much more X-rays than a bending magnet beamline. However, this experiment does not need the undulator's high energy resolution, nor would it make

efficient use of a wiggler's wide range of photon energies. This is important, since demand for beamtime at an insertion device beamline is greater than the demand for beamtime at a bending magnet beamline. From previous experience, the flux produced at a bending magnet beamline is quite sufficient for the experiment that is the subject of this thesis, so that is what was used.

The choice of photon energy is important to the experiment since it determines the diffraction angle, 2θ, for each reflection. In order to try to spread the reflections out, so as to get a good resolution, the energy of the photons is set high. However, the energy should not be set too high, since for any particular reflection, there is a cutoff energy above which the peak is no longer visible. Therefore, the highest Q reflection that can be realistically measured needs to be considered. In terms of practicality in dealing with all the equipment and the detector, we did not want to go above a 2θ of 90°, since there was a danger of the Displex running into the diffractometer, or the diffractometer running into upstream optics (slits, ionization chamber, beampath, etc.). Amidst all of this, there is also the consideration that the Lorentz polarization factor we use, $(\sin(2\theta))^{-1}$, is at a minimum at a 2θ of 90°. Based on the above considerations, the energy that was used in all measurements was 16.00 keV.

3.5.1 Beamline design

The beamlines used (X-14A at the NSLS [23] and 1-BM-C at the APS [24]) both had very similar designs. Figure 3.5 is a drawing of the beamline optics of both beamlines.

Once leaving the ring, the photons encounter a cylindrical grazing incidence mirror, which has the axis of curvature horizontal and perpendicular to the beam; this mirror focuses the beam in the vertical direction, and also absorbs all photons that have an energy above a critical value determined by the scattering angle. At X-14A, the mirror is made out of aluminum which is coated by nickel, then platinum. At 1-BM-C, the mirror is palladium coated, water-cooled, and is set so the critical energy is 24 keV.

After the mirror, the beam goes through a beryllium filter, which helps to cut out the unwanted lower energy photons, and consequently takes a high heat load because of this.

The next piece of optics is a double crystal monochromator, which use silicon crystals with matching reflection planes of (1 1 1), with the photons leaving the monochromator in the same direction as they entered. At 1-BM-C, it is also possible to use either the (2 2 0) or (4 0 0) reflection.

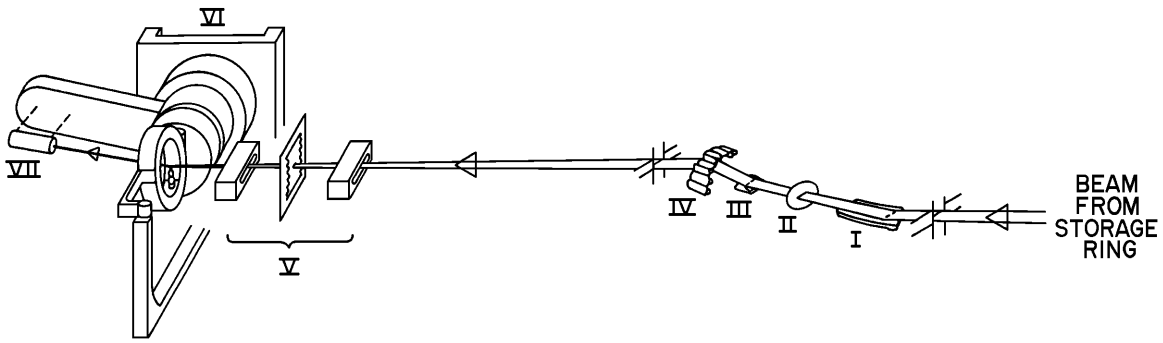

Figure 3.5: Drawing of the beamline optics, with distances not to scale and angular relationships incorrect. I) Mirror, cylindrical with axis perpendicular to beam direction, which vertically collimates the beam and also sets a critical energy above which photons won't be reflected. II) Beryllium filter. III) First silicon monochromator crystal, which selects the photons' energy, and is water-cooled. IV) Sagitally bent second silicon monochromator crystal, which focuses the beam horizontally. V) Ionization chambers used as beam intensity monitors. VI) Four or six circle Huber diffractometer. VII) Detector. The beamline optics for 1-BM-C at the APS also has a mirror similar to I immediately after IV, which focuses the beam vertically; X-14A at the NSLS has this same type of mirror, but it was not used.

The first crystal is a flat piece of silicon. Its angle, relative to the incoming beam, is tuned to what is needed for the desired energy, with the rest of the photons (except for harmonics) getting absorbed, creating a large amount of heat, which is removed by water cooling. The second crystal is sagitally bent, so as to focus the beam horizontally. This crystal is set to the same angle as the first. The bending radius of this bent crystal can be adjusted, so as to change the horizontal focus, such as to the sample position.

At this point, the beam is not horizontal, due to the beam being scattered at a small angle at the first mirror. At both beamlines, there is a vertically focusing mirror at this point which also reflects the beam down by the same angle as the first mirror. This mirror is optional and can be removed if not wanted. Since we used a large beam at X-14A, this mirror was not employed; instead, the entire beamline after the first mirror was rotated about the first mirror, in order to match this angular offset. At 1-BM-C, where we had a narrowly focused beam, this second vertically focusing mirror was employed.

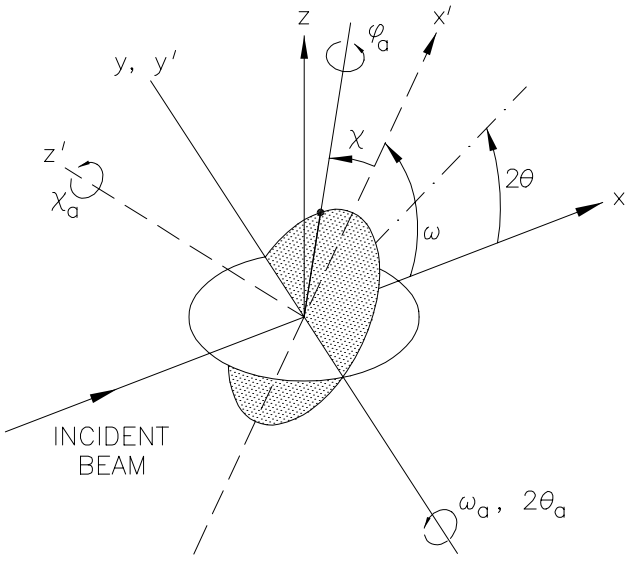

Figure 3.6: Diagram showing the geometry and relations of the angles 2θ, ω, χ, and ϕ, which make up the degrees of freedom for the four-circle diffractometer.

3.5.2 Diffractometer

The crystal needs to be in the center of the beam, with provisions for rotating the crystal into any orientation, and there also has to be a way to rotate a detector about the crystal's center. What is needed is a goniometer; at both beamlines, a Huber diffractometer [25] is used. At the NSLS, a four-circle diffractometer with a split-ring χ circle is used; at the APS, a six-circle diffractometer is used (with only four of the circles in use).

Three of the four circles are used to orient the crystal, while the last is used to rotate the detector about the crystal's center. The detector uses what is normally labelled the 2θ circle. The circle's axis of rotation is horizontal and perpendicular to the beampath. There is an arm on the circle, with the detector mounted on its end. The description of the three orientation circles will be from the outside to the inside, as the circles are nested within one another. First, there is the ω circle, which has the same rotation axis as 2θ. Then there is the χ circle, whose axis of rotation is always perpendicular to ω's. Lastly, there is the ϕ circle, whose axis of rotation is always perpendicular to χ's. The Displex is mounted directly onto the ϕ circle. Figure 3.6 is a diagram showing the geometry of these angles.

When it comes to the positions of the motors, it is important to understand the distinction between the software values of the positions and the hardware values of the positions. The software

values are those that are stored inside the computer program that controls the motors themselves. The hardware values are those that are physically present on the counters that are mounted next to the motors. The two values for a motor do not have to agree, since that would assume that the motor positions are perfectly calibrated; in reality, there are small offsets to the motor positions that need to be accommodated, and these correct values are stored in the software. Even if the values did correspond perfectly, sometimes it is beneficial to define an offset and multiplier to the actual value. Even though the hardware and software values don't have to agree, the relationship between the two needs to be recorded; if the software values become corrupted, they can be regained from the counter readings.

In order to change the crystal's orientation so that a reflection can be brought into the detector's angular view, only two circles are needed. The third circle is useful in the case that bringing the other two circles to desired values is physically impossible due to physical constraints of the equipment; this third circle can be changed to avoid the obstruction in some cases. The third circle is also useful if one wants to rotate the crystal around the reflection. In general, ω and χ move while ϕ is set fixed.

Before the experiment can start, the diffractometer needs to be set up. This entails aligning the beam and diffractometer with respect to one another, setting up the software values for the motor positions, mounting the detector, and setting up the slits. The Displex also needs to be mounted onto the diffractometer. All of this is described in Appendix G.1.

Many things become mounted onto the diffractometer when setting up the experiment. The Displex is mounted onto the ϕ circle, and has high pressure helium supply and return lines, electronics cables, high pressure sample fill line, and a vacuum line coming off of it. There are also detectors, slits (motorized and fixed), flight paths, attenuators, and ionization chambers mounted either on or near the diffractometer. This creates a problem in that it is easy for one thing mounted on the diffractometer to run into something else. This needs to be taken care of by judging and setting the limits of the motors. This procedure is described in Appendix G.3.

3.5.3 Hutch Equipment

There are a variety of equipment used inside the experimental hutch. Figure 3.7 shows the relative positions of most of them.

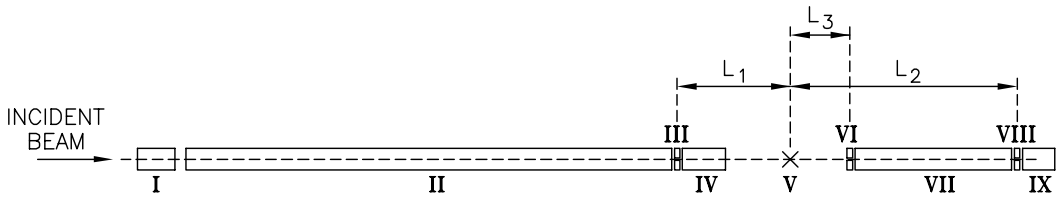

Figure 3.7: Diagram of the positions of equipment in the hutch. I) Ionization chamber $I_0 0$. II) Flight path. III) Motorized sample slits. IV) Ionization chamber I_0. V) Sample position. VI) Scatter slits. VII) Flight path. VIII) Motorized detector slits. IX) Detector. The lengths shown for the NSLS are $L_1 = 22.2$ cm, $L_2 = 54.2$ cm, and $L_3 = 13.0$ cm, while the lengths for the APS are $L_1 = 30.0$ cm, $L_2 = 77.8$ cm, and $L_3 = 20.3$ cm.

The detector used depends on where the experiment was conducted. At the NSLS, a xenon-filled proportional counter was used; at the APS, a NaI scintillation counter was used. Neither detector has a very large dynamic range, making the use of incident beam absorbers mandatory. The detector gives out a voltage pulse for each photon detected, with it magnitude proportional to the photon energy. Electronics are used to set a voltage window that extends from just above and just below the voltage corresponding to the desired photon energy. This window will exclude noise which is at low voltages; it also excludes the photons of harmonic energies that pass through the monochromator, which will be a multiple of the desired energy.

In order to compensate for the poor scaling of the detectors and the fact that the peak intensities vary greatly with Q, attenuators had to be used. At the NSLS, the attenuators were made of aluminum alloy and copper; at the APS, the attenuators were made of molybdenum and copper. A precise measurement of the absorber thickness would have to be made in order to use the standard formula for finding the absorption (see Appendix A), but the actual absorptions were instead measured directly with the X-ray beam (see Appendix G.5); for the aluminum alloy attenuators, the absorptions had to be measured directly, since the alloy composition is unknown. In order to change what absorber is in the beampath, some sort of device has to be employed: at the NSLS, a wheel is used, which is run by a stepping motor that had different absorbers mounted at different positions; at the APS, an air actuated spring-loaded absorber mount was used, which fits inside of a pumped out beam path, where each attenuator can be inserted or extracted individually. Unfortunately, during both runs, we had to insert some extra absorbers by hand, since diffracted intensity variations were very large.

In order to compensate for the varying photon flux due to the changing ring current, the

amount of photons incident upon the sample has to be measured with a monitor. This is done by use of a nitrogen-filled ionization chamber that is in the path of the X-ray beam. The chamber is designed to absorb as little of the photons as possible, having a Kapton window for the entering and leaving of photons to the chamber. The nitrogen is kept constantly flowing through the chamber, which is supplied by a bottle with a regulator. As the X-rays travel through the nitrogen filled cavity, a small percentage of the photons are absorbed by the nitrogen, ionizing the atoms. On opposite sides of the chamber are two electrodes, which have an applied voltage differential; these electrodes draw the oppositely charged particles to them, creating a current in the electrical circuit. This current is proportional to the flux passing through the chamber. This current is measured by a current amplifier, which produces a voltage proportional to the current, which is then measured and converted into a count rate. The ionization chamber does attenuate the flux a small amount, but that can be measured, and since it scales linearly with the flux, it doesn't matter for this experiment.

There was another detector used, a PIN diode, which uses an applied voltage, similar to that of an ionization chamber. It is used for aligning the beam, since it can take the abuse of the direct beam without getting damaged, unlike the normal detectors used. It is subject to thermal drift and has poor sensitivity, which is why it is not used for taking data.

Slits are very important, and at two least two motorized sets are essential. One puts a set of slits where the beam enters the hutch, opened somewhat wider than the desired beamsize, which blocks out undesired background radiation. One employs one pair of motorized slits just before the sample, which sets the size of the beam as it hits the sample and also helps to block background radiation. On the detector arm after the sample, there is a flight path. One puts a set of slits on the front end, opened wide horizontally, but narrow vertically. A motorized set is at the other end, just in front of the detector. The separated slit pairs on the detector arm mask off any photons that come from anything that is not close to the sample, since photons have to be able to pass both sets of slits which are centered on the sample (if aligned correctly), thereby eliminating a good deal of background. This elimination is vital, since the beam has to pass through both Lexan and beryllium before reaching the sample and is scattered by both. The slit set directly in front of the detector needs to be motorized so it can go between closing down when centering a peak to a high precision and opening up when taking an integrated intensity scan.

References

[1] C. T. Venkataraman, Ph.D. thesis, University of Illinois at Urbana-Champaign, 1996.

[2] C. T. Venkataraman and R. O. Simmons, Rev. Sci. Instr. **67**, 3365 + CD (1996).

[3] A. T. Macrander, Ph.D. thesis, University of Illinois at Urbana-Champaign, 1977.

[4] The 60,000 PSI and 15,000 PSI valves, fitting, and some of the tubing came from High Pressure Equipment, Inc., 1212 Linden Ave., Erie, PA 16505.

[5] This smaller tubing comes from Superior Tube, Norristown, PA 19404.

[6] The Bourdon tube gauge is the 50,000 PSI model CM from Dresser Industries, Instrument Division, 153 S. Main St., Newtown, CT 06470.

[7] The stacked rosette strain gauges are model WK-06-120WT-120 from Measurements Group Inc., PO Box 277777 Dept. TR, Raleigh, NC 27611.

[8] The compressor is model 46-14021-2 and is manufactured by the Superpressure division of Newport Scientific, Inc., 8246-E Sandy Court, Jessup, MD 20794-9632.

[9] The leak detector is model HLT-160 and is manufactured by Balzer's High Vacuum Products, 8 Sagamore Park Road, Hudson, NH 03051.

[10] The I-250 beryllium was supplied by Brush-Wellman Inc., Elmore, Ohio 43416.

[11] These formulae came from a personal communication with W. B. Daniels.

[12] The machining of the sample cell was done by Speedring, a subsidiary of Precision Aerotech, Inc., 6717 Hwy 157, PO Box 1588, Cullman AL 35056.

[13] The HC-2 compressor and DE202 expander module are manufactured by APD Cryogenics Inc., 1833 Vultee St., Allentown, PA 18103.

[14] Both sensors A and B are of the same type and origin. They are DT-470-SD-13-1.4LS Si diode sensors, manufactured by Lake Shore Cryotronics, Inc., 64 East Walnut St., Westerville, OH 43081-2399.

[15] Lexan is a polycarbonate which is a high performance engineering thermoplastic characterized by high clarity, high heat and flame resistance, dimensional stability, and exceptionally high impact strength over a wide temperature range. Lexan is the trade name for the product manufactured by General Electric Co.

[16] Both temperature controllers came from Lake Shore Cryotronics, Inc., 64 East Walnut St., Westerville, OH 43081-2399. We used model DRC-93CA as our controller, and model 330 as our thermometer.

[17] The 60 W current supply is model E3616A manufactured by Hewlett-Packard Company, 5201 Tollview Drive, Rolling Meadows, IL 60008.

[18] The bridge is a DMD-20 strain gauge meter, manufactured by HBM Inc., 19 Bartlett St., Marlboro, MA 01752.

[19] T. Potma, *Strain Gauges: Theory and Application* (Centrex, Eindhoven, 1967).

[20] The multimeter is model 8840A manufactured by John Fluke Mfg. Co., Inc., PO Box C9090, Everett, WA 98206.

[21] LabWindows/CVI is a C-based programming environment that is specially developed for creating data-taking programs on Microsoft Windows personal computers and Sun workstations. The program is licensed from National Instruments Corporation, 6504 Bridge Point Parkway, Austin, TX 78730-5039.

[22] The General Purpose Interface Bus (GPIB), aka IEEE 488, is a bus protocol that allows a computer to remotely control GPIB-supported electronic devices. A GPIB card is installed in the computer, which is connected to the devices with special cables. The card was supplied by National Instruments Corporation, 6504 Bridge Point Parkway, Austin, TX 78730-5039.

[23] A. Habenschuss, G. E. Ice, C. J. Sparks, and R. A. Neiser, Nucl. Instrum. Meth. A **266**, 215 (1988).

[24] Information on 1-BM-C came from a personal communication with Jonathan Lang.

[25] Huber diffractometers are distributed in the U.S. by Blake Industries, Inc., 660 Jerusalem Road, Scotch Plains, NJ 07076.

Chapter 4

Data

4.1 Integrated Intensity Data Collection and Correction

Since the property that is being measured is the Debye-Waller factor, which relates the peak intensity of different reflections, integrated intensity measurements are made at reflections. Depending on the type of measurement, either many different reflections are measured at a given temperature (Q-dependent), or one reflection is measured at many different temperatures (T-dependent).

The data is collected by taking rocking curves of reflections. In order to take rocking curves, reflections need to be found and centered; this is a tedious process which involves searching for several reflections and creating an orientation matrix, as described in Appendix G.8. A centered reflection implies that the ω, χ, and ϕ motors are at values where the desired plane of reflection in the crystal is at the correct Bragg angle with respect to the beam, and that the 2θ motor is at a value such that the detector is at twice the correct Bragg angle with respect to the beam.

Rocking curves are taken by scanning the ω motor through the peak, from the tails on one side of the peak to the other. During the scan, the ω motor will stop periodically as determined by the step size, and during this stop, the detector records the number of diffracted photons that strike it. The length of the pause at each stop is determined by either a time gate or a monitor count gate. During the scan, all motors other than ω are kept still.

At this point, the scan has to be corrected at each individual scan point for two experimental difficulties: the effects of dead time, and the variations in the incident flux as measured by a monitor. Once this is done, the background in the scan needs to be subtracted, which takes into account the attributes of the scan shape itself.

Once this is done, all that should be left is a peak that goes to zero on both sides. The area under the peak is integrated, giving a raw integrated intensity value for the reflection.

Since these integrated intensity values are to be compared to one another, the effects of the

different conditions of the scans on the intensities need to be corrected for. If the measurement involved more than one single attenuator, the effect of the absorption of the incident beam needs to be adjusted. Since the crystal is not spherical and is oriented differently in the beam for each reflection, a varying volume of helium is illuminated, causing varying numbers of electrons to interact with the photons, depending on the angles of the sample cell in the beam; this volume change needs to be taken out.

At this point, the differences in intensities between the different reflections is that of the theoretical formula for the intensities of elastic peaks:

$$I_i \propto I_0 \, F^2 \, e^{-Q^2 \langle {u_Q}^2 \rangle} \, L. \tag{4.1}$$

Since the property that is being investigated is the Debye-Waller factor, $e^{-Q^2 \langle {u_Q}^2 \rangle}$, the other factors need to be removed from the measured integrated intensities. These factors are the structure factor, F^2, and the Lorentz polarization factor, L. Once those are gone, the ratio of two different measurements is due to the Debye-Waller factor.

4.1.1 Dead Time Correction

X-ray detectors that were used are of the scintillation counter variety. Each time a photon strikes it, an electrical pulse, whose maximum voltage is proportional to the energy of the photon, is sent to the detector electronics. The electronics are set to count only pulses of a certain height range, in order to weed out the background and the photon harmonics. The pulse sent has a temporal width, and if any any other photon hit the detector at the same time, the electronics only sees one count (or none if the combined pulse height is higher than the window maximum).

This is a problem that worsens as the count rate increases, since the probability of photons striking the detector within one pulse width, or dead time, increases. This nonlinear response of the detector at high flux can be dealt with by measuring the dead time τ of the detector and correcting the count rate with

$$n_{\text{true}} = -\frac{1}{\tau} \ln(1 - \tau \, n_{\text{obs}}) \simeq \frac{n_{\text{obs}}}{1 - n_{\text{obs}} \, \tau} \tag{4.2}$$

where n_{obs} is the measured count rate, and n_{true} is the true count rate. The procedure for the measurement of the characteristic dead time of the detector, is in Appendix G.4. The measured

dead time for the detector used at X-14A was 5.6 μs, while the dead time for the detector used at 1-BM-C was 0.10 μs.

So, the correction is made by using Eq. 4.2 for each individual scan point. Because of the need for the count time in the equation, the time of each count needs to be recorded during a scan. A time gate can be set to a desired value so that every count last the specified time. If the gate used for counting is the monitor, the count time will vary.

4.1.2 Incident Flux Monitor Correction

The flux that reaches the sample can vary over time, due to such things as the current in the storage ring decreasing with time, changes in the orbit of the electrons (or positrons) in the storage ring, or changes in temperature of the monochromator.

The way to compensate for this is to have an incident flux monitor in the beamline, ideally after the sample slits. This monitor measures the flux that passes through, and is recorded simultaneously when the main detector is being used. To correct for this varying flux, the detector count is divided by the monitor count for every individual scan point.

The monitor can be set up as the count gate, such that a count is terminated when the monitor count reaches a certain value.

4.1.3 Background and TDS Subtraction

There are two different types of background that needed to be subtracted. Background caused by scattering from the helium crystal and the background caused by scattering from everything else.

The scattering from everything non-helium is normally relatively flat over the range needed for an integrated intensity curve. There is the worry about beryllium peaks, but since rocking curves do not involve a change in 2θ, the intensity caused by a beryllium peak should not vary throughout the scan.

The background caused by the helium crystal comes in several forms, although only two are really important. The first is Compton scattering, which is inelastic scattering by electrons. The other type is thermal diffuse scattering (TDS), which is inelastic scattering from phonons in the crystal.

The background due to Compton scattering is diffuse. It is a decreasing function as Q increases,

with no peaks of any kind. Within the small scan ranges of the rocking curves, the Compton scattering background is constant; a rocking curve leaves 2θ fixed during the scan, so the Compton component of the photons detected should remain fixed.

The background due to TDS is much more complex. As discussed in Sec. 2.1.4, first order TDS is caused by interaction with one phonon (either creating or destroying), second order TDS involves two phonons, and so on. The background due to TDS has peaks, and they are at a maximum at the positions of elastic peaks, making them troublesome when trying to remove them. The second order TDS is extremely weak, and has very broad peaks, so all orders over one can be ignored. The first order TDS has somewhat sharp peaks, with the ratio of the TDS counts to elastic counts increasing as Q increases. The effect of not correcting for TDS on lattice parameters is negligible, but the effect upon the Debye-Waller factor is to reduce it, underestimating the motion of the atoms [1].

The theory of first order TDS contribution to integrated intensity scans has been studied [2], with strategies given on how to subtract it. The methods are quite complex, depending on the elastic constants of the crystal, the divergence of the X-ray beam, the solid angle of the detector, the width of the scan, etc. There are several programs available for calculations [3] and there are ways of doing rough TDS estimates [4] if the exact elastic constants are known.

However, it has been shown that with the advent of synchrotron radiation, the amount of contribution of TDS to the measured integrated intensity scan is reduced to a negligible contribution, as compared to a traditional X-ray tube [5]. This is due to the small divergence of the X-ray beam and the sharp peaks from the crystal, which allow for a small solid angle for the detector and small scanning ranges. Because of these considerations, TDS calculations won't be done on the data.

So, in order to correct for background, the first thing that needs to be done is look at the background scan at the same position, when the crystal is melted, in order to see if the background is nonlinear. If the background is linear (it always was for this experiment), the background of a scan was removed by simply going to the tails of a peak, and subtracting the amount under the straight line through the tails. If the background is not linear, the background scan has to be scaled to the data scan, and subtracted.

4.1.4 Scan Integration

Integration of the scan is done by multiplying each adjusted detector value by its step size (to give the area of the column), and then summing all of them together. In theory, the number of steps summed is irrelevant, since it is assumed that the peak went to zero at the boundaries of the scan. Since the step size does not change during a scan, it is more convenient to find the integrated intensity by

$$I_{\text{int}} = \frac{\Delta\omega}{N} \sum_{i=1}^{N} c_i \tag{4.3}$$

where N is the number of scan points, $\Delta\omega$ is the total scan width, and c_i is the adjusted detector count at the i^{th} scan point.

4.1.5 Attenuator Correction

The detectors used have a maximum count rate, after which they are unreliable, even with dead time corrections. Because there is around a factor of one million in intensity difference between the low Q peaks and the high Q peaks, and the dynamic range of the detector is around a thousand, there have to be attenuators in the beam for the brighter peaks.

The attenuators came from different materials. The absorption of each attenuator was measured directly (see Appendix G.5), and the theoretical value was computed from the thickness and the linear absorption coefficient (see Appendix A) as a check. To correct for the attenuators, the intensity of the peak is divided by the experimental absorption of the attenuator.

4.1.6 Volume Corrections

When measuring the rocking curves for different reflections, there is a problem caused by the fact that going to the different motor positions changes the angle between the cell and the oncoming beam. Changing this angle causes the volume illuminated by the X-ray beam to likewise change; this in turn causes the reflected intensity to change. This can be accommodated by computing the volume for each configuration and dividing it from the intensity. The actual volume is not required, but a ratio to some reference is. The reference value will be the minimum volume possible.

An assumption has to be made about the size of the beam cross-section at the sample's position (called the beam spot). There are two different conditions corresponding to different experimental

runs, which leads to two different cases. Neither condition gives an exact result, especially since it assumes that the flux density distribution is constant across the beam spot.

In order to find the ratio relations, matrices are used. A right-handed rectilinear coordinate system is set up as following: $\hat{\mathbf{x}}$ is towards the X-ray source, $\hat{\mathbf{y}}$ is towards the ring, and $\hat{\mathbf{z}}$ is up. The unit vector representing the cell axis needs to be set up,

$$\mathbf{\Psi}_{\text{cell}}(\omega = 0, \chi = 0) = \begin{pmatrix} 0 \\ -1 \\ 0 \end{pmatrix}. \tag{4.4}$$

The vector is created for the case when $\omega = 0$ and $\chi = 0$, and is generalized through the use of rotation matrices. The two matrices used for rotations of the cell axis vector in ω and χ need to be set up,

$$\Omega_{\chi,\omega=0} = \begin{pmatrix} 1 & 0 & 0 \\ 0 & \cos(\chi) & \sin(\chi) \\ 0 & -\sin(\chi) & \cos(\chi) \end{pmatrix} \quad \text{and} \quad \Omega_{\omega} = \begin{pmatrix} \cos(\omega) & 0 & \sin(\omega) \\ 0 & 1 & 0 \\ -\sin(\omega) & 0 & \cos(\omega) \end{pmatrix}. \tag{4.5}$$

A rotation matrix for ϕ is not needed since it is only the identity matrix. The matrix for χ is set up assuming $\omega = 0$, and must be applied first.

The rotation matrices are applied to the cell axis vector in the correct order to get a general value for any χ and ω,

$$\mathbf{\Psi}_{\text{cell}}(\omega, \chi) = \Omega_{\omega}\, \Omega_{\chi,\omega=0}\, \mathbf{\Psi}_{\text{cell}}(0, 0) = \begin{pmatrix} \sin(\omega)\sin(\chi) \\ -\cos(\chi) \\ \cos(\omega)\sin(\chi) \end{pmatrix}. \tag{4.6}$$

Very Small Beam Spot

The assumption in this case is that the beam spot will be considered to be infinitely narrow, allowing the volume to be proportional to the length of the beam's path through the cell. The beam can be

represented by a unit vector corresponding to the beam direction,

$$\mathbf{\Psi}_{\text{beam}} = \begin{pmatrix} -1 \\ 0 \\ 0 \end{pmatrix} . \tag{4.7}$$

The actual value that expresses the ratio is the inverse of the sine of the angle between the cell's axis and the direction of the incident X-ray beam. The sine of this angle is obtained from the absolute value of the cross product between the cell axis vector and beam direction vector. The cross product results in

$$\mathbf{\Psi}_{\text{beam}} \times \mathbf{\Psi}_{\text{cell}}(\omega, \chi) = \begin{pmatrix} -1 \\ 0 \\ 0 \end{pmatrix} \times \begin{pmatrix} \sin(\omega)\sin(\chi) \\ -\cos(\chi) \\ \cos(\omega)\sin(\chi) \end{pmatrix} = \begin{pmatrix} 0 \\ \sin(\chi)\cos(\omega) \\ \cos(\chi) \end{pmatrix} . \tag{4.8}$$

Taking the length of this vector and inverting, the resulting ratio of the volume to its minimum is

$$\text{ratio} = C_{\text{S}}(\omega, \chi) = \frac{1}{\sqrt{\cos^2(\chi) + \sin^2(\chi)\cos^2(\omega)}} . \tag{4.9}$$

This formula is used for the data taken at the APS, where the beam spot was very small, being around 0.2 mm square. The application of this correction made the linear fits for the data better in all cases.

Very Wide Beam Spot

The assumption in this case is that the beam spot will be considered to be infinitely wide with a infinitely thin height, allowing the volume to be proportional to the area of the beam's path through the cell. The beam can be thought of as a plane, with an associated normal,

$$\mathbf{\Psi}_{\text{normal}} = \begin{pmatrix} 0 \\ 0 \\ 1 \end{pmatrix} . \tag{4.10}$$

The actual value that expresses the ratio is the inverse of the cosine of the angle between the cell's axis and the incident X-ray beam's normal. The cosine of this angle is obtained from the value of the dot product between the cell axis vector and the beam's normal vector,

$$\mathbf{\Psi}_{\text{normal}} \cdot \mathbf{\Psi}_{\text{cell}}(\omega, \chi) = \begin{pmatrix} 0 \\ 0 \\ 1 \end{pmatrix} \cdot \begin{pmatrix} \sin(\omega)\sin(\chi) \\ -\cos(\chi) \\ \cos(\omega)\sin(\chi) \end{pmatrix} = \cos(\omega)\sin(\chi)\,. \tag{4.11}$$

Taking this value and inverting, the resulting ratio of the volume to its minimum is

$$\text{ratio} = C_{\text{W}}(\omega, \chi) = \frac{1}{\cos(\omega)\sin(\chi)}\,. \tag{4.12}$$

This formula corresponds to the data taken at the NSLS, where the beam spot was broad, being around 2 mm wide and 1 mm high. For the crystal diameter of 0.813 mm, χ needs to fall in the range $48^\circ < \chi < 132^\circ$ in order for this approximation to hold. For the NSLS data, where the χ values were very restricted, this condition is satisfied.

This approximation is not applied to the data, however, since its application makes a linear fit through the data worse for most measurements. This is most likely due to the fact that this approximation assumes a single crystal inside of the sample cell, which is not always reality. There are normally several crystals illuminated with a large beam, and an increase in helium illuminated does not automatically mean an increase in illumination for a crystal.

4.1.7 Lorentz Factor

For horizontally polarized light, the Lorentz factor is

$$L(\theta) = \frac{1}{\sin(2\theta)}. \tag{4.13}$$

Using the value of 2θ, the value of L for each reflection can be easily computed. The intensity is then divided by L.

4.1.8 Structure and Form Factors

The structure factor has to be removed from the intensity measurements. The structure factor is always some constant multiplied by the squared form factor (see Appendix D.1).

The constant for fcc can be taken as unity, but the relationship for the hcp peaks is more difficult, since it is not a true Bravais lattice. Once the constant is found, the intensity value is divided by it.

The form factor depends on the value of Q, which comes from the value of 2θ and λ. The form factor is found using fits to calculated form factors [6] and the intensity is divided by its square.

4.2 Determination of Lattice Parameters

The lattice parameters are useful to know for a couple of reasons. They are used to compute the molar volume, and in the case of hcp, the c/a ratio is used to test whether the crystal is ideally close packed.

A source of error for lattice parameter measurements is an offset in the 2θ angle. Should either the detector slits or the scatter slit become slightly off center, the offset in 2θ will occur. This effect shows up in the lattice parameter values as a constant increasing or decreasing of values with increasing 2θ angle. This can be fixed by adding a constant to 2θ for each reflection, and recomputing the lattice parameters; this is done until there is no increase or decrease of the values in 2θ. This offset is then also applied to the Debye-Waller data to improve the Q values.

In order to find the lattice parameters for a crystal using only the knowledge of the crystal structure and the elastic peaks, the θ value of a reflection must be found and the corresponding h, k, and ℓ values must be known, as well as the wavelength of the photons, λ. The resulting relations come from Bragg's Law and the interplanar distance formulas.

4.2.1 fcc Lattice Parameter

There is only one lattice parameter for a crystal structure based on a cubic lattice, such as fcc, and thus determining it requires only one reflection. The relation is

$$a = \left(\frac{\lambda}{2\sin(\theta)}\right)\sqrt{h^2 + k^2 + \ell^2}. \tag{4.14}$$

4.2.2 hcp Lattice Parameters

Since a crystal structure based on the hexagonal lattice, such as hcp, has two lattice parameters, it takes two reflections to determine them. However, the two reflections $(h_1\,k_1\,\ell_1)$ and $(h_2\,k_2\,\ell_2)$ have to fulfill the relation

$$\frac{{h_1}^2 + h_1k_1 + {k_1}^2}{{\ell_1}^2} \neq \frac{{h_2}^2 + h_2k_2 + {k_2}^2}{{\ell_2}^2} \tag{4.15}$$

in order to be able to be used. This condition simply determines if they come from the same family of reflections, since if they do, the information they contain is redundant.

The first thing is to define the variables

$$\rho_i \equiv {h_i}^2 + h_ik_i + {k_i}^2 \qquad \text{and} \qquad \xi_i \equiv {\ell_i}^2 \tag{4.16}$$

in order to make the calculations easier. The relations for the lattice parameters are

$$a = \lambda\sqrt{\frac{1}{3}\left(\frac{\xi_1\rho_2 - \xi_2\rho_1}{\xi_1\sin^2(\theta_2) - \xi_2\sin^2(\theta_1)}\right)} \qquad \text{and} \qquad c = \frac{\lambda}{2}\sqrt{\frac{\rho_1\xi_2 - \rho_2\xi_1}{\rho_1\sin^2(\theta_2) - \rho_2\sin^2(\theta_1)}}\,. \tag{4.17}$$

It is possible to get one of the two lattice parameters from a single reflection, but it needs to be a reflection that is totally in the h and k directions ("pure a reflection") or totally in the ℓ direction ("pure c reflection"). For a $(h\,k\,0)$ reflection, the lattice parameter is

$$a = \left(\frac{\lambda}{\sin(\theta)}\right)\sqrt{\frac{h^2 + hk + k^2}{3}}, \tag{4.18}$$

while for a $(0\,0\,\ell)$ reflection, the lattice parameter is

$$c = \left(\frac{\lambda}{2\sin(\theta)}\right)\ell\,. \tag{4.19}$$

4.3 Experimental Errors

As in all experiments, error was introduced into the measurements. Some errors could have been avoided, while others could not.

4.3.1 Error Associated With Integrated Intensity Scans

One type of error that was beyond our control was crystal stability. As described in Appendix G.7.5, helium crystals are very soft and can do strange things during a set of measurements. The illuminated crystal can increase or decrease in size due to crystal boundary movements. A mosaic reflection is very susceptible to this. The scans taken during the T-dependent are very susceptible to this problem, since changing the temperature makes the crystal more unstable.

Another uncontrollable error was stability of the incoming X-ray beam. It is assumed that the X-ray beam has a uniform flux distribution at the sample position, and that its position does not change. However, this depends very much on the position of the orbit of the electrons (or positrons) in the storage ring, since the direction of the X-rays as they reach the monochromator is determined by the orbit. Occasionally the orbit will change unexpectedly, but it normally will not change much, except for refills. When the ring is emptied and refilled, the orbits will be different; this is seen directly in the form of having to tweak the angle of the monochromator crystal in order to maximize the flux at the sample. When one is working with a wide beam (NSLS in our case), the flux distribution of the photons passing through the sample slits will change, altering results. When one is working with a narrow beam (APS in our case), the effect is that the beam position wanders, causing the beam to hit the sample cell off center, and illuminating different volumes of the cylindrical volume, again altering results. For these exact reasons, we would try to finish a set of measurements before the ring was emptied.

For the NSLS run, an error that could have been avoided involved with the ionization chambers that acted as incoming flux monitors. There were two of them, one positioned at the entrance to the hutch, and one positioned right in front of the sample position. The use of absorbers made the resulting values of the second monitor somewhat inaccurate, even though we thought we had compensated. The monitor values used then became the first monitor, with corrections coming in the form of absorption corrections. The error came from the fact that the first ionization chamber, since the beamline personnel deemed it of lesser value, was not hooked up to a nitrogen source, but was open to the atmosphere. This error is actually not terrible when comparing the monitor's values to the ring current, but there are subtle oscillations.

For the APS run, a mistake that probably added some error came after the χ circle was accidentally run into the beam path, upon which the sample slits were mounted. This misaligned

the slits with respect to the goniometer center. It was impossible to fix this error completely, since that would involve disassembling the Displex from the goniometer, which takes a long time, and half the allotted beamtime had already been used. This mistake was corrected to a good degree, owing to the fact the the displacement was almost entirely vertical. The vertical slits were scanned while 2θ was at the position of a beryllium ring, in order to look for a maximum intensity which would correspond to the center of the cell.

Another problem with the APS run was with the motors. When the motors were told to move to a specific value, they sometimes moved only partially or not at all. For most of the motors, this was not too big of a problem since it was normally obvious that the move did not occur. The one major exception was the case of the detector slits, which had to be set exactly the same for every scan, and it wasn't obvious if they were at incorrect positions. They were found to be wrong several times, and they were most likely wrong other times and weren't detected.

One last problem with the APS data occurred during the measurement of data set 12. The monochromator crystal was tweaked in order to maximize the flux at the sample. Upon doing so, it was noticed that the flux detected by the monitor and the counts in the detector for the last peak scanned were disproportionate. It seems the beam position would move when the monochromator was tweaked, which was not supposed to happen. To correct for this, the last scan before the tweak was redone, and all subsequent measurements were normalized to the difference between the two measurements of the same peak.

4.3.2 Error Associated With Lattice Parameter Determination

The main source of error for lattice parameter measurements is that for most of the peak centers used, only a 2θ scan was used to find the center with respect to 2θ. A radial scan should have been used instead; a radial scan is where 2θ and ω move at the same time, but 2θ moves at twice the angular velocity of ω. Because of this, there is a loss of precision of the center with respect to 2θ.

4.4 Measurement Conditions

The data presented in this thesis was taken at two different experimental runs, with each being at a different beamline (each beamline is described in Sec. 3.5.1). The first run took place at the NSLS in the summer of 1996, while the second run took place at the APS in the summer of 1998.

Both Q-dependent and T-dependent scans were taken at the NSLS, but only Q-dependent scans were taken at the APS. The rest of this section discusses the parameters of each set of scans, while the actual values for every integrated intensity scan can be found in Appendix F.

4.4.1 Crystal Characteristics

From the observation of the freezing and melting signatures of the crystals, the freezing temperature is known (see Appendix G.7.2). This temperature can be measured twice, when freezing (T_{f}) and when melting (T_{m}), in order to get a good measurement. Using the average of these temperatures and the experimentally obtained thermodynamic relations (see Appendix D.2), the pressure at freezing (P_{eq}) is found, which is then used to determine the molar volume of the crystal at freezing (V_{eq}). Tables 4.1 and 4.2 have these values for the crystals that the Debye-Waller scans were performed upon. The uncertainty in T comes from the fact that the temperature plateau at freezing has a slight slope. Sometimes only one of the signature temperatures was able to be determined. The temperature given is the value measured by sensor B.

Certain hcp crystals were grown when the pressure was above the hcp-fcc-liquid triple point. The initial crystal formed was fcc, and an hcp crystal was formed by further cooling.

4.4.2 Crystal Quality

The quality of the crystals used during the runs varied widely from almost perfect to very mosaic. The quality can be judged qualitatively from the use of pictures and rocking curves. These data are given in Tables 4.3 and 4.4.

Looking at the Polaroid pictures of each crystal and knowing the crystal structure, the number of visible crystals can be estimated; this method is not fool-proof, since only a limited scan in ω was possible when taking the pictures. The main indicator is the reflection with the lowest Q value, which is normally the strongest. For an fcc crystal, a 4-fold symmetry of the 111 reflections is expected, while for an hcp crystal, 6-fold symmetry of the 100 reflections is expected. Knowing the symmetry of these reflections, and using the beryllium powder rings as guides, it is possible to infer the number of crystals.

The extent of the mosaic quality of the crystal can be inferred from the rocking curves. If there is one narrow peak, this crystal is most likely ideal. If the reflection has two peaks, but the

Table 4.1: NSLS 1996 Crystal Characteristics

Crystal Label	Helium Isotope	Crystal Structure	T_f [K] ($\pm$ 0.02)	T_m [K] ($\pm$ 0.02)	P_{eq} [MPa] ($\pm$ 0.3)	V_{eq} [cm^3] ($\pm$ 0.006)
1	3	hcp[a]	18.55		167.9	11.587
3	3	hcp[a]		18.56	168.0	11.585
4	3	fcc	18.56	18.56	168.0	11.585
12	3	hcp	16.92	16.96	146.6	11.908
13	3	hcp	14.95	14.93	121.6	12.363
15	3	hcp	13.24		101.6	12.812
16	4	fcc	20.68	20.73	187.5	10.973
18	4	hcp	14.78	14.82	110.5	12.135

[a] The crystal went through an fcc phase before changing to hcp.

Table 4.2: APS 1998 Crystal Characteristics

Crystal Label	Helium Isotope	Crystal Structure	T_f [K] ($\pm$ 0.02)	T_m [K] ($\pm$ 0.02)	P_{eq} [MPa] ($\pm$ 0.3)	V_{eq} [cm^3] ($\pm$ 0.006)
5	3	hcp		13.81	108.2	12.654
12	3	hcp[a]	17.90	17.84	158.7	11.718

[a] The crystal went through an fcc phase before changing to hcp.

tails slope gently down to zero as with a ideal crystal, the crystal is composed of two sub-crystals slightly out of orientation. If the peak has an irregular shape, or if there are bumps in the tails, this shows that the crystal is mosaic; the degree of the mosaic depends on how misshapen the peak is. Figs. 4.1 – 4.10 are plots of the rocking curves of two peaks (a high Q and a low Q one) for each crystal; the plots have some of the tails cut off.

Table 4.3: NSLS 1996 Crystal Quality Characteristics

Crystal Label	Number of Crystals Using Image on Polaroid	Reflection Structure
1	1 strong	single peak with weak secondary peak
3	1 strong	single peak
4	1 strong and 2 weak	single peak
12	1 strong and 1 weak	asymmetric mosaic peak
13	2 strong and 1 weak	mosaic reflection with 3 strong peaks
15	1 strong and 2 weak	wide mosaic reflection with over 10 peaks
16	1 strong and 2 weak	asymmetric mosaic peak
18	2 strong	asymmetric mosaic peak

Table 4.4: APS 1998 Crystal Quality Characteristics

Crystal Label	Number of Crystals Using Image on Polaroid	Reflection Structure
5	3 strong, clustered	mosaic reflection with 5 peaks
12	1 strong	mosaic reflection with 1–3 peaks

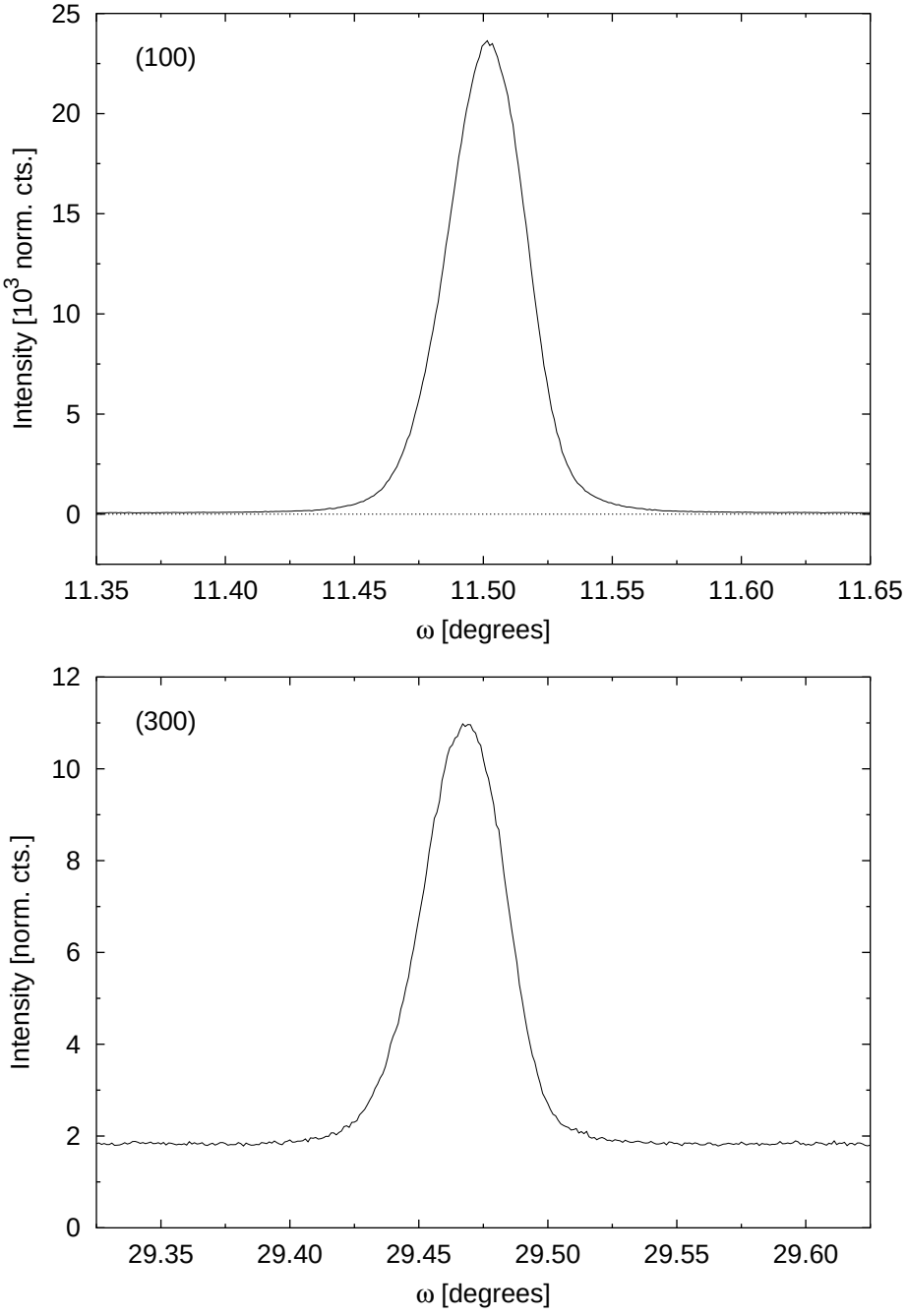

Figure 4.1: Rocking curves of (1 0 0) and (3 0 0) peaks for NSLS crystal 1.

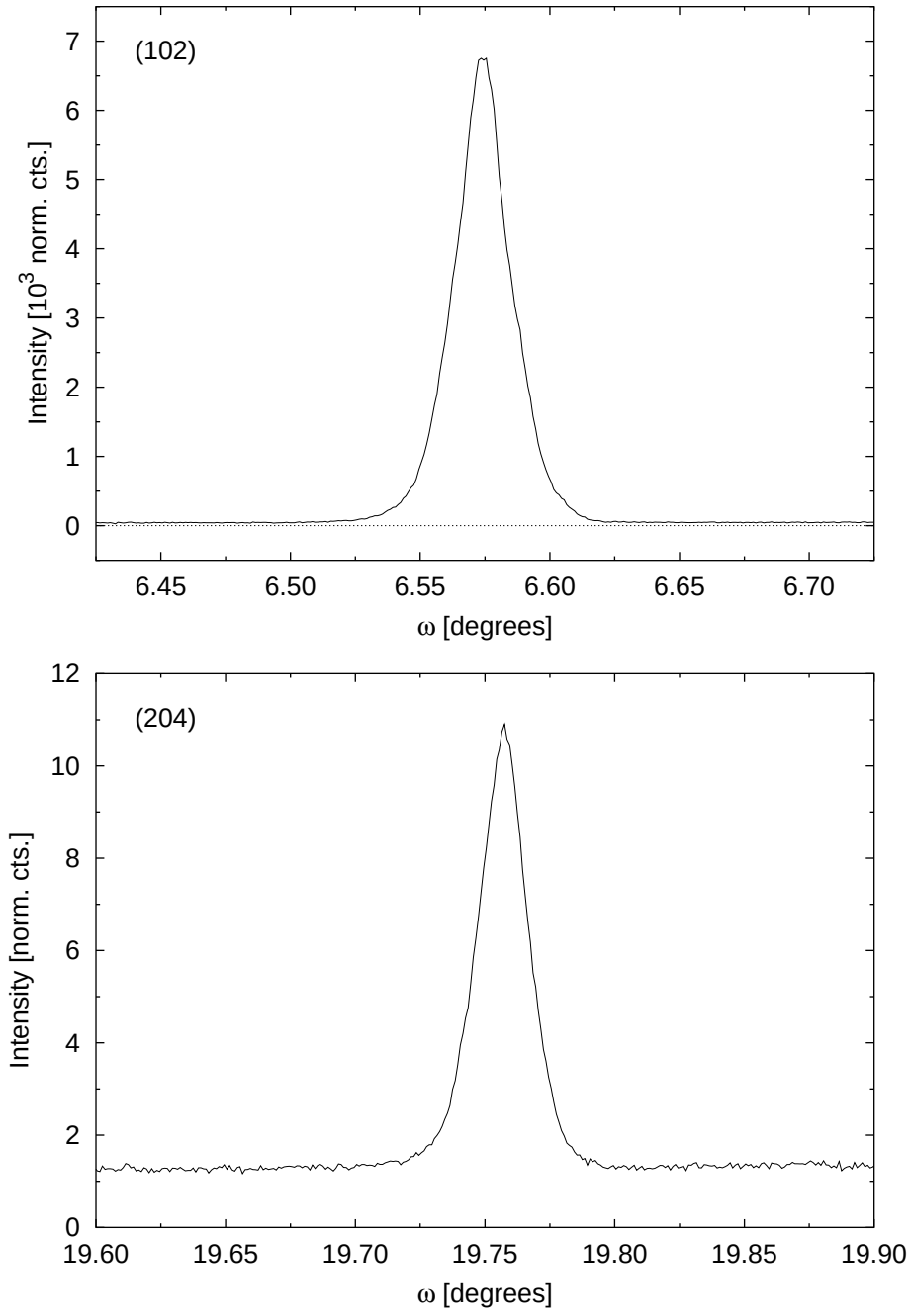

Figure 4.2: Rocking curves of (1 0 2) and (2 0 4) peaks for NSLS crystal 3.

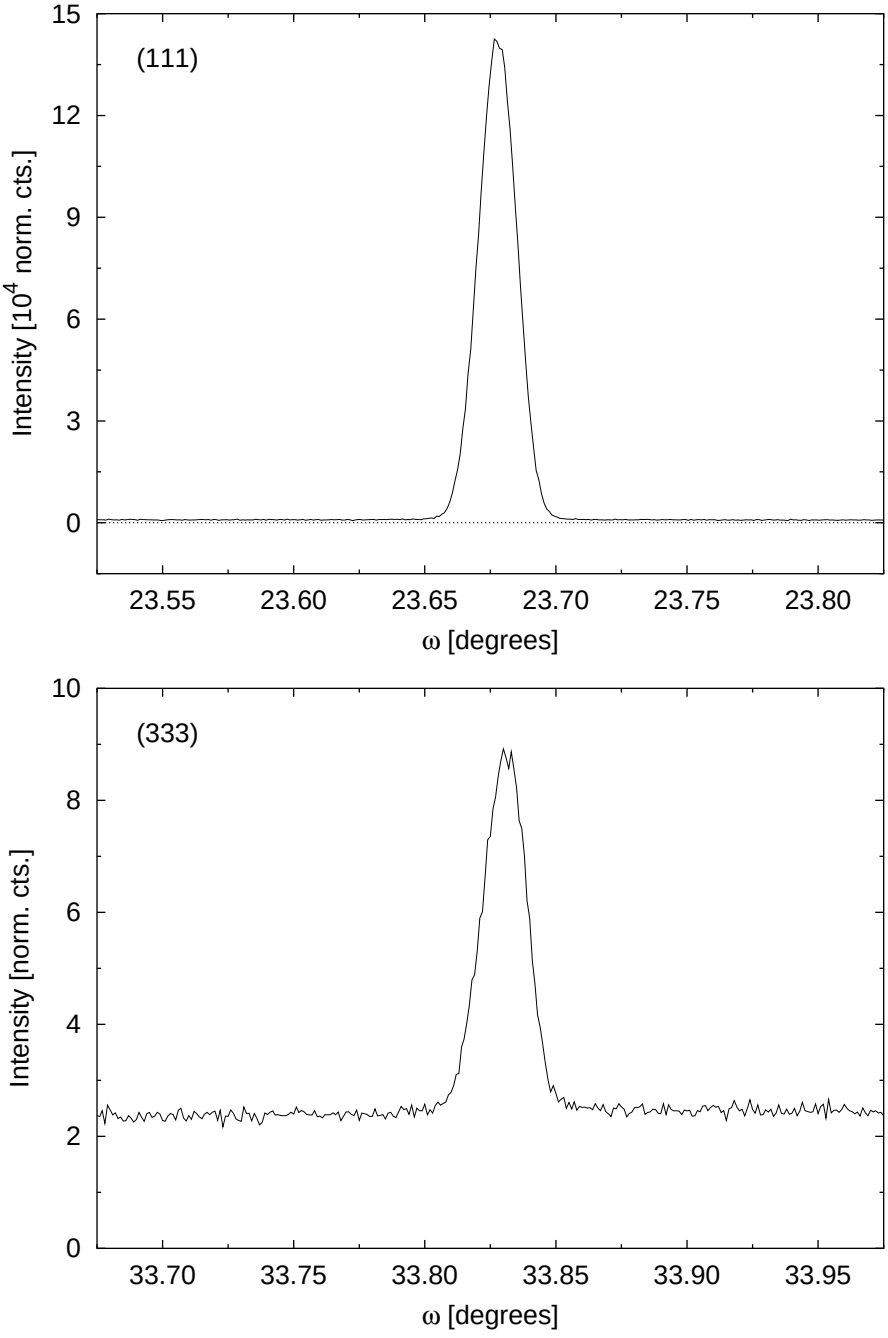

Figure 4.3: Rocking curves of (1 1 1) and (3 3 3) peaks for NSLS crystal 4.

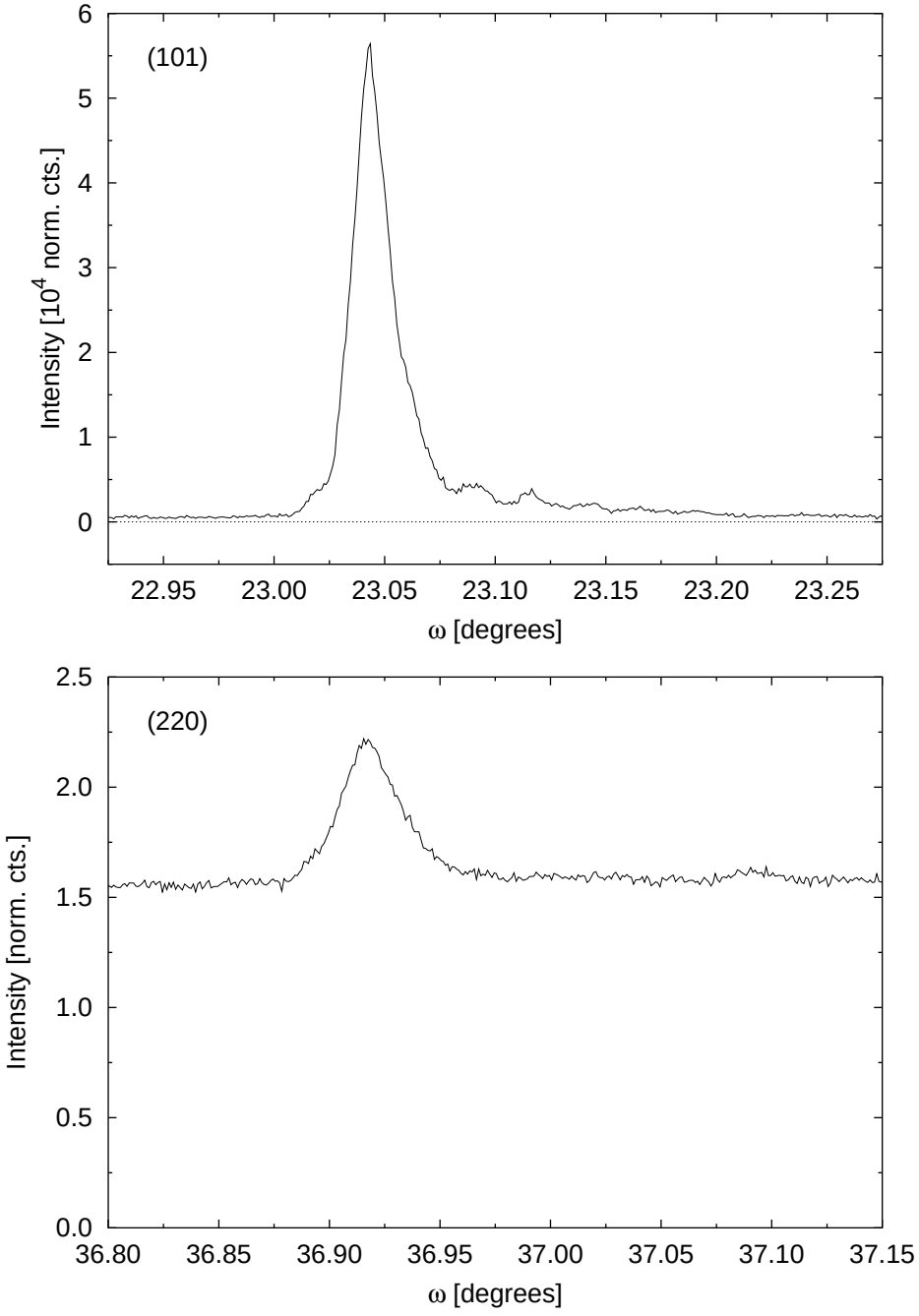

Figure 4.4: Rocking curves of (1 0 1) and (2 2 0) peaks for NSLS crystal 12.

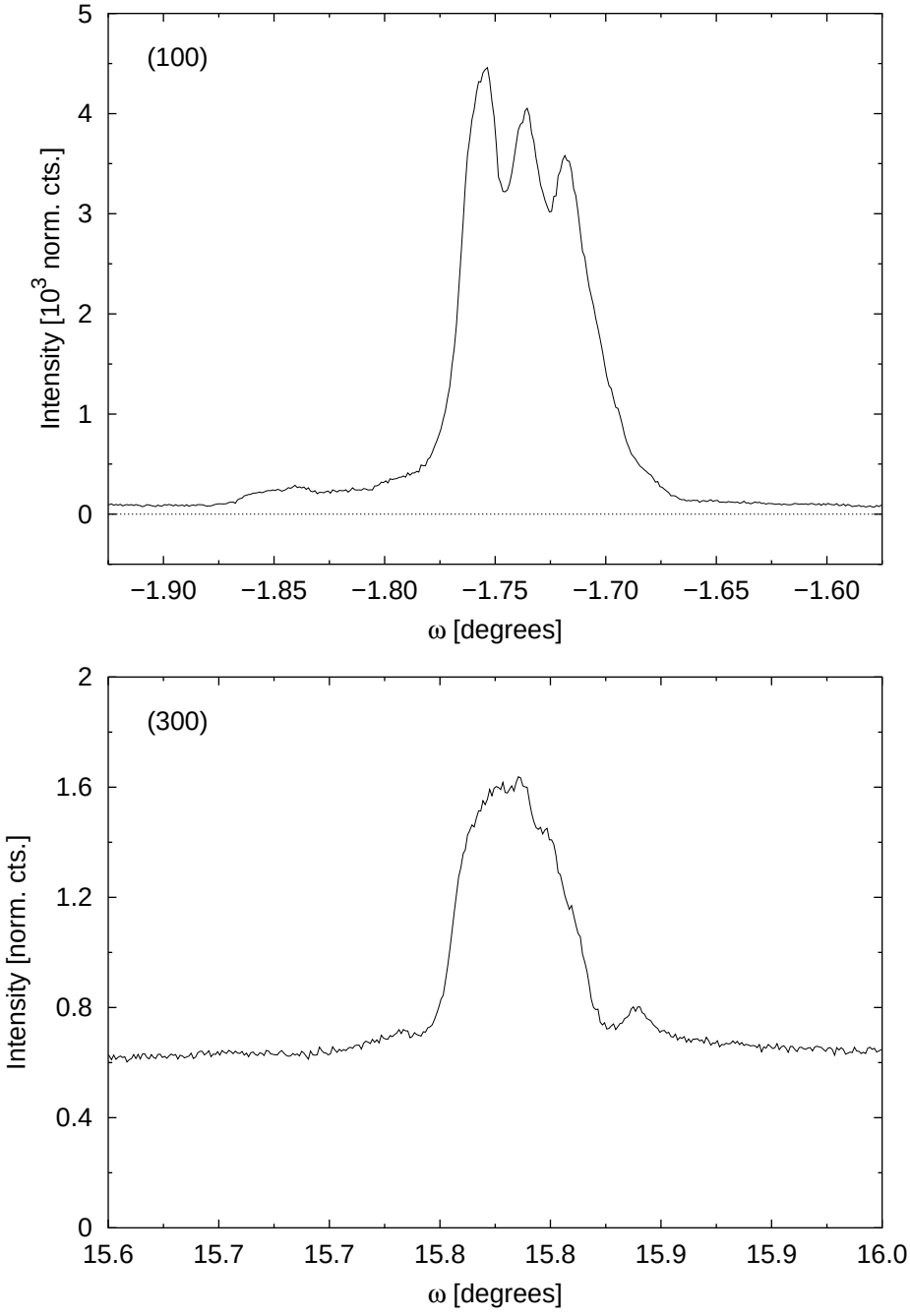

Figure 4.5: Rocking curves of (1 0 0) and (3 0 0) peaks for NSLS crystal 13.

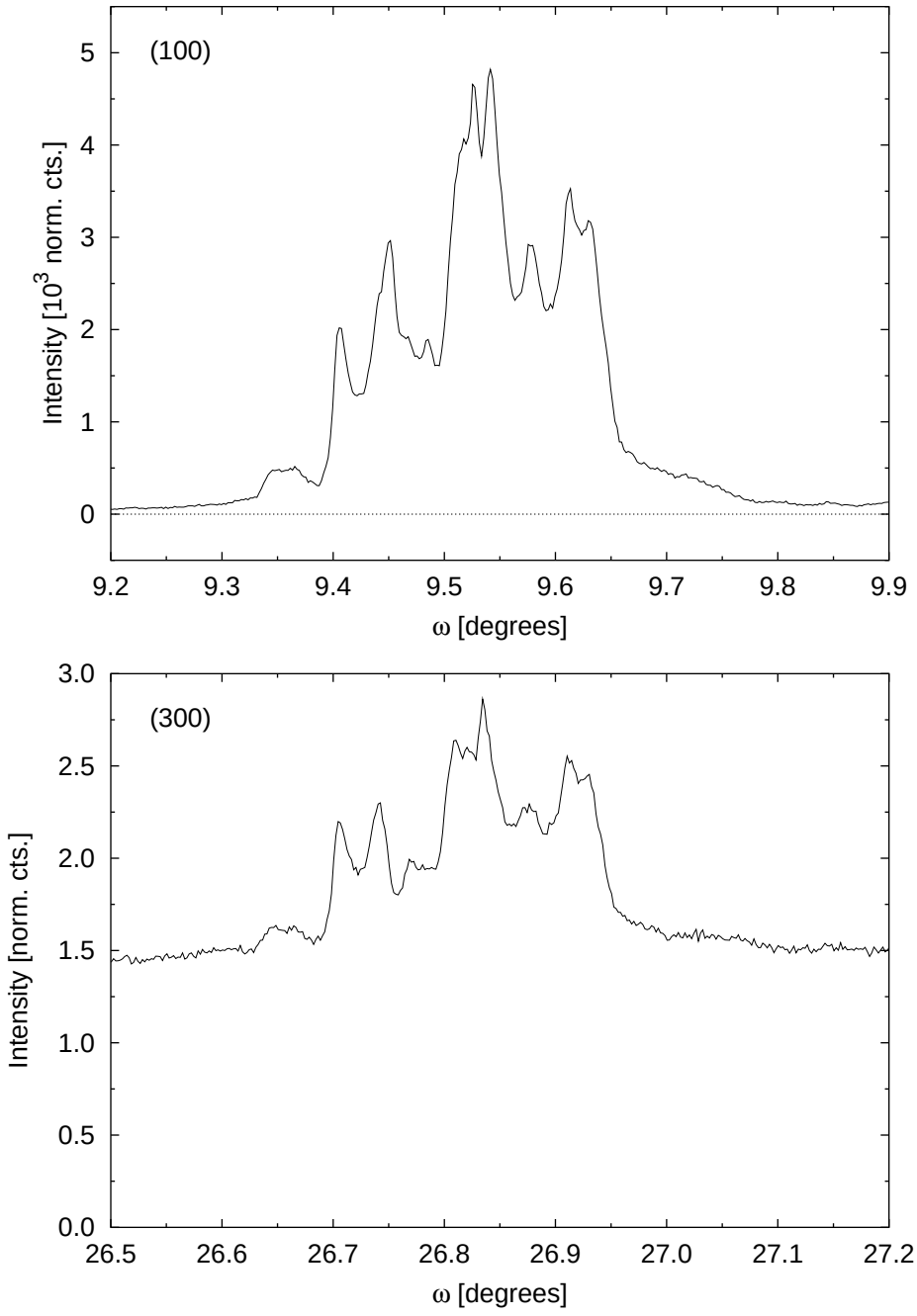

Figure 4.6: Rocking curves of (1 0 0) and (3 0 0) peaks for NSLS crystal 15.

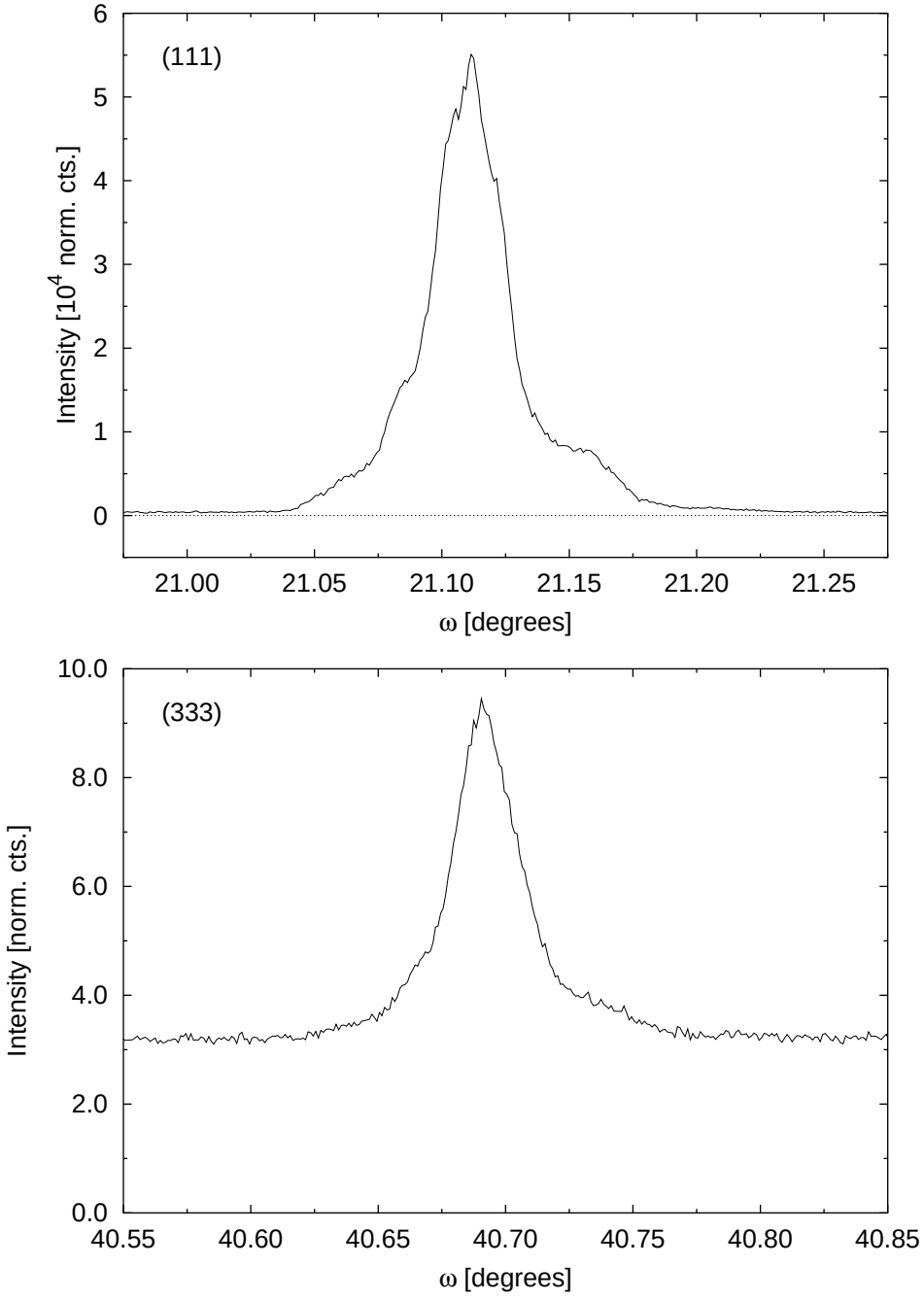

Figure 4.7: Rocking curves of (1 1 1) and (3 3 3) peaks for NSLS crystal 16.

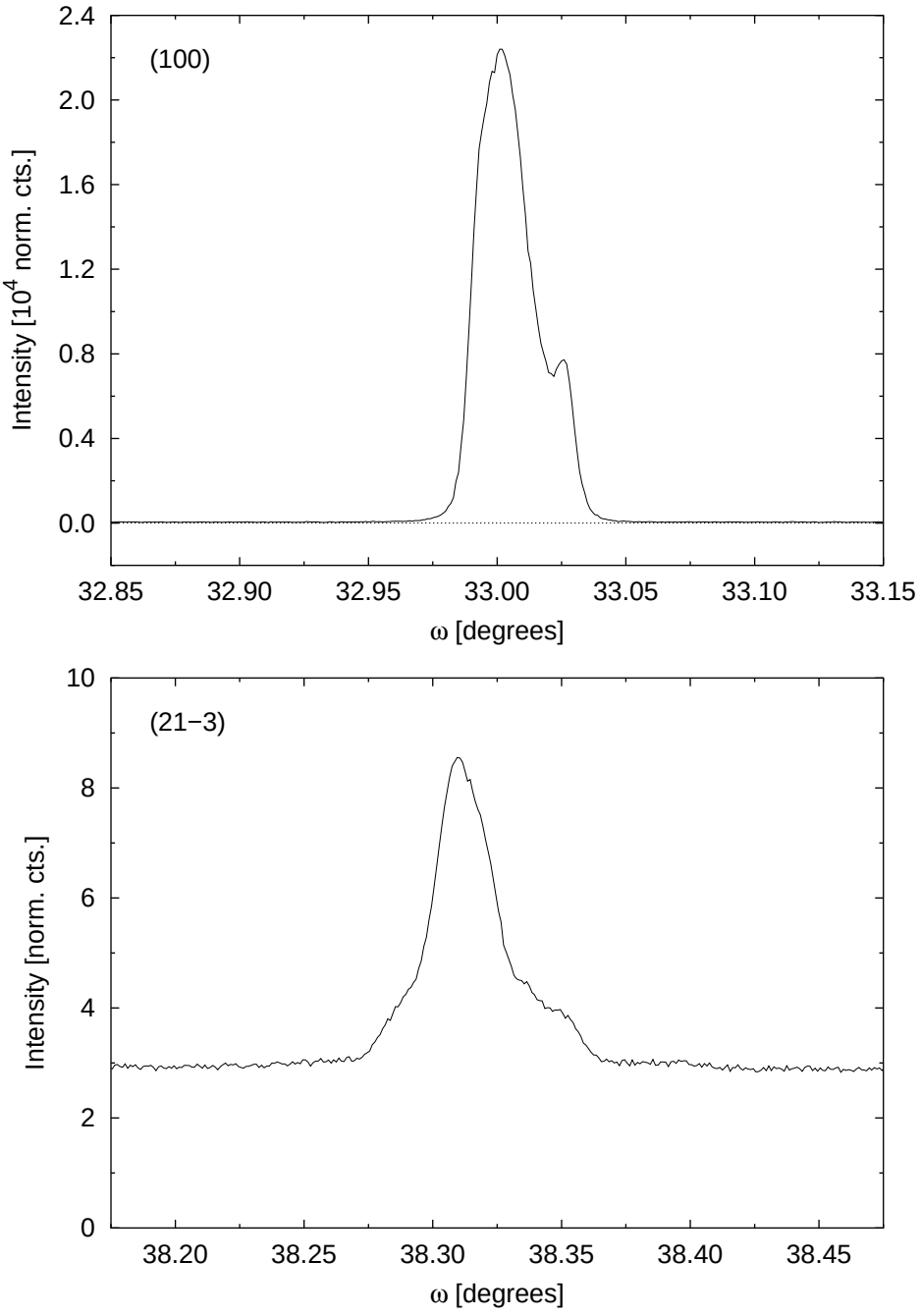

Figure 4.8: Rocking curves of $(1\,0\,0)$ and $(2\,1\,\bar{3})$ peaks for NSLS crystal 18.

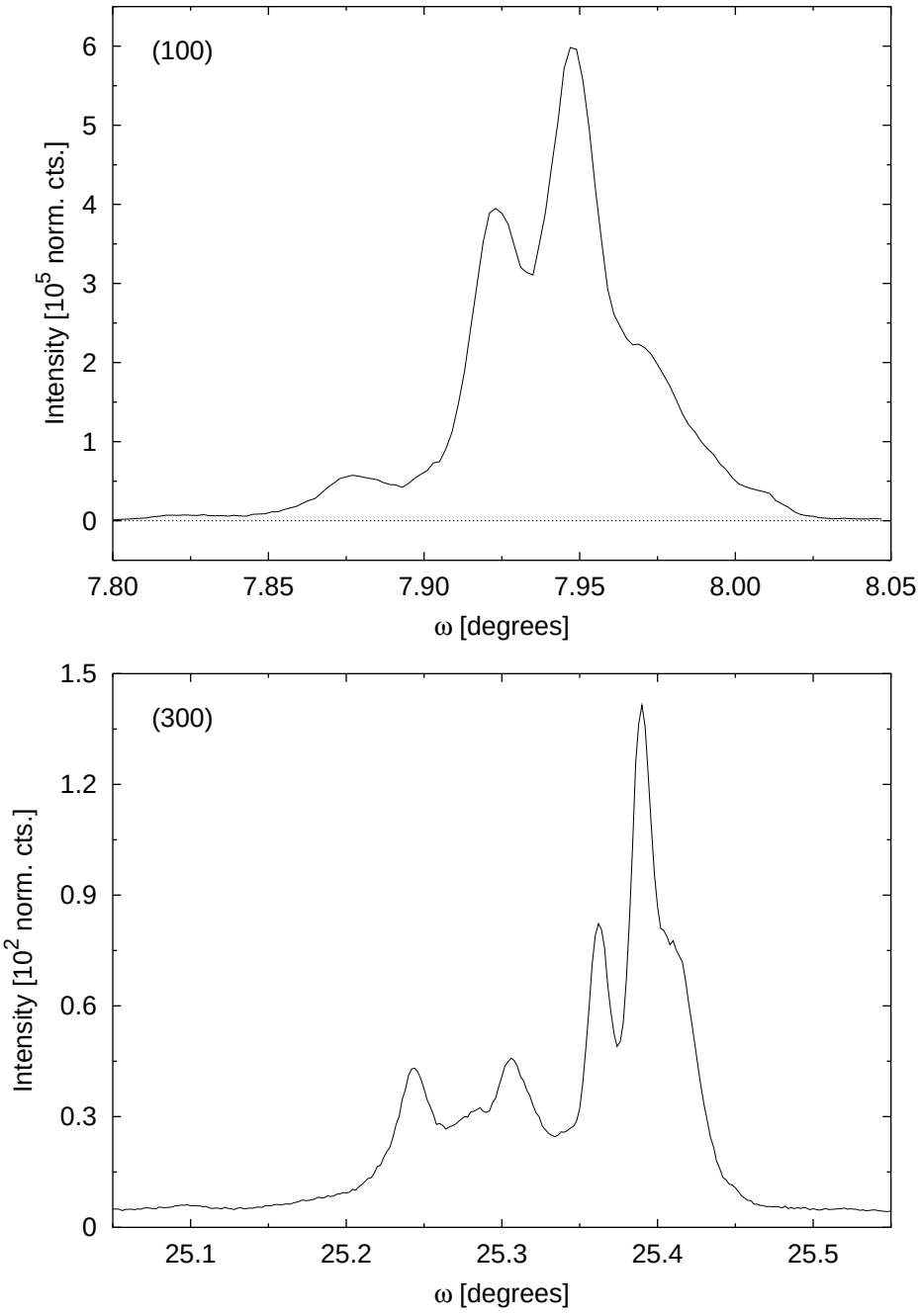

Figure 4.9: Rocking curves of (1 0 0) and (3 0 0) peaks for APS crystal 5.

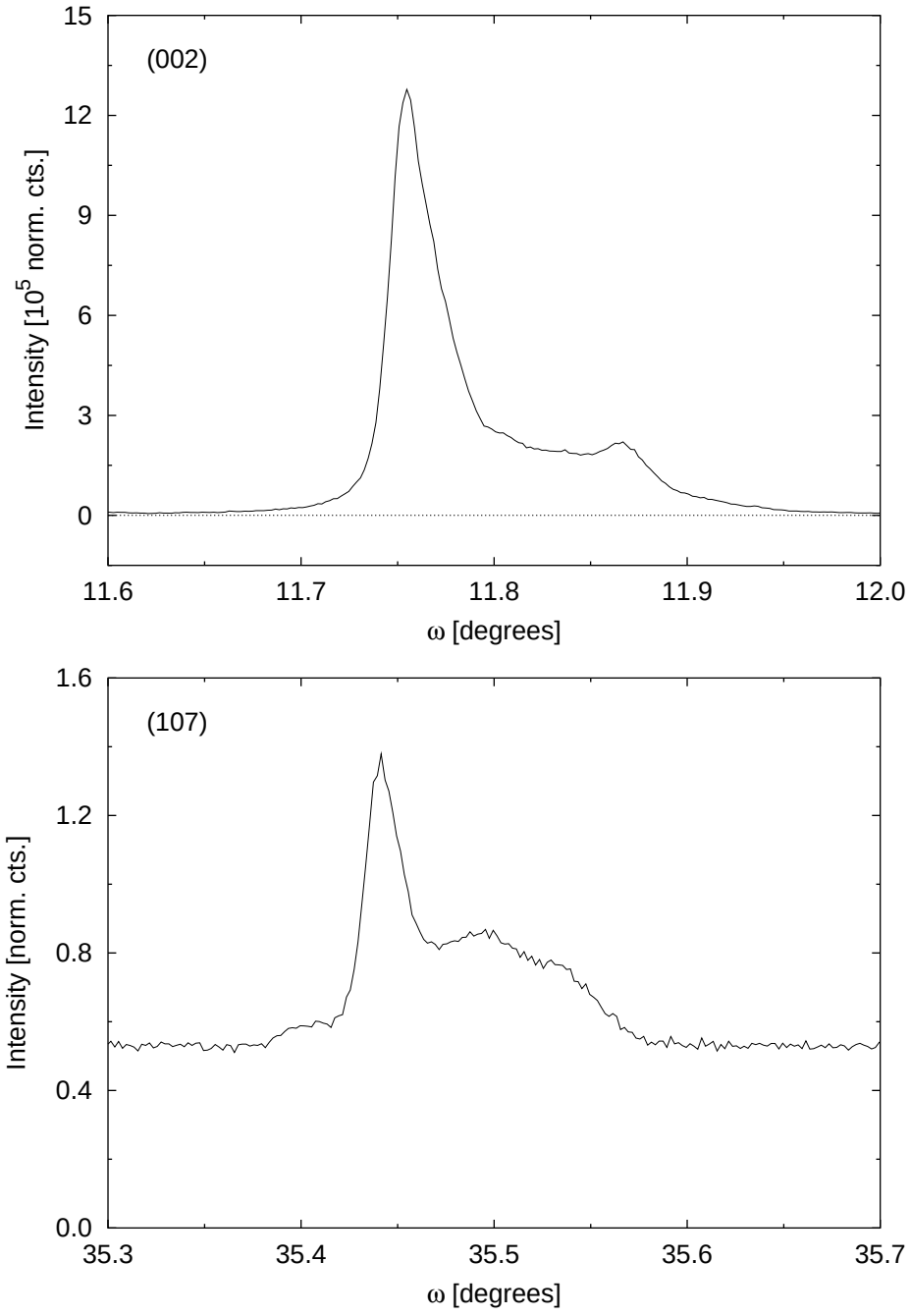

Figure 4.10: Rocking curves of (0 0 2) and (1 0 7) peaks for APS crystal 12.

4.4.3 Lattice Parameters and Volumes

Determination of the lattice parameters was done differently for both beamtimes. Once the lattice parameters were determined, the molar volume is determined using the formulae in Appendix B.2.

Corrections to the 2θ angles were needed for several measurements, since the lattice parameters increased or decreased with reflection angle. The corrections are: 0.015 was subtracted for NSLS crystal 4, 0.02 was subtracted for NSLS crystal 13, 0.025 was added for NSLS crystal 16, and 0.11 was added for APS crystals 5 and 12.

Since the reflections for the NSLS beamtime were heavier with h and k indices, the value of a was solved using high 2θ, pure a reflections. After this, reflections with the highest ℓ values were used with the value of a to find the c value.

For the APS reflections, reflections were heaviest in ℓ, so c was solved for using high 2θ, pure c reflections. After this, reflections with high values in h and k with respect to ℓ were used to find the value of a.

The measured lattice parameter data can be found in Tables 4.5 and 4.6.

4.4.4 Scan Parameters

The molar volume values cited below are from the determination of the lattice parameters, which were used in the equations given in Appendix D.2. The temperature given is the value measured by sensor B. The scan width corresponds to the width of the rocking curve in ω, and the step size is the distance between each meaurement.

The labelling of the measurements is based on the number of the crystal as pertaining to the order grown. If a letter is given, it is used to differentiate between measurements on the same crystal.

NSLS 1996 Q-Dependent Debye-Waller Scans

The measurement conditions for the NSLS 1996 Q-dependent data can be found in Table 4.7.

For crystals 1, 3, and 4, the amount of helium in the system is the same. Any change in lattice parameters between measurements 1A, 1B, and 3 — the hcp crystals — comes from vacancies in the crystal.

Crystal 4 has two sets of measurements with identical conditions. The data is not placed

Table 4.5: NSLS 1996 Q-dependent Lattice Parameter Data

Measure-ment	a [Å] ±0.0003	c [Å] ±0.0004	c/a ±0.0005	V [cm^3] ±0.003
1A	3.0074	4.9051[a]	[b]	11.568[a]
1B	3.0072	4.9047[a]	[b]	11.566[a]
3	3.0101	4.9103	1.6313	11.602
4	4.2526			11.578
12	3.0359	4.9506	1.6307	11.898
13	3.0757	5.0124	1.6297	12.365
15	3.1119	5.0755[a]	[b]	12.817[a]
16	4.1743			10.951
18A	3.0543	4.9825	1.6313	12.120
18B	3.0545	4.9856	1.6323	12.129

[a] Value derived from average c/a of 1.6310.

[b] Not enough experimental data to generate a reliable c/a value.

Table 4.6: APS 1998 Q-dependent Lattice Parameter Data

Measure-ment	a [Å] ±0.0005	c [Å] ±0.0004	c/a ±0.0005	V [cm^3] ±0.004
5	3.0882	5.0369[a]	[b]	12.526[a]
12	3.0109	4.9102	1.6308	11.607

[a] Value derived from average c/a of 1.6310.

[b] Not enough experimental data to generate a reliable c/a value.

---

together because the sets are separated in time by a ring refill. If analyzed together, each pair of intensities for corresponding reflections have a similar ratio.

Measurement 16 has duplicate scans for one reflection, and triplicate scans for another.

NSLS 1996 *T*-Dependent Debye-Waller Scans

The measurement conditions for the NSLS 1996 T-dependent data can be found in Table 4.8.

Measurement 3 was taken in several sets, with long periods of time and also beam dumps between sets. This caused the relationship between the data in these sets to become uncertain, so data points at the same temperature in different sets tied the intervals together by normalizing one

set to match the tie point in the other set. It was not possible to check the reproducibility of the measurements, due to these problems.

APS 1998 Q-Dependent Debye-Waller Scans

The measurement conditions for the APS 1998 Q-dependent data can be found in Table 4.9.

Measurement 12 has an additional correction to it. Midway through taking the set, the monochromator was tweaked, resulting in the beam position at the sample position moving, changing the resultant intensity of reflections. This is when we first realized this problem with beam position stability. This discontinuity was solved by retaking the last scan done which was for the (2 1 3) peak, and when the data were analyzed, all the values after (2 1 3) in time were adjusted down to correspond to the change in its intensity.

4.5 Data Analysis

Discussion of the data in this section assumes that the data have already been processed, as described in Sec. 4.1. Thus, the data will have the atomic form factor, structure factor, and Lorentz factor already removed.

4.5.1 Q-Dependent Data

Q-dependent Debye-Waller data are collected at one temperature, where rocking curves of as many reflections as possible are taken. Each set of data produces a $\langle u^2 \rangle$ value.

Basic analysis of this type of data is very straightforward, as long as a simple theoretical model is assumed, as described in Sec. 2.1.4. The basic expression of the Debye-Waller factor is

$$I \propto I_0 e^{-Q^2 \langle {u_Q}^2 \rangle} , \tag{4.20}$$

where the exponential contains the factor. From this, it is easy to see the relation between different reflections of the same crystal; the higher the value of Q, the smaller the integrated intensity of the peak. If the natural logarithm of both sides is taken, as in

$$\ln(I) = -\langle {u_Q}^2 \rangle \, Q^2 + (\text{constant}) , \tag{4.21}$$

Table 4.7: NSLS 1996 Q-dependent Measurement Conditions

Measure-ment	T [K] ($\pm$0.01)	Scan Width [degrees]	Step Size [degrees]	Detector Slits V[mm]×H[mm]
1A	17.37	0.4	0.001	5×5
1B	15.86	0.4	0.001	5×5
3	11.52	0.4	0.001	5×5
4A	18.13	0.4	0.001	5×5
4B	18.13	0.4	0.001	5×5
12	16.81	0.4	0.001	2×5
13	14.23	0.4	0.001	2×5
15	12.54	0.8	0.002	2×5
16	20.25	0.4	0.001	2×5
18A	14.23	0.4	0.001	2×5
18B	12.00	0.4	0.001	2×5

Table 4.8: NSLS 1996 T-dependent Measurement Conditions

Measure-ment	Measured Reflection	Scan Width [degrees]	Step Size [degrees]	Detector Slits V[mm]×H[mm]
3	$(3\,0\,0)$	0.2	0.001	5×5
18	$(2\,1\,\bar{3})$	0.2	0.001	2×5

Table 4.9: APS 1998 Q-dependent Measurement Conditions

Measure-ment	T [K] ($\pm$0.01)	Scan Width [degrees]	Step Size [degrees]	Detector Slits V[mm]×H[mm]
5	13.30	0.25–0.6	0.002	2×4
12	16.90	0.4–0.7	0.002	1.5×2.5

the equation is linear in terms of Q^2.

If an isotropic crystal is assumed, the directional dependence in $\langle {u_Q}^2 \rangle$ is dropped, as discussed in Sec. 2.2.3. This is fine for fcc crystals, but care has to be taken when this assumption is made with hcp crystals. Helium hcp crystals grown during the measurements had a nearly ideal c/a ratio of $\sqrt{8/3}$, and if this ratio is compared to a plot of $\langle {u_c}^2 \rangle / \langle {u_a}^2 \rangle$ versus c/a for other elemental hcp crystals as in Appendix E, $\langle {u_c}^2 \rangle / \langle {u_a}^2 \rangle$ for hcp helium should be around 1.2. However, if this is the case, the data points should separate in terms of $\ln(I)$ as Q^2 increases, since pure a reflections and pure c reflections will create separate lines with different slopes, and all mixed reflections will fall in between these lines.

For this thesis, it will be assumed that hcp helium is isotropic. For the measurements presented here, this broadening cannot be discerned within the experimental uncertainties. Also, the values for the other hcp elemental crystals are all for metals, not a noble gas, so the trend set by these elements might not apply. Helium surely has some anisotropic nature to it, but it was not detected.

So, in order to extract the $\langle u^2 \rangle$ value for a measurement at a given temperature, the data needs to be plotted logarithmically against Q^2. The negative of the slope from a linear fit is the $\langle u^2 \rangle$ value. The resulting error of the slope comes from the fit itself, assuming a good fit [7].

The Lindemann ratio,

$$\text{L.R.} = \frac{\sqrt{\langle {u_{3\text{D}}}^2 \rangle}}{r} = \frac{\sqrt{3\langle u^2 \rangle}}{r} \tag{4.22}$$

where r is the nearest neighbor distance and $\langle {u_{3\text{D}}}^2 \rangle$ is the three dimensional mean squared atomic deviation, can also be calculated. The value of r comes from the measured lattice parameters (see Appendix B.2), while $\langle {u_{3\text{D}}}^2 \rangle = 3\langle u^2 \rangle$ for a Gaussian momentum distribution such as helium's. Since the c/a ratio for hcp is almost ideal, the lattice parameter a is used for r.

The $\langle u^2 \rangle$ and Lindemann ratio values for the measurements as derived from the linear fits are given in a couple of tables. Table 4.10 is the table for ^{3}He, while Table 4.11 is the table for ^{4}He. In addition to these tables, Table 4.12 and Table 4.13 are tables summarizing the measurement conditions for ^{3}He and ^{4}He, respectively.

Plots of the Q-dependent data sets are shown in Figs. 4.11 – 4.20. The lines shown on the plots are from a linear fit to each data set. NSLS crystals 1 and 18 have both sets of data from the different temperatures on the same plot.

Table 4.10: ^{3}He Values Derived From Q-dependent Measurements

Measurement	$\langle u^2 \rangle$ [Å^2]	$\sqrt{3\langle u^2 \rangle}/r$	Θ_M [K]
NSLS 1A	0.1219 ± 0.0066	0.2011	114.2 ± 4.9
NSLS 1B	0.1155 ± 0.0023	0.1957	117.1 ± 1.9
NSLS 3	0.1135 ± 0.0022	0.1938	113.6 ± 1.9
NSLS 4A	0.1143 ± 0.0011	0.1947	121.1 ± 0.9
NSLS 4B	0.1150 ± 0.0015	0.1954	120.5 ± 1.3
NSLS 12	0.1196 ± 0.0026	0.1973	115.0 ± 2.0
NSLS 13	0.1291 ± 0.0041	0.2023	104.8 ± 2.7
NSLS 15	0.1343 ± 0.0027	0.2040	99.3 ± 1.7
APS 5	0.1302 ± 0.0058	0.2023	103.0 ± 3.8
APS 12	0.1158 ± 0.0022	0.1957	118.2 ± 1.8

Table 4.11: ^{4}He Values Derived From Q-dependent Measurements

Measurement	$\langle u^2 \rangle$ [Å^2]	$\sqrt{3\langle u^2 \rangle}/r$	Θ_M [K]
NSLS 16	0.0999 ± 0.0027	0.1855	110.7 ± 2.3
NSLS 18A	0.1125 ± 0.0028	0.1902	93.2 ± 1.9
NSLS 18B	0.1026 ± 0.0017	0.1817	97.5 ± 1.3

Table 4.12: ^{3}He Q-dependent Measurement Conditions Table

Measurement	Structure	T [K]	V [cm^3]
NSLS 1A	hcp	17.37	11.568
NSLS 1B	hcp	15.86	11.566
NSLS 3	hcp	11.52	11.602
NSLS 4	fcc	18.13	11.578
NSLS 12	hcp	16.81	11.898
NSLS 13	hcp	14.23	12.365
NSLS 15	hcp	12.54	12.817
APS 5	hcp	13.30	12.526
APS 12	hcp	16.90	11.607

Table 4.13: ^{4}He Q-dependent Measurement Conditions Table

Measurement	Structure	T [K]	V [cm^3]
NSLS 16	fcc	20.25	10.951
NSLS 18A	hcp	14.23	12.120
NSLS 18B	hcp	12.00	12.129

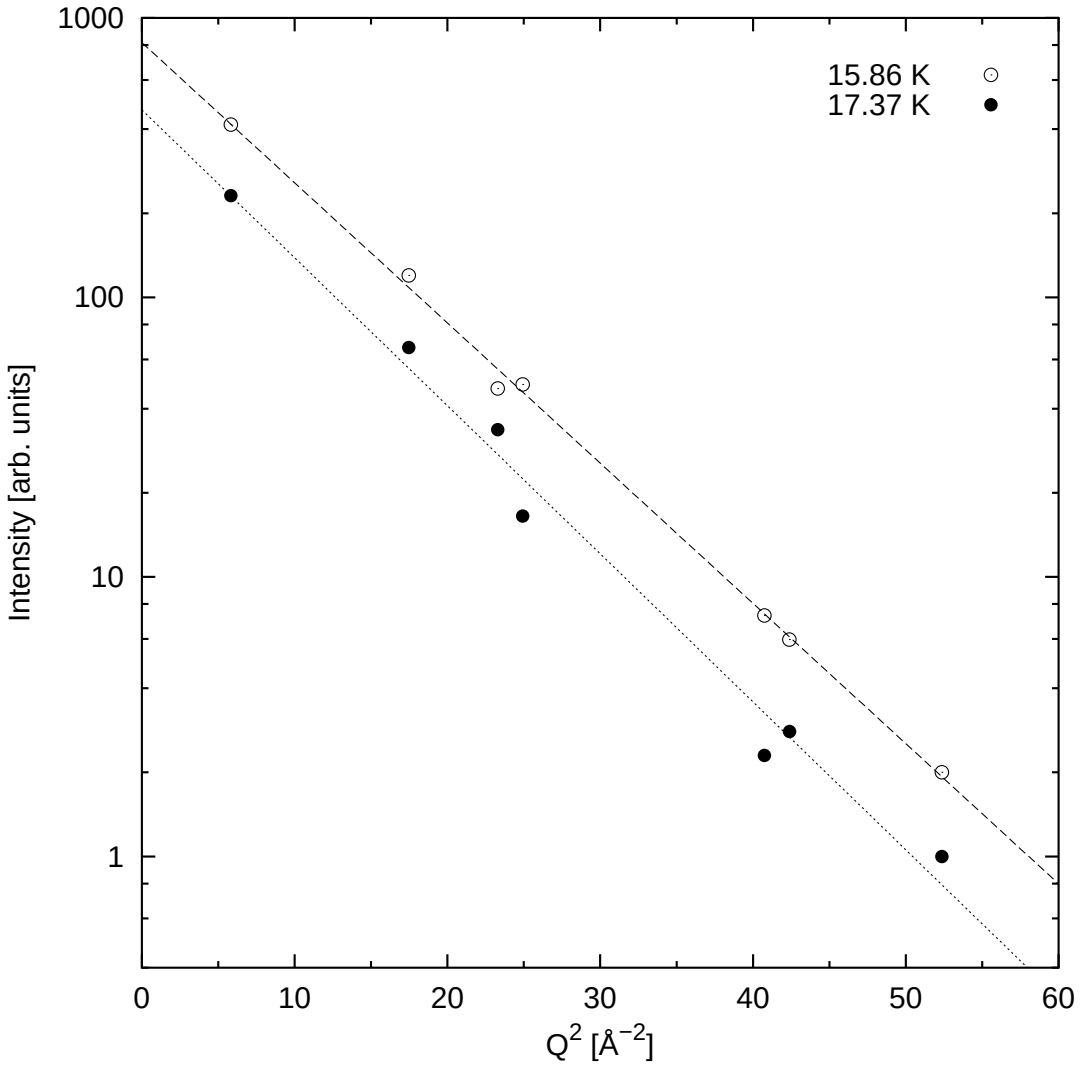

Figure 4.11: NSLS crystal 1 Q-dependent measurements. The crystal is hcp ^{3}He. The conditions for measurement A are a molar volume of 11.568 cm^3 and a temperature of 17.37 K. The conditions for measurement B are a molar volume of 11.566 cm^3 and a temperature of 15.86 K.

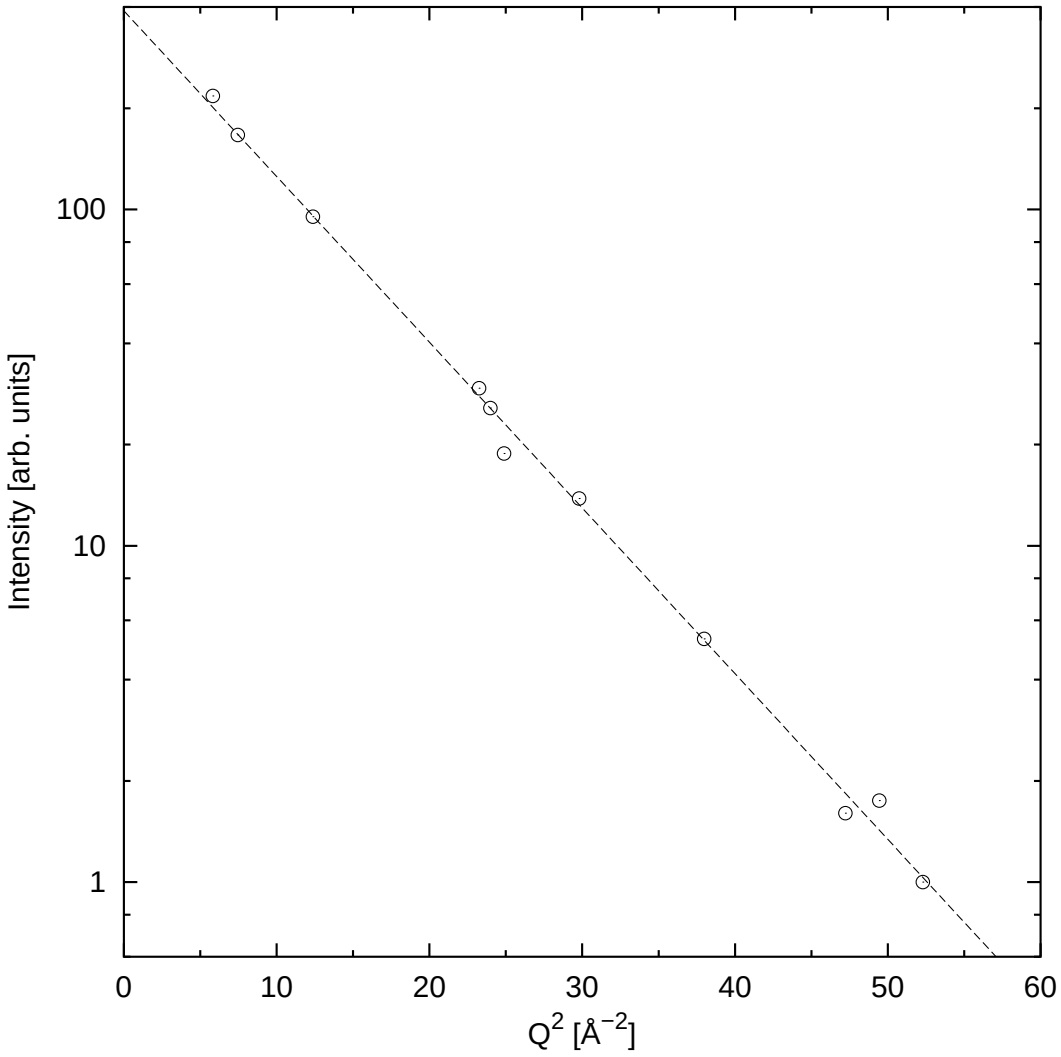

Figure 4.12: NSLS crystal 3 Q-dependent measurement. The crystal is hcp ^{3}He, while the conditions are a molar volume of 11.602 cm^3 and a temperature of 11.52 K.

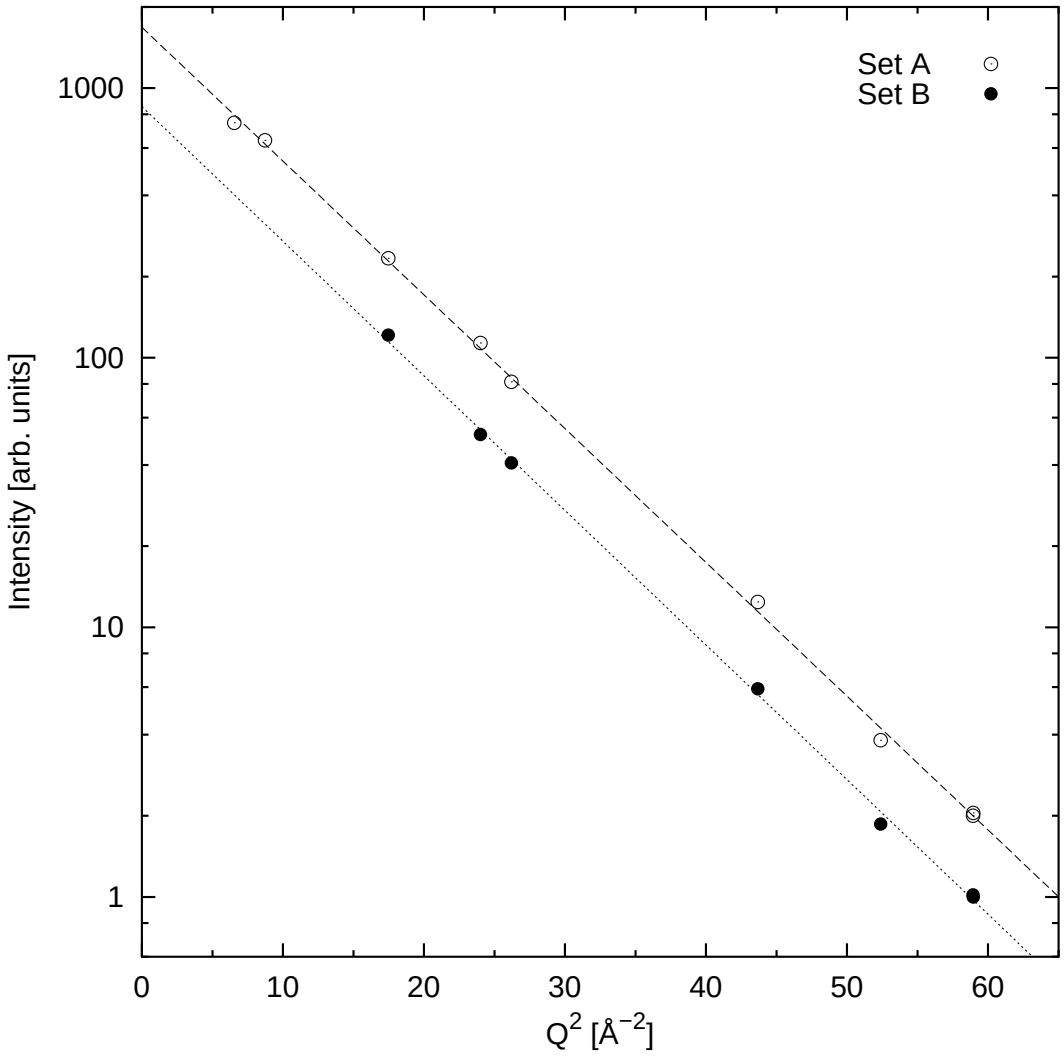

Figure 4.13: NSLS crystal 4 Q-dependent measurements. The crystal is fcc ^{3}He, while the conditions are a molar volume of 11.578 cm^3 and a temperature of 18.13 K.

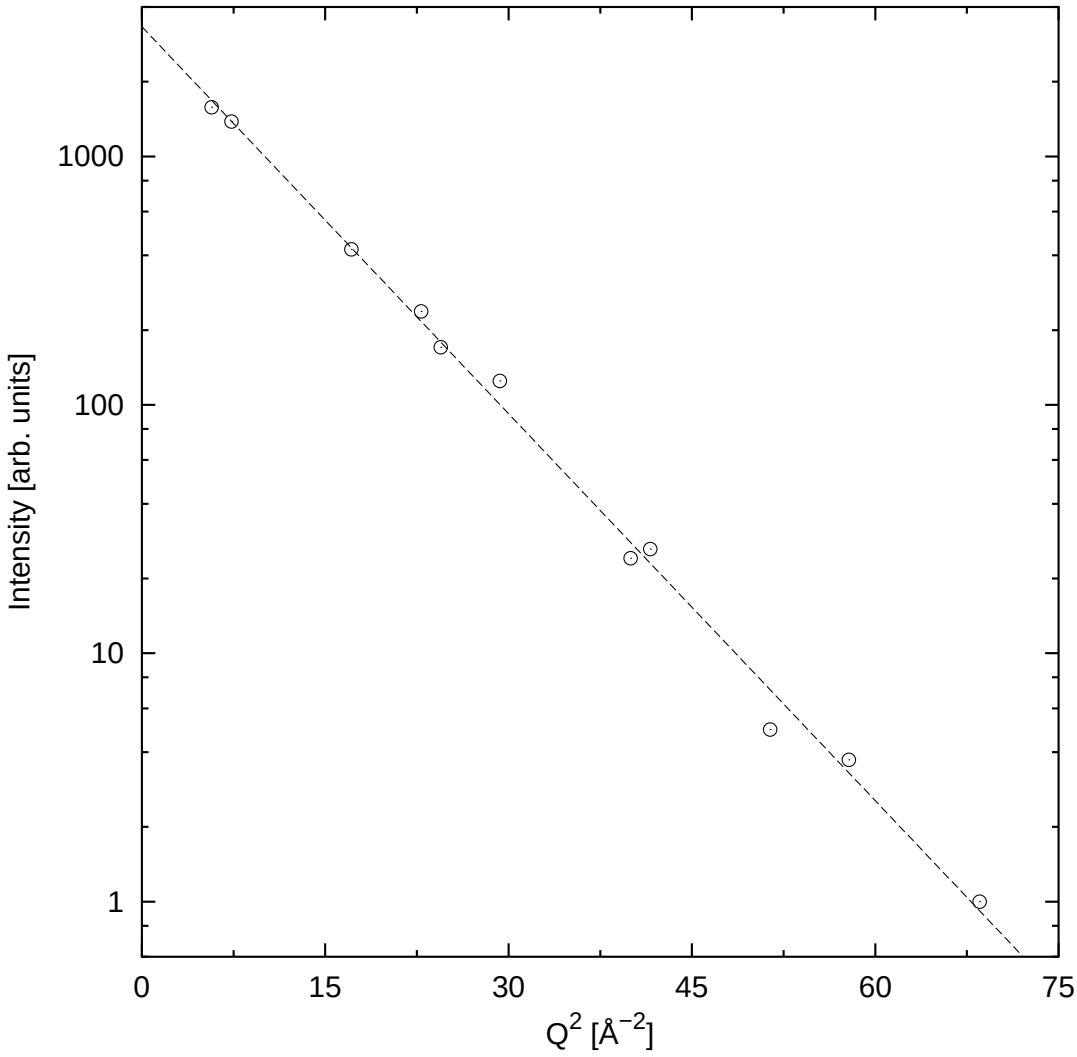

Figure 4.14: NSLS crystal 12 Q-dependent measurement. The crystal is hcp ^{3}He, while the conditions are a molar volume of 11.898 cm^3 and a temperature of 16.81 K.

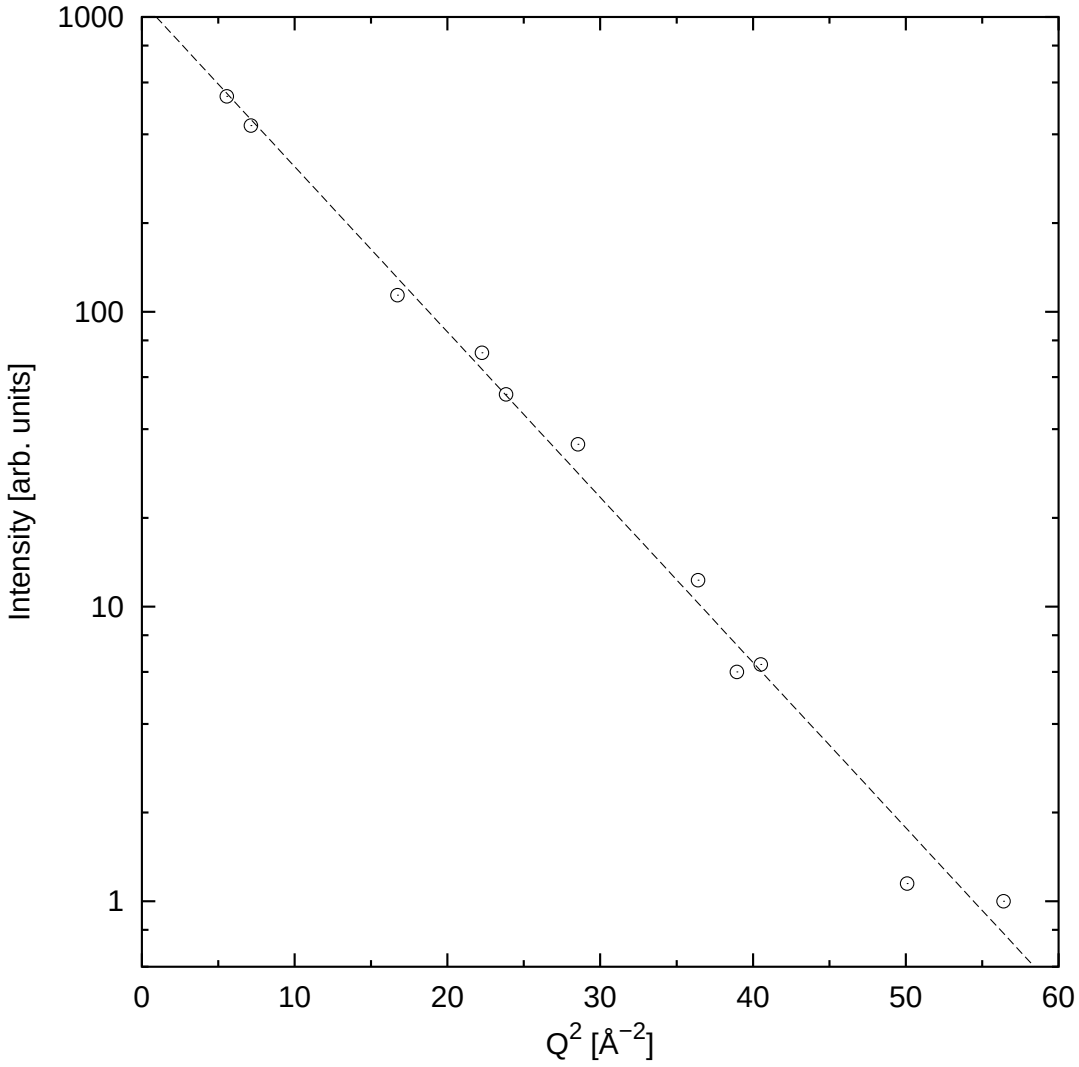

Figure 4.15: NSLS crystal 13 Q-dependent measurement. The crystal is hcp ^{3}He, while the conditions are a molar volume of 12.365 cm^3 and a temperature of 14.23 K.

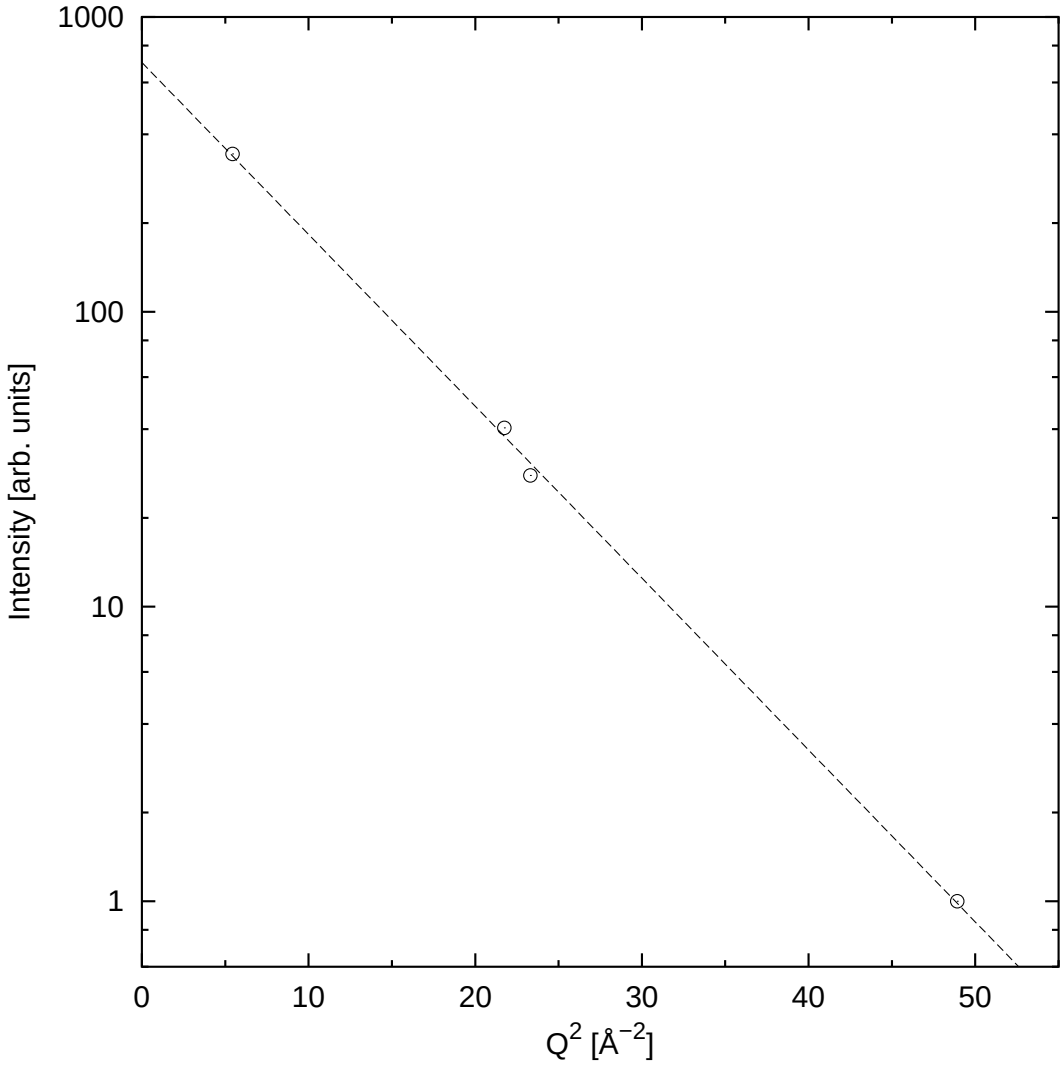

Figure 4.16: NSLS crystal 15 Q-dependent measurement. The crystal is hcp ^{3}He, while the conditions are a molar volume of 12.817 cm^3 and a temperature of 12.54 K.

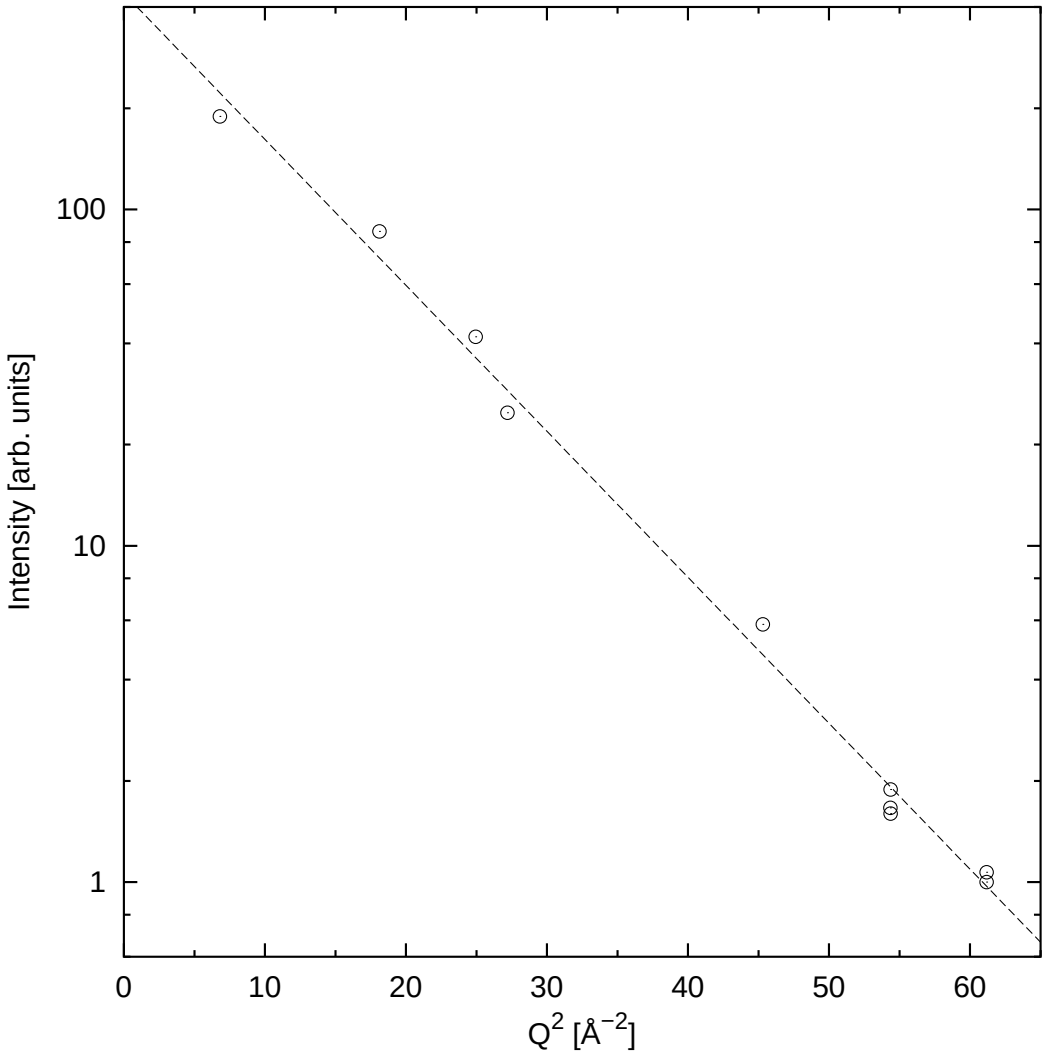

Figure 4.17: NSLS crystal 16 Q-dependent measurement. The crystal is fcc ^{4}He, while the conditions are a molar volume of 10.951 cm^3 and a temperature of 20.25 K.

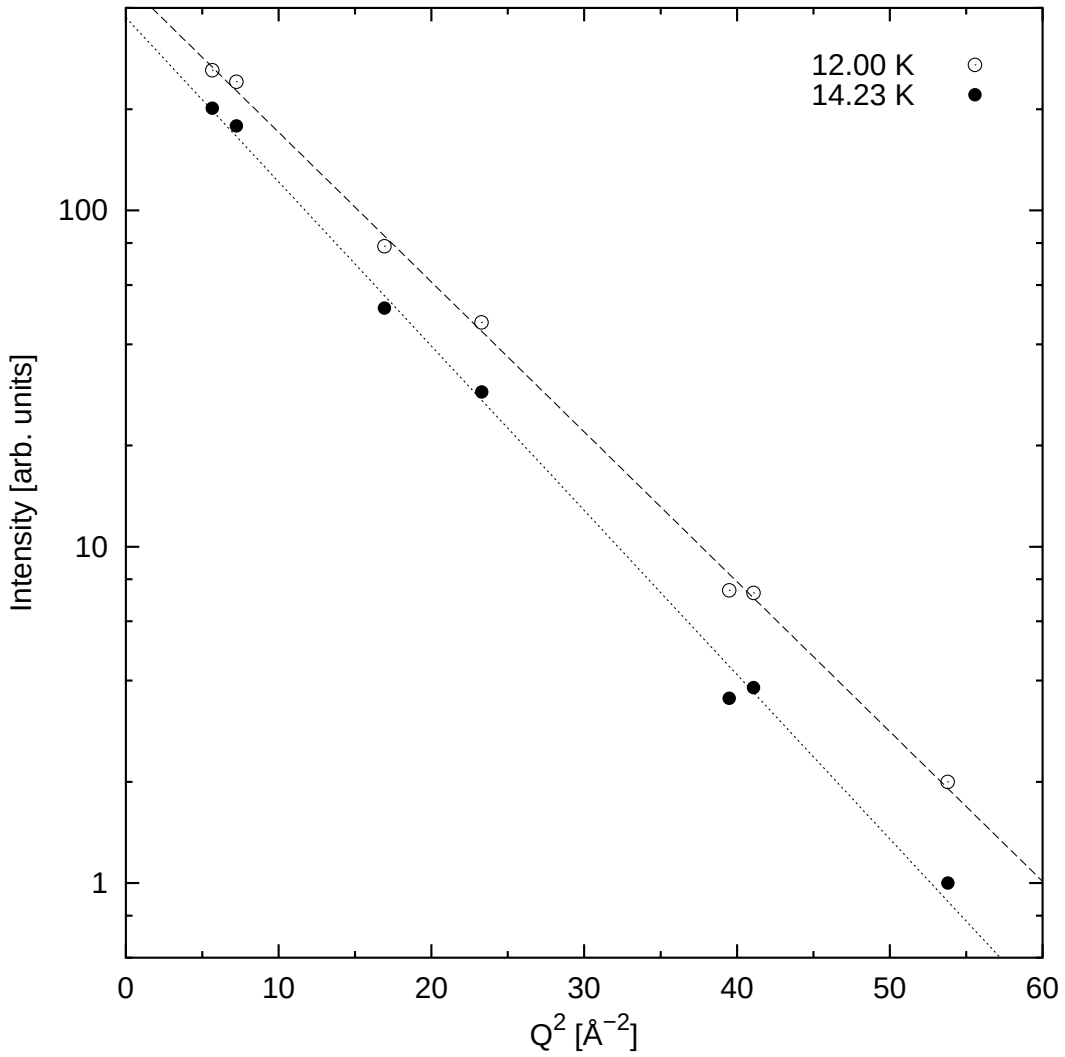

Figure 4.18: NSLS crystal 18 Q-dependent measurements. The crystal is hcp ^{4}He. The conditions for measurement A are a molar volume of 12.120 cm^3 and a temperature of 14.23 K. The conditions for measurement B are a molar volume of 12.129 cm^3 and a temperature of 12.00 K.

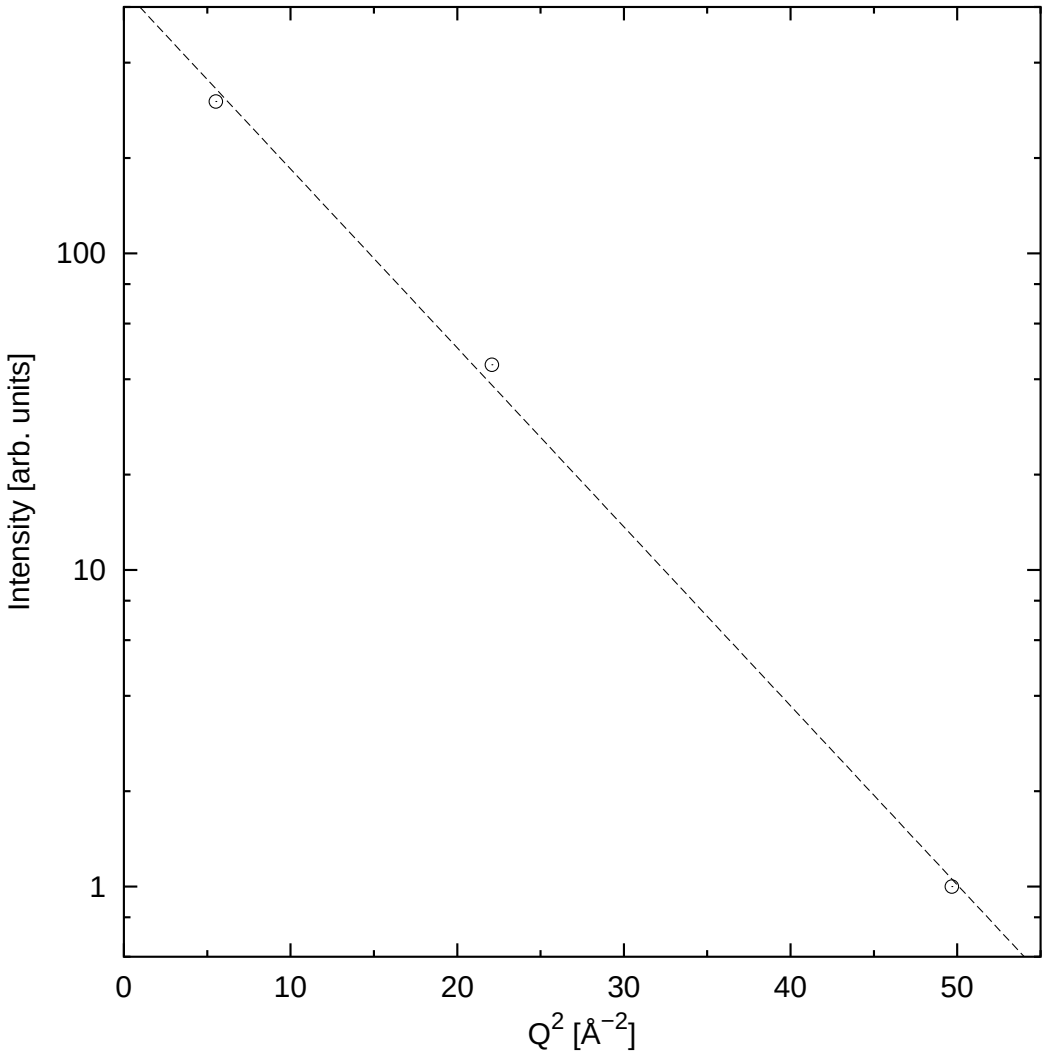

Figure 4.19: APS crystal 5 Q-dependent measurement. The crystal is hcp ^{3}He, while the conditions are a molar volume of 12.526 cm^3 and a temperature of 13.30 K.

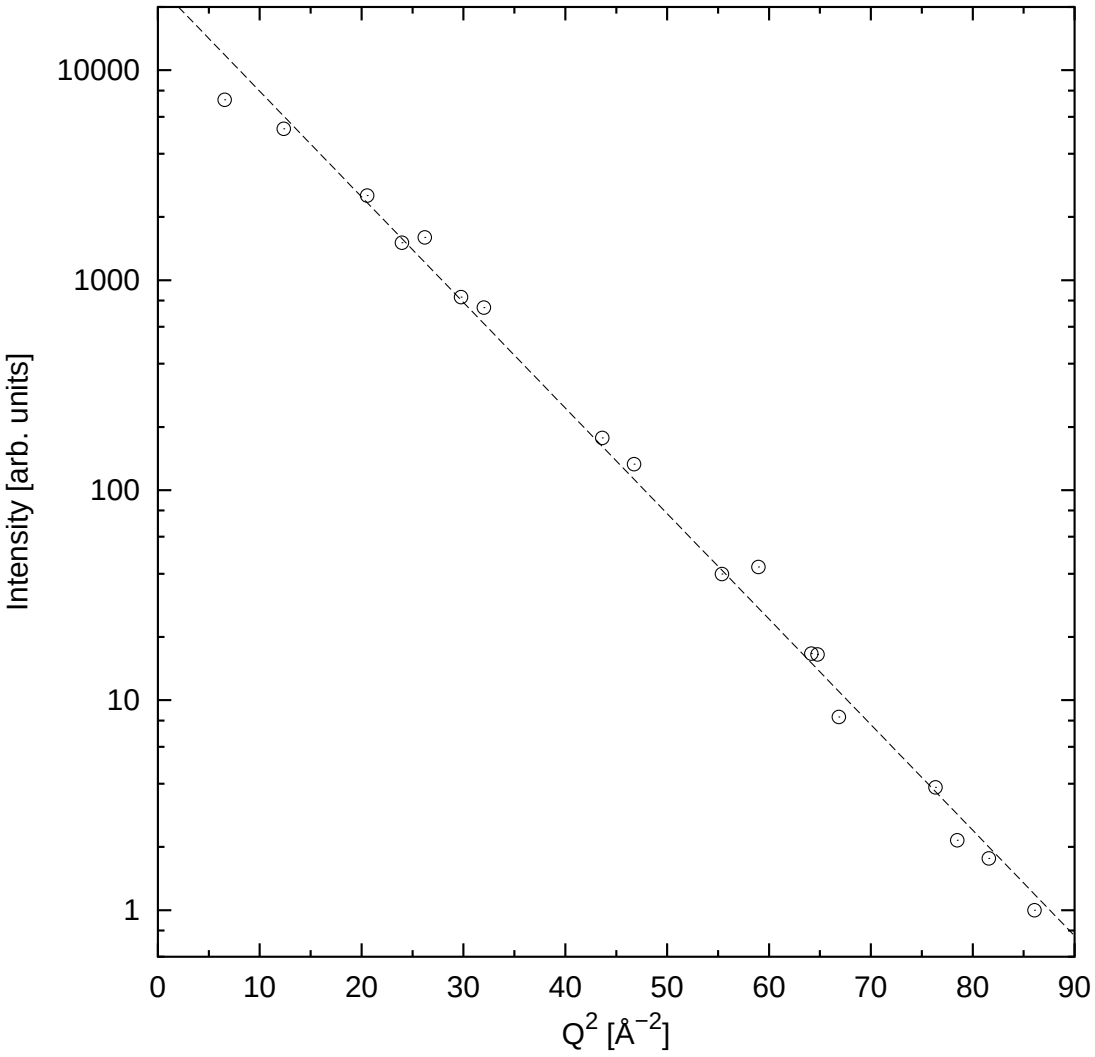

Figure 4.20: APS crystal 12 Q-dependent measurement. The crystal is hcp ^{3}He, while the conditions are a molar volume of 11.607 cm^3 and a temperature of 16.90 K.

One standard way to present the $\langle u^2 \rangle$ data is through the use of equivalent Debye temperatures. This practice comes from the tradition of expressing the heat capacity of materials in terms of the Debye temperature. This is a way to compare the measured values to the Debye model. It is also convenient since measured C_V and $\langle u^2 \rangle$ values can span several several orders of magnitude over a sufficient temperature range, while the Debye temperatures do not vary too much.

The method of determination of the Debye temperature was shown in Sec. 2.2.2, where

$$\langle u^2 \rangle \, T = \left(\frac{3\hbar^2}{m k_{\mathrm{B}}} \right) \frac{1}{x^2} \left[\Phi(x) + \frac{x}{4} \right] \qquad \text{and} \qquad x \equiv \frac{\Theta_M}{T} \,, \tag{4.23}$$

with $\Phi(x)$ being the Debye integral. If a value of $\langle u^2 \rangle$ is known for a given temperature T, a value of x can be found. The values of m for both ^{3}He and ^{4}He are in Appendix D.3. Finding a value of x is not easy due to the Debye integral, and in past years tables of values for the right side of the first equation (excluding the constant) were used [8]. In this day of powerful computers, it is much easier to solve for x numerically with the use of a computer program. The values presented here were generated by a data analysis program, written in the C programming language. Once the value of x has been found, multiplication of it with T gives the Debye temperature, Θ_M.

The resulting Debye temperatures for the measurements are given in tables 4.10 and 4.11. They are plotted logarithmically versus the molar volume in Figs. 4.21 and 4.22, although the data points have not been corrected for having been taken at different temperatures.

4.5.2 *T*-Dependent Data

T-dependent Debye-Waller data are collected using only one reflection, where rocking curves are taken at different temperatures. Each set of data produces values of $d\langle u^2 \rangle / dT$ for the temperature range of the measurements. Values of $\langle u^2 \rangle$ from Q-dependent measurements can be used to represent a set of data as absolute $\langle u^2 \rangle$ values, instead of relative values.

The temperature derivative of $\langle u^2 \rangle$ is found by means of

$$\frac{d}{dT} \langle u^2 \rangle = -\frac{1}{Q^2} \frac{d}{dT} \ln(I) \,, \tag{4.24}$$

where Q is that of the reflection used for the measurements. Since experimental measurements

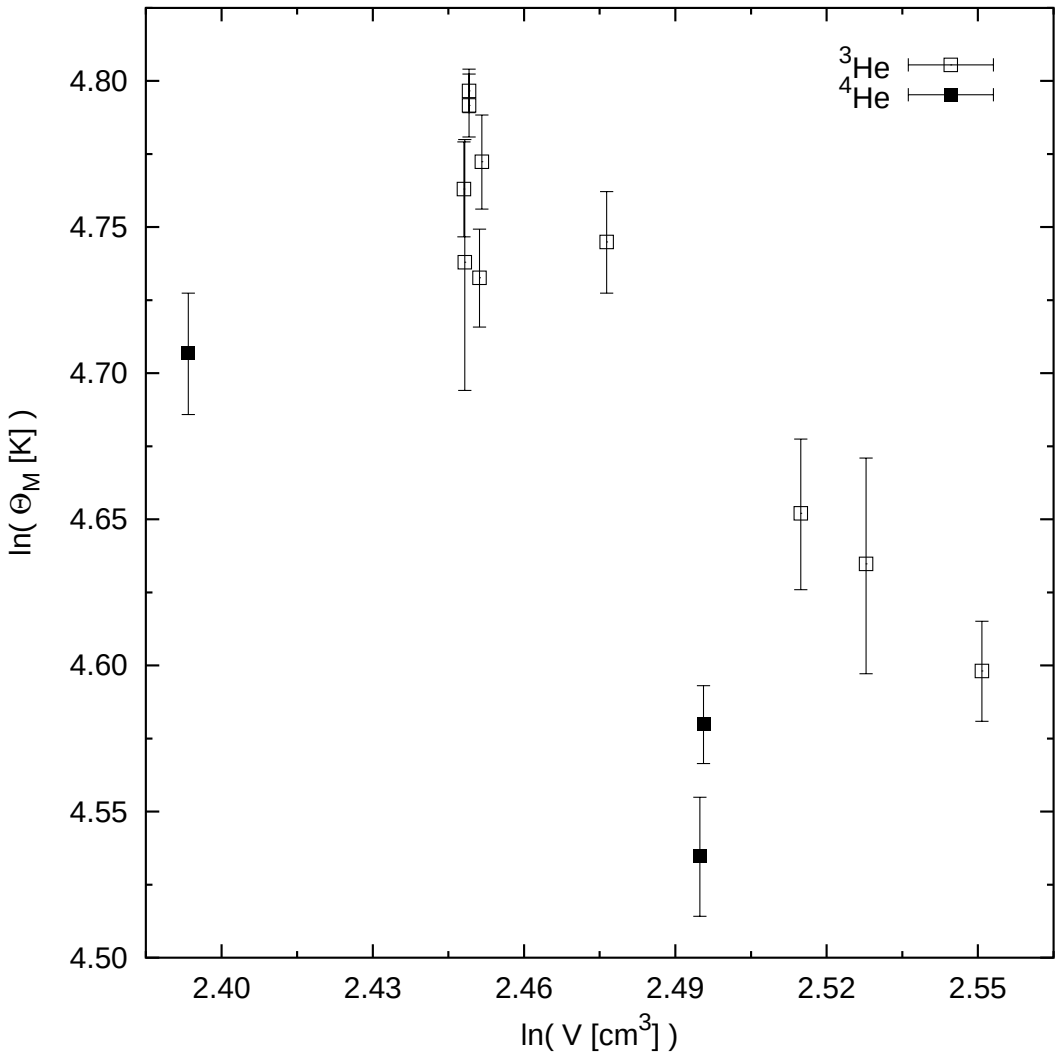

Figure 4.21: Natural logarithm of the Debye temperature versus natural logarithm of the molar volume for both ^{3}He and ^{4}He, with all the measurements taken at various temperatures. Fig 4.22 is an expanded plot of the cluster of ^{3}He data points.

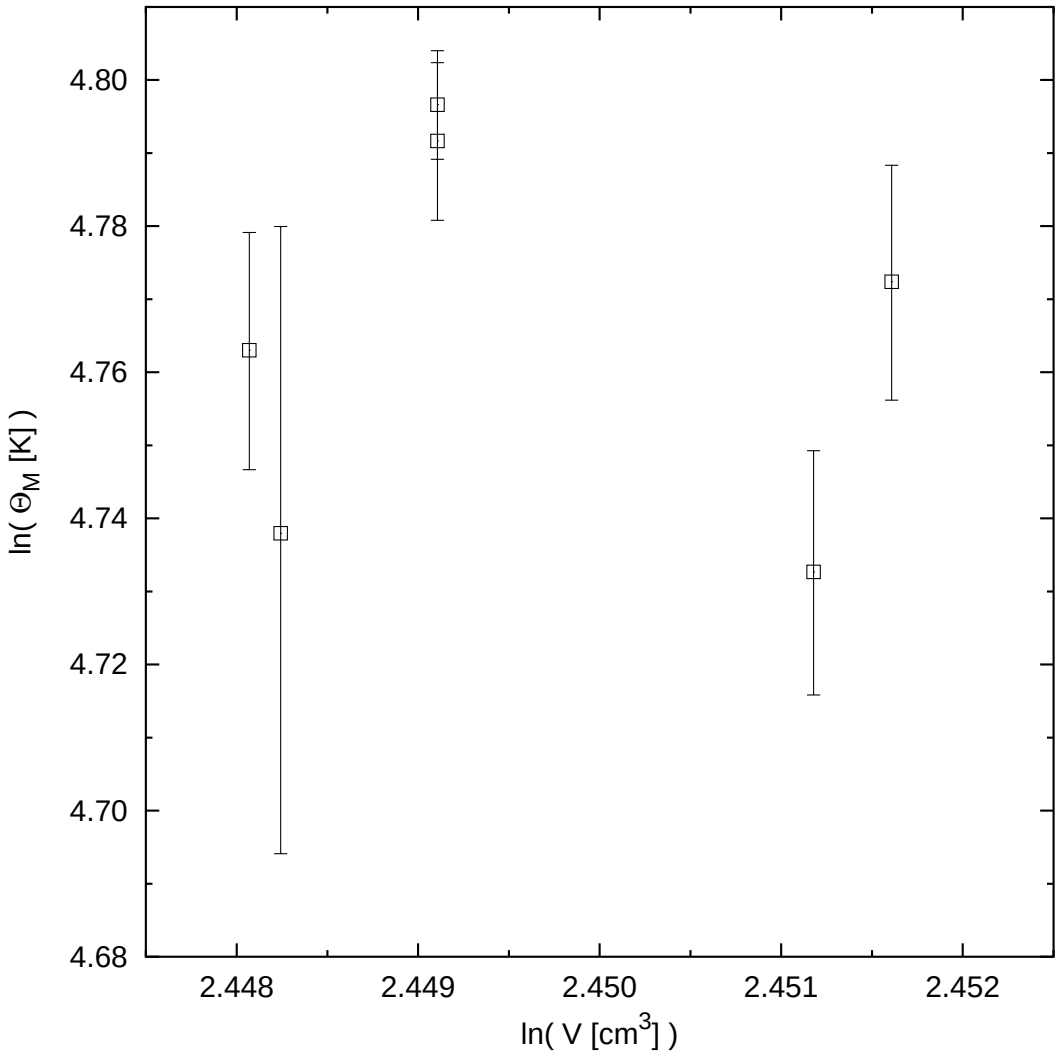

Figure 4.22: Expanded scale plot of natural logarithm of the Debye temperature versus natural logarithm of the molar volume for ^{3}He. The measurements were taken at various temperatures.

involve finite temperature steps, the actual formula used for analyzing the data is

$$\frac{\Delta\langle u^2\rangle}{\Delta T} = -\frac{1}{Q^2}\left(\frac{\Delta \ln(I)}{\Delta T}\right) . \tag{4.25}$$

This is fine as long as ΔT is small and the relationship between T and $\ln(I)$ is relatively smooth, which is the case for the data in this thesis.

The following paragraphs discuss the problem encountered when taking T-dependent measurements with the setup described in this thesis; internally-consistent Q-dependent measurements are the more reliable route to reliable temperature-dependent $\langle u^2\rangle$ values. The best way to check the reliability of T-dependent measurements is to take multiple identical measurements and compare them.

Ideally, constant volume should be maintained so the measurements would be for a constant molar volume (if vacancies don't occur in great numbers). A constant volume was expected for the measurements, but unfortunately the data were not taken under this condition. A solid helium plug forms in the fill line. Since frozen helium is rather soft and does not make a very consistent plug, it will sometimes move after a temperature change, and sometimes it will not. This was seen in measurements of the lattice parameters when looking for vacancies, where the lattice parameters would jump in value every few temperature steps. So, the data presented have a caveat that they were taken with neither constant volume or constant pressure.

Another problem with this type of data is that the crystal is unstable during temperature changes. The fraction of the single crystal under study in the beam can change during the ramping up or down in temperature. These temperature changes can also cause single crystals to merge with others. These effects are discussed in Appendix G.7.5.

The T-dependent data for hcp ^{3}He were taken using the (3 0 0) peak, with the molar volume near 11.60 cm^3; Fig. 4.23 is a plot of these data. The T-dependent data for hcp ^{4}He were taken using the (2 1 $\bar{3}$) peak, with the molar volume near 12.12 cm^3; Fig. 4.24 is a plot of these data.

Values for $d\langle u^2\rangle/dT$ are found by applying Eq. 4.25 to both sets of data. Intensity measurements made within 0.02 K of each other are combined into an average value in order to simplify the calculations. The results of this analysis are plotted in Fig. 4.25.

T-dependent data can be used to calculate $\Delta\langle u^2\rangle$ using Eq. 4.25, where both sides are multi-

plied by ΔT, leaving

$$\Delta\langle u^2\rangle = -\frac{1}{Q^2}\,\Delta\ln(I)\,. \tag{4.26}$$

If a set of Q-dependent measurements was taken at the same molar volume as the T-dependent measurements, and if the measurement temperature of the former matches any of the measurement temperatures of the latter, the T-dependent measurements can be converted into $\langle u^2\rangle$ values. This is done by merely adding or subtracting $\Delta\langle u^2\rangle$ from the $\langle u^2\rangle$ value found from the set of Q-dependent measurements. Once $\langle u^2\rangle$ values are calculated, Θ_M values can be calculated as described in Sec. 4.5.1.

Both $\langle u^2\rangle$ and Θ_M values are computed for both sets of data. Intensity measurements made within 0.02 K of each other are combined into an average value in order to simplify the calculations. Errors for $\Delta\langle u^2\rangle$ are hard to estimate, since two independent identical measurements would have had to been taken for each data set. Errors for the derived $\langle u^2\rangle$ values are a combination of the error from the reference Q-dependent $\langle u^2\rangle$ value as well as from the $\Delta\langle u^2\rangle$; also, the further the derived $\langle u^2\rangle$ is from the reference $\langle u^2\rangle$, the larger the error becomes.

For the crystal 3 data, since no T-dependent measurement was made at the same temperature as the 11.52 K Q-dependent measurement, a value was interpolated from a linear fit to the T-dependent data; this interpolation was for only a 0.4 K difference. A graph of the resulting $\langle u^2\rangle$ values for crystal 3 is in Fig. 4.26, while a similar graph for the Debye temperatures is in Fig. 4.27.

For the crystal 18 data, the $\langle u^2\rangle$ value from the 12.00 K Q-dependent measurement was used with the 12.00 K T-dependent measurement. A graph of the resulting $\langle u^2\rangle$ values for crystal 18 is in Fig. 4.28, where the experimental 14.23 K value is shown for comparison; a similar graph for the Debye temperatures is in Fig. 4.29. Error bars for the two T-dependent values near the 14.23 K Q-dependent value are from the 12.00 K Q-dependent reference value, and is a minimum error for these two values. Comparing the 14.23 K Q-dependent value to the T-dependent values, they agree within the errors.

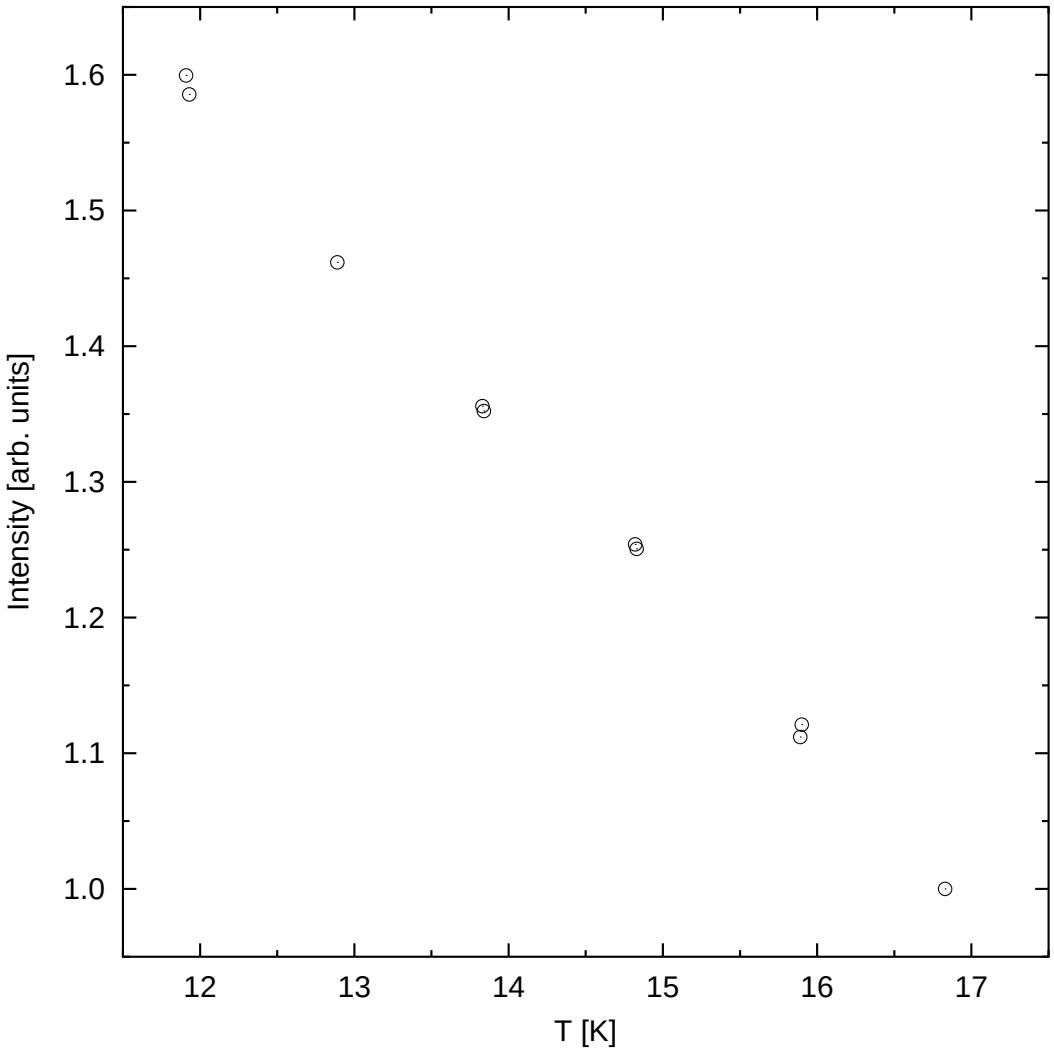

Figure 4.23: NSLS crystal 3 T-dependent measurement. The crystal is hcp ^{3}He and the (3 0 0) peak was used, with the the molar volume being 11.60 cm^3.

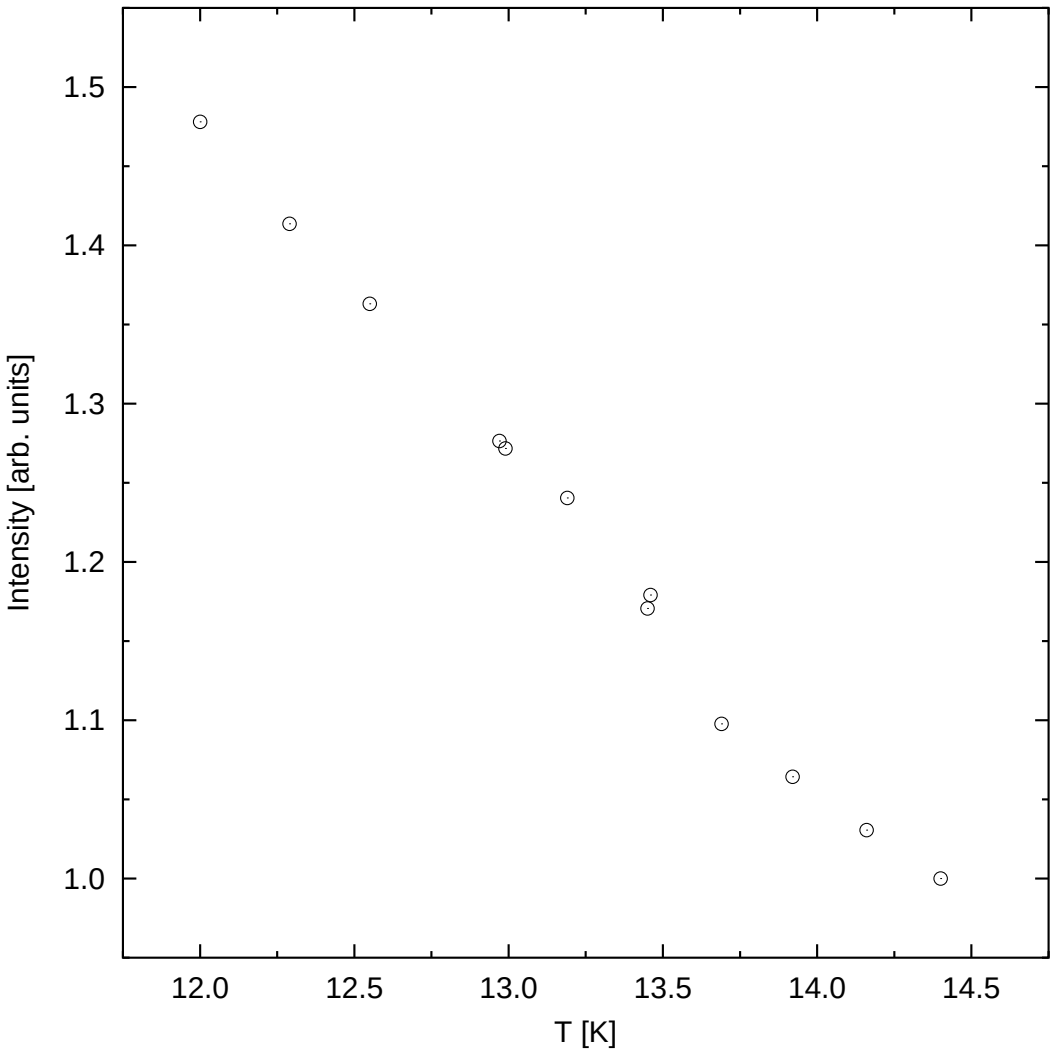

Figure 4.24: NSLS crystal 18 T-dependent measurement. The crystal is hcp ^{4}He and the $(2\,1\,\bar{3})$ peak was used, with the molar volume being 12.12 cm^3. The jog near 13.5 K occurred when the temperature controller's heater range was changed.

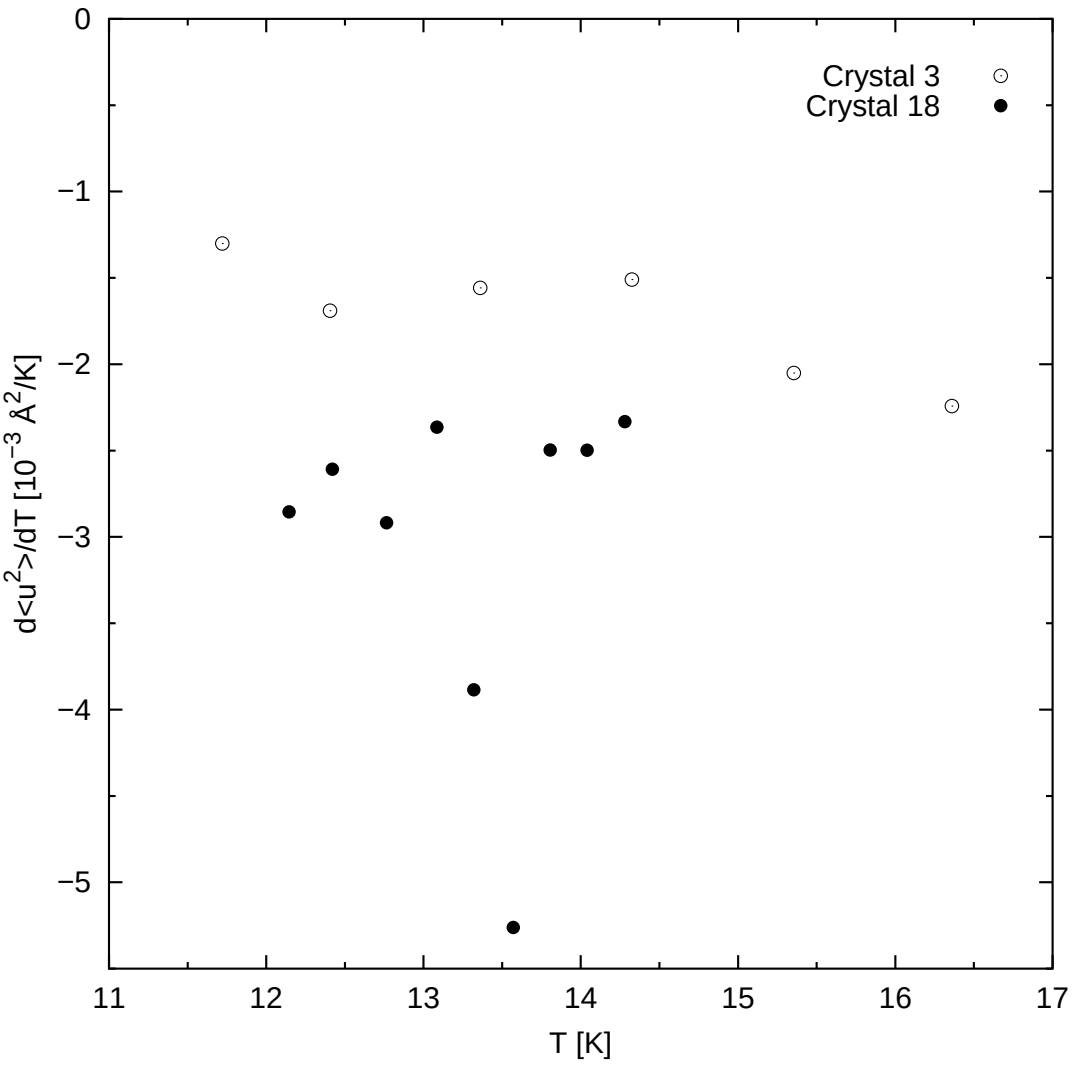

Figure 4.25: Calculated $d\langle u^2\rangle/dT$ values for NSLS crystals 3 and 18. crystal 3 is hcp ^{3}He, with a molar volume of 11.60 cm^3. Crystal 18 is hcp ^{4}He, with a molar volume of 12.12 cm^3. The downward spike near 13.5 K for crystal 18 occurred when the temperature controller's heater range was changed.

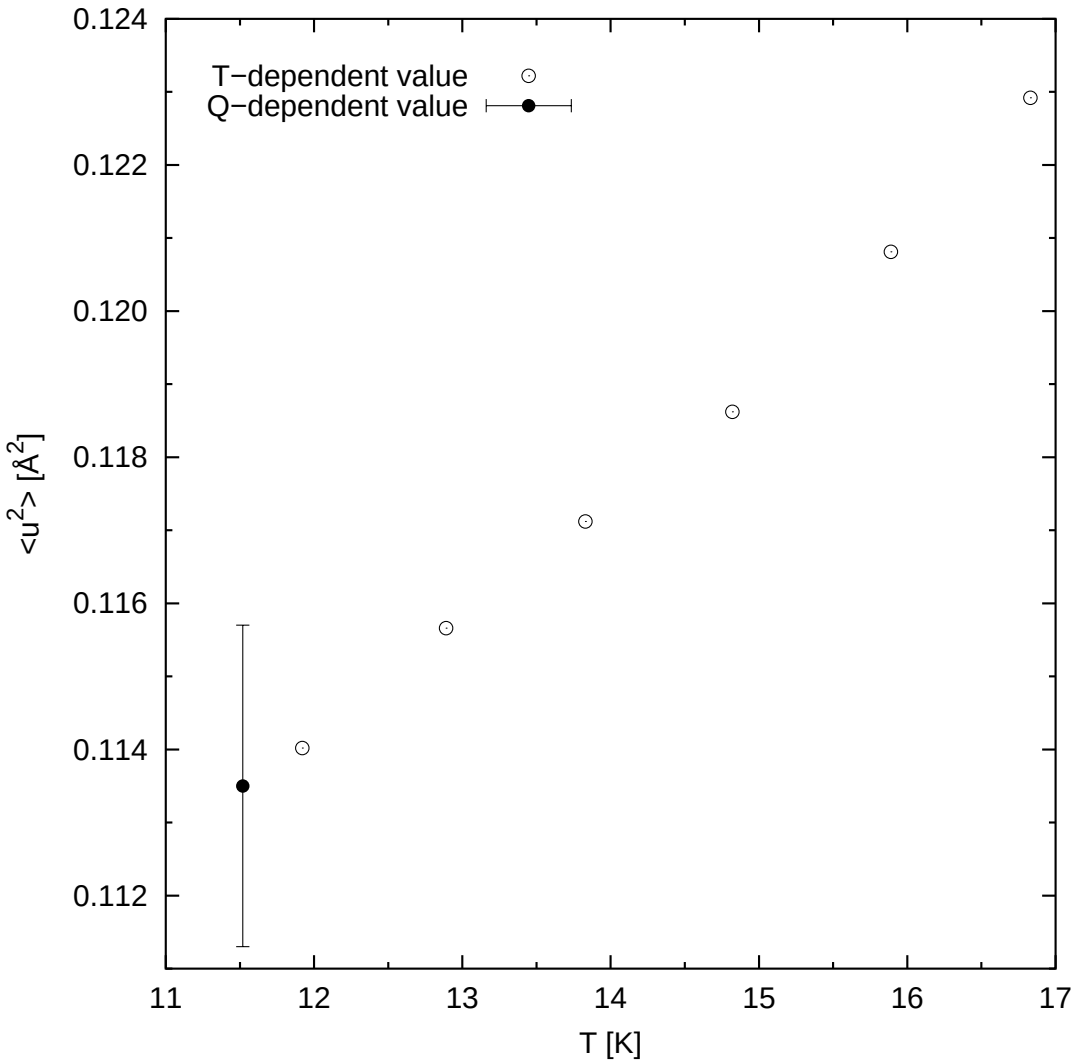

Figure 4.26: NSLS crystal 3 derived $\langle u^2 \rangle$ values. The crystal is hcp ^{3}He and the (3 0 0) peak was used, with the molar volume being 11.60 cm^3. The T-dependent values are based on a linear interpolation to the 11.52 K Q-dependent value, with errors somewhat larger that that of the Q-dependent measurement itself.

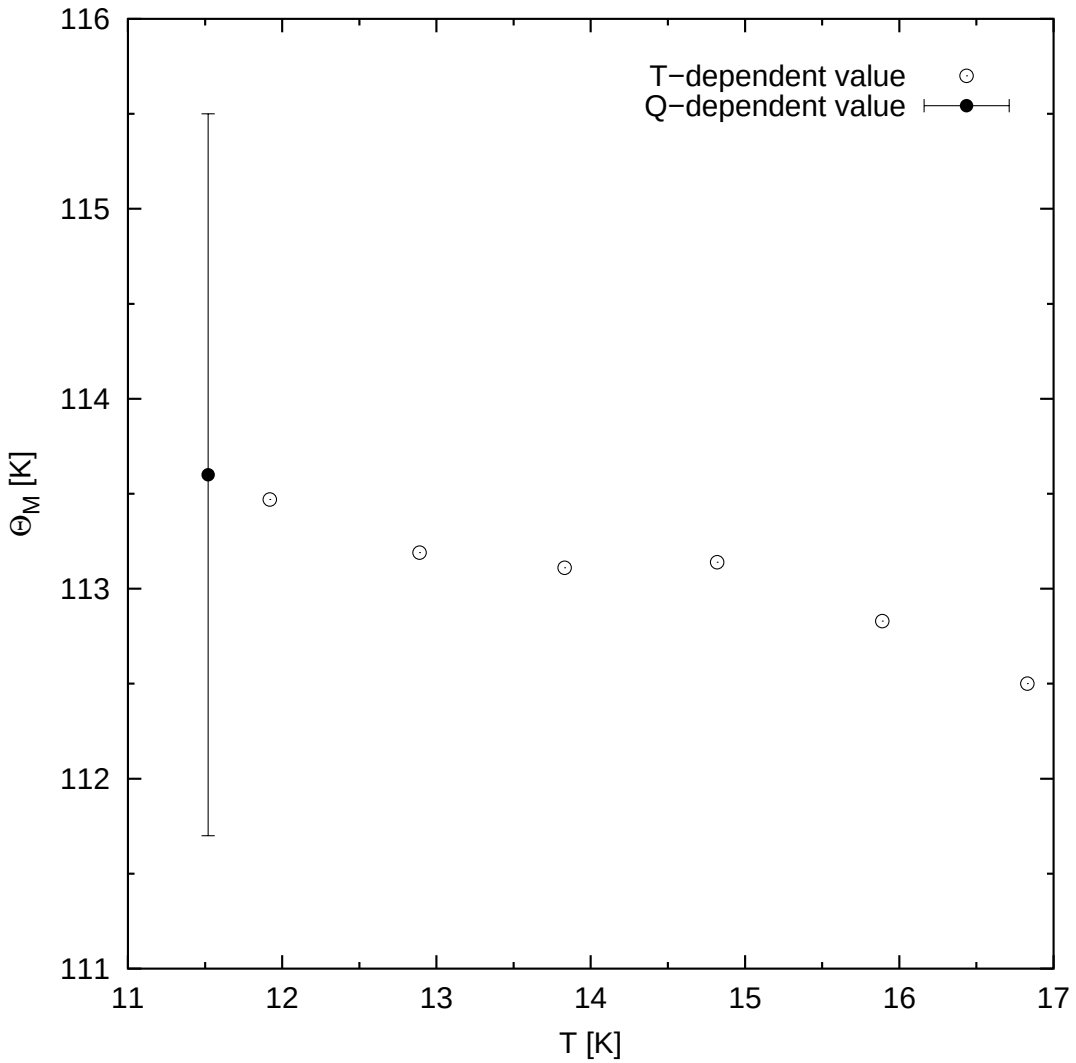

Figure 4.27: NSLS crystal 3 derived Θ_M values. The crystal is hcp ^{3}He and the (3 0 0) peak was used, with the molar volume being 11.60 cm^3. The T-dependent values are based on a linear interpolation to the 11.52 K Q-dependent value, with errors somewhat larger that that of the Q-dependent measurement itself.

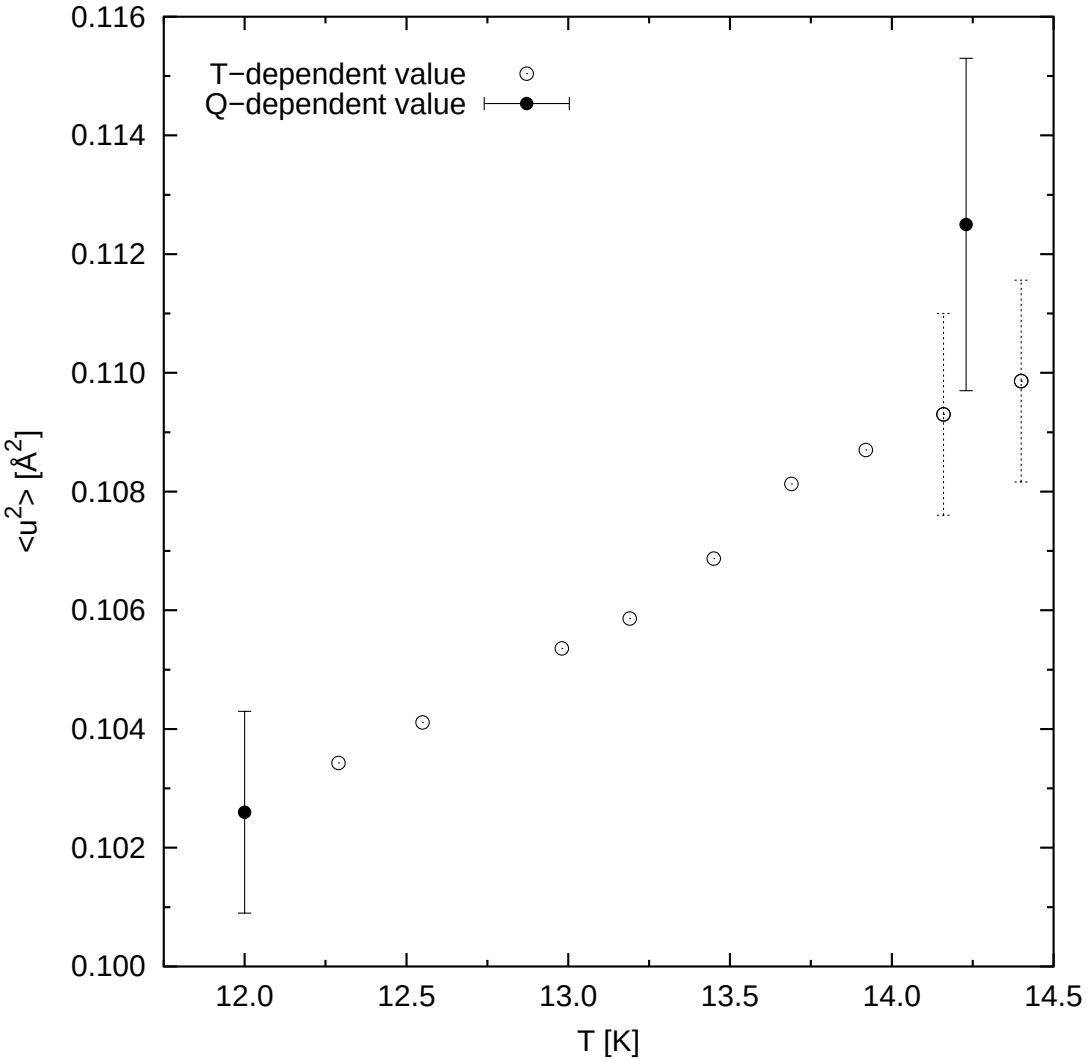

Figure 4.28: NSLS crystal 18 derived $\langle u^2 \rangle$ values. The crystal is hcp ^{4}He and the $(2\,1\,\bar{3})$ peak was used, with the molar volume being 12.12 cm^3. The T-dependent values are based on the 12.00 K Q-dependent value. The error bars for the two highest temperature T-dependent values are those of the 12.00 K Q-dependent measurement, and represent a minimum error value for each. The 14.23 K Q-dependent measurement agrees with the T-dependent measurments, within the respective estimated errors.

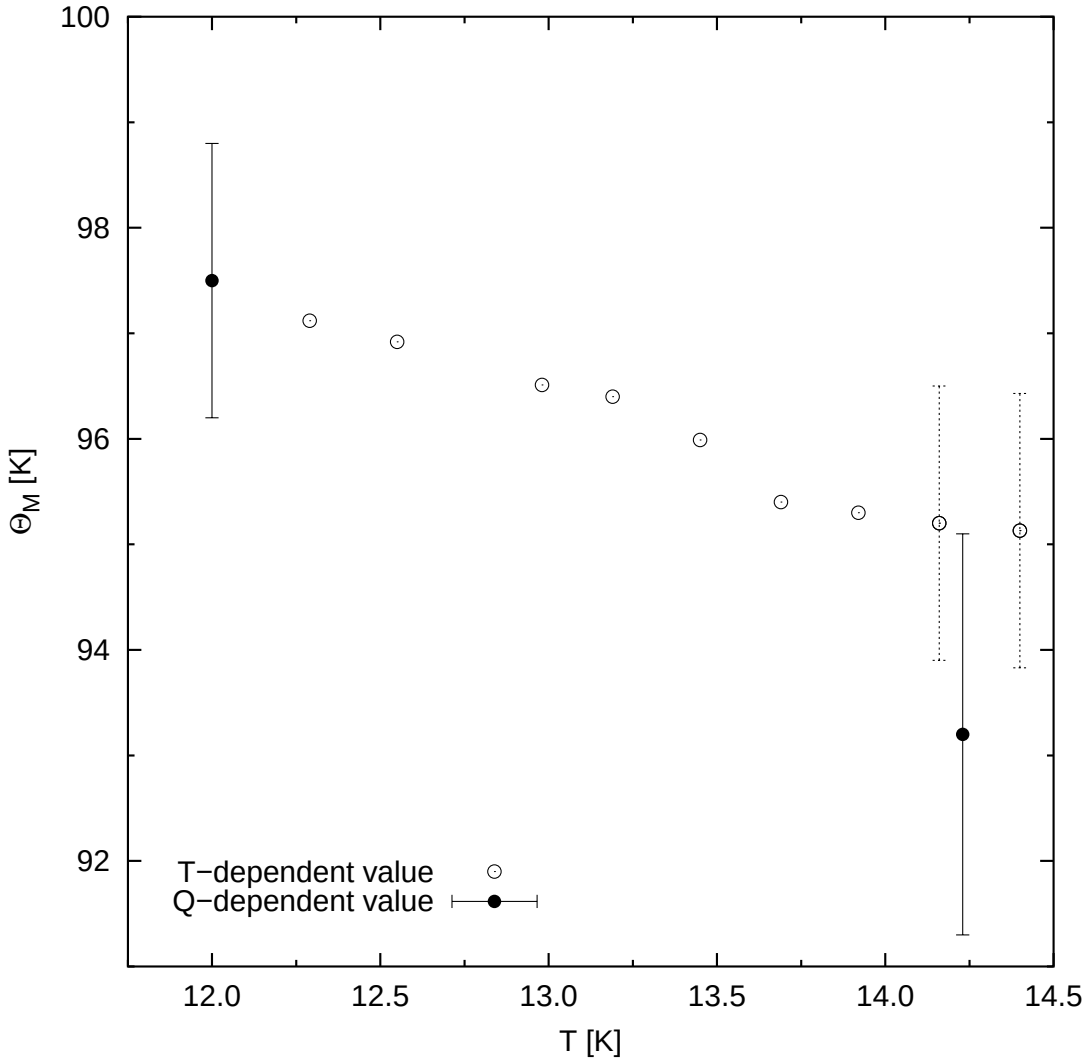

Figure 4.29: NSLS crystal 18 derived Θ_M values. The crystal is hcp ^{4}He and the $(2\,1\,\bar{3})$ peak was used, with the molar volume being 12.12 cm^3. The T-dependent values are based on the 12.00 K Q-dependent value. The error bars for the two highest temperature T-dependent values are those of the 12.00 K Q-dependent measurement, and represent a minimum error value for each. The 14.23 K Q-dependent measurement agrees with the T-dependent measurments, within the respective estimated errors.

References

[1] A. W. Stevenson and J. Harada, Acta Crystallogr. Sect. A **39**, 202 (1983).

[2] C. B. Walker and D. R. Chipman, Acta Crystallogr. Sect. A **26**, 447 (1970).

[3] M. Sakata, A. W. Stevens, and J. Harada, J. Appl. Cryst. **16**, 154 (1983).

[4] L. D. Jennings, Acta Crystallogr. Sect. A **26**, 613 (1970).

[5] R. Bachmann, H. Kohler, H. Schulz, and H. Weber, Acta Crystallogr. Sect. A **41**, 35 (1985).

[6] Z. Su and P. Coppens, Acta Crystallogr. Sect. A **53**, 749 (1997).

[7] W. H. Press, S. A. Teukolsky, W. T. Vetterling, and B. P. Flannery, in *Numerical Recipes in C* (Cambridge, New York, 1992), Chap. 15.

[8] G. C. Benson and E. K. Gill, Can. J. Phys. **44**, 674 (1966).

Chapter 5

Comparisons and Discussion

5.1 Previous Q-Dependent Debye-Waller Measurements

The only previous measurements of this type were done with ^{4}He, so no comparisons with previous data are possible for ^{3}He. There have been three separate measurements done for ^{4}He.

The first measurement for ^{4}He was with neutrons by Stassis et al. [1]. The method of using neutrons to find the Debye-Waller factor is essentially the same as the method of using X-rays [2]. This method could not be attempted for ^{3}He, since ^{3}He has an extremely high absorption rate for neutrons; not only would the scattered flux be reduced, but the sample itself would be altered as the ^{3}He would turn into ^{1}H, ^{3}H, and thermal energy. The other two measurements for ^{4}He were with X-rays by Venkataraman [3], and Burns and Isaacs [4].

The data from these sources are summarized in Table 5.1, where the equivalent Debye temperatures were calculated either for the first time or were redone using a computer program written in the C language. None of these measurements were taken where both molar volume and temperature conditions were similar to that of a measurement in this thesis.

5.2 Previous T-Dependent Debye-Waller Measurements

The only known previous measurement of this type is on fcc ^{4}He, by Venkataraman [3]. In that thesis, $(\partial\langle u^2\rangle/\partial T)_V$ was calculated from the data, and the two data sets of this type are at much different molar volumes than data in this thesis.

5.3 Other Types of Data

A few other types of data can be considered. Heat capacity and phonon dispersion curve measurements can be used to derive a value for $\langle u^2\rangle$, although these values are indirect since they

Table 5.1: Previous Debye-Waller Measurements of ^{4}He

Structure	V [cm^3]	T [K]	$\langle u^2 \rangle$ [Å^2]	Θ_M [K]
hcp	12.06	5.8	0.09322[a]	99.68 ± 0.50
hcp	15.72	5.8	0.1722[a]	56.45 ± 0.50
fcc	10.14	26.94	0.0887 ± 0.0038[b]	130.6 ± 3.5
fcc	10.24	25.94	0.0843 ± 0.0018[b]	133.9 ± 2.1
fcc	10.46	23.84	0.1027 ± 0.0062[b]	113.7 ± 4.9
fcc	10.51	23.01	0.0988 ± 0.0007[b]	115.5 ± 0.6
fcc	10.37	24.40	0.0823 ± 0.0040[b]	134.4 ± 4.9
hcp	20.9	0.7	0.307 ± 0.013[c]	29.8 ± 1.3

[a] Neutron measurement by Stassis et al. [1].
[b] X-ray measurement by Venkataraman [3].
[c] X-ray measurement by Burns and Isaacs [4].

depend upon a model. The effect the mass of the atom for the two helium isotopes has on the equivalent Debye temperature can be compared to that which is predicted by a simple theoretical analysis. As a way of looking for anharmonicities, peaks can be searched for at forbidden locations (almost-forbidden reflections).

5.3.1 Heat Capacity Measurements

There have been several measurements of the heat capacity of both ^{3}He and ^{4}He, which also gave Debye temperatures [5, 6, 7, 8, 9]. From these heat capacity measurements, Θ_{C_V} was calculated. These measurements were taken over a wide temperature range, creating curves that go towards $T = 0$, giving an approximate value of $\Theta_{C_V}(T = 0)$.

For two sets of ^{4}He measurements [8, 9], enough such values at different molar volumes were taken to allow a fit to a Grüneisen parameter at $T = 0$, $\gamma_{C_V}(0)$. The expression found for the combined data is

$$\gamma_{C_V}(0) = 0.8114 + 0.09690\, V \qquad 26 \leq V[\text{cm}^3] \leq 13.7\ . \tag{5.1}$$

The temperature dependence of $\gamma_{C_V}(T)$ at low temperatures is very slight, with it increasing as the molar volume increases. For $V = 13$ cm^3 and $T = 10$ K (conditions close to those of the

samples in this thesis), $\gamma_{C_V}(10\,\mathrm{K})/\gamma_{C_V}(0) \approx 1.02$ [8]. There are not enough measurements for ^{3}He in order to get a fit for $\gamma_{C_V}(0)$, although it has been observed that the few ^{3}He measurements that exist conform to Eq. 5.1 [8]. Because of this, for this thesis, the Grüneisen parameter is approximated as being temperature independent, γ_{C_V}, and being the same for both ^{3}He and ^{4}He, using Eq. 5.1 as its value. The molar volumes in this thesis are slightly smaller than those allowed by this fit, but this fit is the only one available, so it's used. From Eqs. 2.68 and 2.70 which apply to harmonic models, Θ_{C_V} and Θ_M correspond to different low-order moments of the one-phonon frequency spectrum, $\omega_{\mathrm{D}}(-3)$ and $\omega_{\mathrm{D}}(-1)$ respectively. Nevertheless, it is assumed here that γ_{C_V} (as measured from Θ_{C_V}) will be the same as γ_M, which will be used in the rest of this thesis. This Grüneisen parameter can be integrated to give a relationship between $\ln(\Theta_M)$ and $\ln(V)$, namely

$$\ln(\Theta_M) = -0.8114\,\ln(V) - 0.09690\,V + \text{constant} \qquad \Theta_M\,[\mathrm{K}],\, V\,[\mathrm{cm}^3]\,. \tag{5.2}$$

This relationship can be used to scale measurements that are at different molar volumes, allowing direct temperature comparisons of data.

5.3.2 Phonon Dispersion Measurements

There are several measurements of the phonon dispersion relations along different directions for ^{4}He using inelastic neutron scattering [10, 11, 12, 13, 14, 15]. From these data, a one-phonon density of states can be generated, using a fit to a Born-von Kármán model. This density of states can be used to calculate a value of $\langle u^2 \rangle$, but such a procedure is indirect and neglects the considerable multi-phonon processes present in helium crystals. Values calculated this way do not agree with direct experiment or PIMC computations.

In order to include some multi-phonon processes, it is also possible to calculate M values from the heat capacity data using an ACB sum rule [16], which takes into account single phonon processes plus only multiphonon processes that have a single phonon as some intermediate stage [12]. This view has been applied to the analysis of phonon intensity data [11], where it predicts a nonlinear $\ln(I)$ versus Q^2 relation, in apparent agreement with some of the neutron inelastic data. However, this is not seen in any of the experimental Debye-Waller measurements, including the present ones, which average over all phonon excitations.

There have also been measurements for ^{3}He and ^{4}He using inelastic X-ray scattering [17]. These x-ray studies however concentrated on specific branches of the phonon spectra and are not sufficient to be used for Born-von Kármán fitting. Analysis of the inelastic x-ray data using observed lifetimes and ACB concepts for excitation intensities was consistent with strong multiphonon excitations in the extended zone for reduced Q values between 1 and 2.

5.3.3 Isotopic Effects

Because of the difference in mass for the two helium isotopes, corresponding phonons in both isotopic crystals (of the same molar volume) will have different vibrational frequencies. For a harmonic crystal, the phonon frequency is dependent upon mass as $m^{-1/2}$, giving the harmonic ^{3}He-^{4}He frequency ratio as $\sqrt{4/3} \approx 1.155$. Since the Debye temperature is defined as

$$\Theta_{\mathrm{D}} \equiv \frac{\hbar\omega_{\mathrm{D}}}{k_{\mathrm{B}}}\,, \tag{5.3}$$

it scales with mass as the Debye frequency does. The equivalent Debye temperatures at $T = 0$ for a general harmonic solid also has the same mass dependence.

Several sources give experimental values for the ^{3}He-^{4}He ratio. Sample and Swenson [6] give a value of 1.18, using heat capacity data in the hcp phase, where the low temperature limit of the Debye temperature, $\Theta_{C_V}(T \to 0)$, is used; the fact this corresponds to the moment $\omega_{\mathrm{D}}(-3)$ needs to be considered. Slusher and Surko [18] give a value of 1.17 ± 0.01 for the transverse optical phonons near $K = 0$, using Raman scattering. Seyfert et al. [17] give an average value of 1.11 ± 0.05 for the longitudinal phonons along the $<1\,0\,0>$ direction, using inelastic X-ray scattering. A more complete account of experimental findings is given by Seyfert [19].

5.3.4 Almost-Forbidden Reflections

One way to look for anharmonicities is by looking for peaks at the locations of the forbidden peaks of a crystal with a basis. For helium, this means an hcp crystal. These peaks at forbidden locations are called "almost-forbidden" reflections. According to estimates, almost-forbidden peaks should be visible in hcp helium, although they should be very weak [20]. For hcp crystals, the condition for forbidden reflections can be written as when $h = k + 3n$ for any integer n and ℓ is

odd; anharmonicities would cause almost-forbidden peaks to appear at those values, except for the case of $n = 0$, where the reflections are still forbidden [21]. The (3 0 1) peak is the reflection with the lowest Q value for helium, but since allowed peaks at comparable Q values were very weak, it was impossible to find this reflection. The lower Q forbidden peaks (0 0 1), (0 0 3), and (1 1 1) were searched for at the Advanced Photon Source and no peaks were found, while at the National Synchrotron Light Source, a peak was found at (1 1 1) position. The (1 1 1) peak was most likely due to either multiple reflections or stacking faults; the crystal was not rotated about the reflection to see if the multiple reflection possibility could be ruled out. Burns and Isaacs [4] also saw peaks at the (0 0 1) and (0 0 3) reflections, which were attributed to stacking faults or strains caused by passing through a bcc-hcp transition.

5.4 Computations

Values of $\langle u^2 \rangle$ can be computed for He through the use of path-integral Monte Carlo [22]. Ceperley did computations that matched measurement conditions for data in this thesis and also for Venkataraman [3]. It was initially found that these computations disagreed somewhat with experiment; this was found to be due to a need for larger simulation samples. This led to work by Draeger and Ceperley [23], where a way of extrapolating computational values to samples of infinite size was found, and more computations were made to match measurements in this thesis.

The computations exhibit a finite size scaling consistent with a crossover between the quantum and classical limits, which are $N^{-2/3}$ and $N^{-1/3}$ respectively, where N is the size of the sample used for a computation. In order to find a value for when $N = \infty$, several computations with different N were made and a fit was made to a crossover model, which predicted the asypmtotic limit. For computations at conditions corresponding to experimental measurements presented in this thesis, the resulting asymptotic values agree quite well with experimental measurements for all but one case.

From several sets of computations, $\langle u^2 \rangle$ values were able to be fit to a model of the form

$$\langle u^2 \rangle = a + b\,T^3\,, \tag{5.4}$$

where a and b are parameters. This T^3 temperature dependence is different from the T^2 temperature

dependence expected for a harmonic crystal. If a curve of this type is converted into a corresponding Θ_M curve, this new curve has a maximum just above $T = 0$. This maximum is unexpected in a harmonic model, because the usual low-temperature series expansions for the respective Debye equivalent temperatures show monotonic behavior. This maximum implies that either the fit does not detect any lower-order terms in T or this is caused by the anharmonic nature of helium.

For the case of hcp crystals, the computations were done using a lattice where the c/a ratio is set to be ideal. As discussed before, this is very close to the observed c/a ratio.

Of the computations made, there is one for fcc ^{3}He and fcc ^{4}He, both at $V = 10.98$ cm^3 and $T = 17.78$ K. If the $\langle u^2 \rangle$ values are converted to equivalent Debye temperatures, they give a value of 1.183 ± 0.004 for the ^{3}He-^{4}He frequency ratio (as discussed in Sec. 5.3.3). This is not too far from the ideal value of $\sqrt{4/3} \approx 1.155$. Since this type of comparison for the PIMC values was made for only one pair of available computations, the true accuracy of this value is not well defined.

The computations for fcc show a small non-Gaussian shape for the atomic displacement (coming from Eq. 2.17), being of the form

$$\ln\left(I/I_c\right) = -2M' \equiv -\langle u^2 \rangle\, Q^2 - \xi\, Q^4\,, \tag{5.5}$$

where I is the measured intensity, I_c is a constant, M' is the first-order corrected Debye-Waller factor, and ξ is a variable composed of $\langle u^2 \rangle^2$ and $\langle u^4 \rangle$. The correction comes in the form of a non-zero ξ, making the Debye-Waller factor a quadratic expression in Q^2. I/I_c values were calculated for $<1\,0\,0>$ and $<1\,1\,1>$ directions, with the non-zero ξ being evident when these values are plotted as $Q^{-2}\ln(I/I_c)$ versus Q^2. Both sets of computations end up being linear with differing slopes (which correspond to differing ξ values). The significance of this is that PIMC predicts the non-Gaussian shape of the atomic displacement (due to the non-zero values of ξ), as well as predicting an anisotropy for the Debye-Waller factor (due to the two reciprocal directions having differing values of ξ).

Computations were done matching six measurements. These PIMC calculated $\langle u^2 \rangle$ values, with equivalent Debye temperatures calculated by Mathematica, are given in Table 5.2, followed by the corresponding experimental values for comparison. From this table, it can be seen that each set of PIMC and experimental values agree within the respective stated uncertainties.

Three sets of computations were also done at the same molar volume of a measurement at a

Table 5.2: Results from PIMC Computations and Their Experimental Counterparts

No.[a]	Structure	Isotope	V [cm^3]	T [K]	$\langle u^2 \rangle$ [Å^2]	Θ_M [K]
1	fcc	3	11.54	17.78	0.1141 ± 0.0040	120.9 ± 3.4
2	hcp	3	11.90	16.84	0.1184 ± 0.0024	116.0 ± 1.9
3	hcp	3	12.81	12.31	0.1326 ± 0.0019	100.0 ± 1.2
4	fcc	4	10.98	20.00	0.0977 ± 0.0039	112.3 ± 3.4
5	hcp	4	12.12	14.55	0.1117 ± 0.0013	94.1 ± 0.9
6	hcp	4	12.12	11.85	0.1024 ± 0.0013	97.4 ± 1.1
No.	Measurement Label		V [cm^3]	T [K]	$\langle u^2 \rangle$ [Å^2]	Θ_M [K]
1	NSLS 4A		11.578	18.13	0.1143 ± 0.0011	121.1 ± 0.9
	NSLS 4B				0.1150 ± 0.0015	120.5 ± 1.3
2	NSLS 12		11.898	16.81	0.1196 ± 0.0026	115.0 ± 2.0
3	NSLS 15		12.817	12.54	0.1343 ± 0.0027	99.3 ± 1.7
4	NSLS 16		10.951	20.25	0.0999 ± 0.0027	110.7 ± 2.3
5	NSLS 18A		12.120	14.23	0.1125 ± 0.0028	93.2 ± 1.9
6	NSLS 18B		12.129	12.00	0.1026 ± 0.0017	97.5 ± 1.3

[a] PIMC calculations done by Draeger and Ceperley [23].

number of different temperatures, corresponding to NSLS crystals 4, 16, and 18. The conditions for most of the values are such that, experimentally, the crystal would be in the hcp phase. However, two of these sets of computations are done for an fcc crystal, to see a trend up to the two experimental fcc values. The crystal 16 set has a large number of values, done to show that the temperature dependence of $\langle u^2 \rangle$ conforms to Eq. 5.4.

The graphs of the $\langle u^2 \rangle$ values for NSLS crystals 4, 16, and 18, as well as plots of their fits to a $a + bT^3$ model, are shown in Figs. 5.1, 5.2, and 5.4 respectively. On these graphs, the associated experimental values are shown for comparison, and they agree with the nearest PIMC value within error bars.

NSLS crystal 16 has two sets of fits, the first for the full set of data and the second for a partial set of data, where the two outlying points were removed from the fit. If the partial fit is studied, it goes almost perfectly through all the included points; the divergence of the remaining two points is not understood, but these two points are within the stated uncertainty of the other points. Because of the near perfect fit to the majority of the PIMC values, the partial fit will be considered the better fit for NSLS crystal 16.

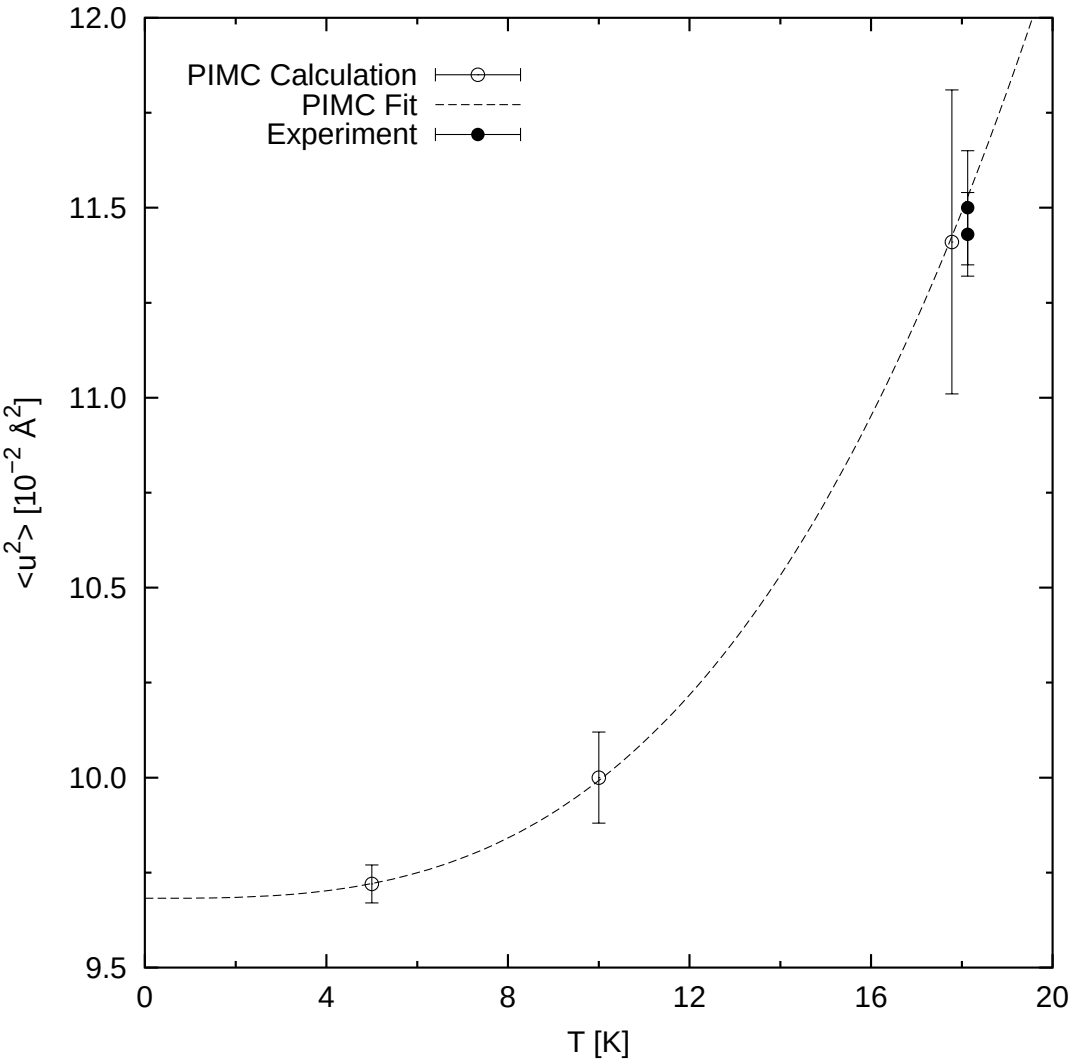

Figure 5.1: Comparison of $\langle u^2 \rangle$ values as calculated by PIMC for fcc ^{3}He at $V = 11.54$ cm^3 [23] to the measured value from NSLS crystal 4, which has a molar volume of 11.578 cm^3. The curve corresponds to a fit of the PIMC values to a $a + bT^3$ model. The computations below 18.0 K are done at a temperature corresponding to an hcp crystal in reality for this molar volume. The experimental values and their corresponding PIMC value agree quite well within error bars.

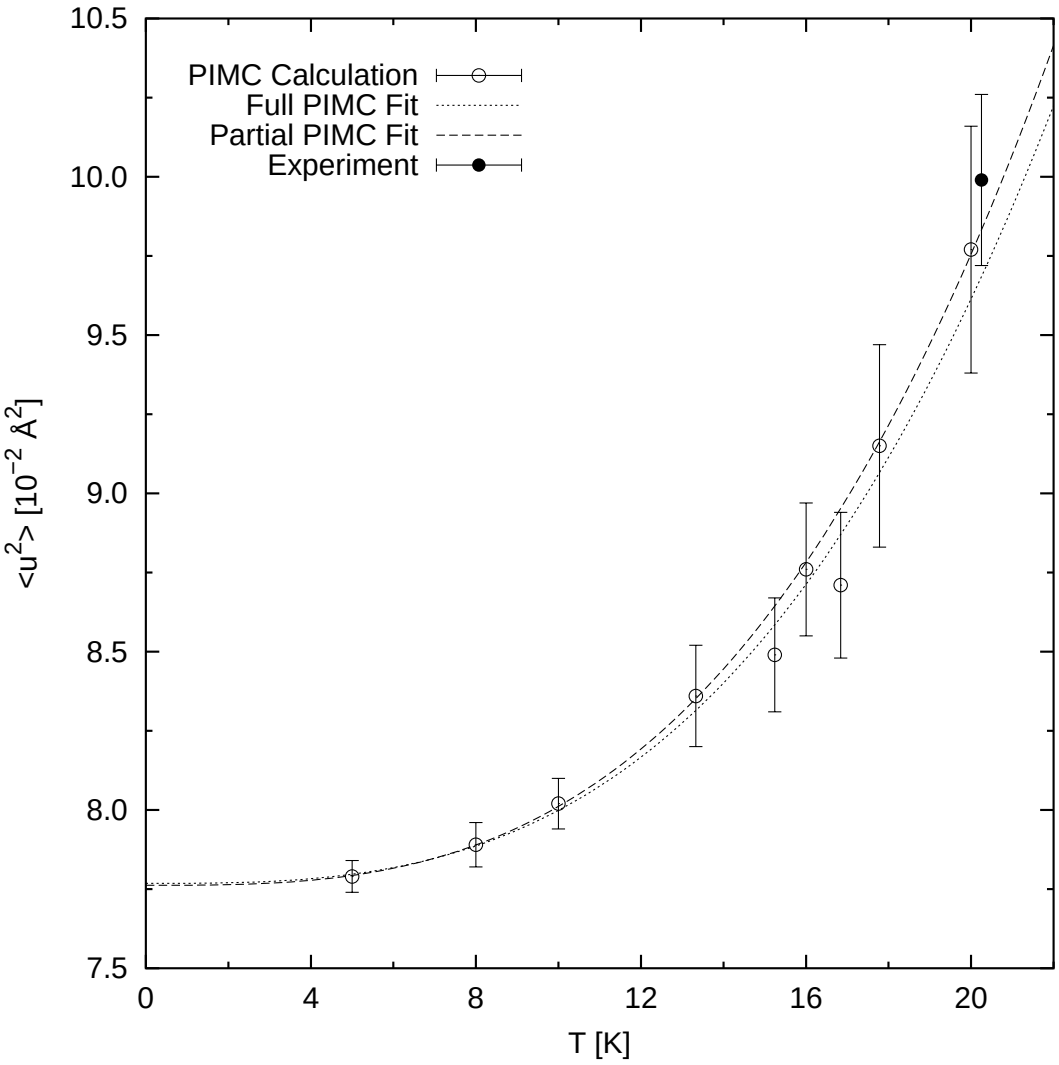

Figure 5.2: Comparison of $\langle u^2 \rangle$ values as calculated by PIMC for fcc ^{4}He at $V = 10.98$ cm^3 [23] to the measured value from NSLS crystal 16, which has a molar volume of 10.951 cm^3. The curves corresponds to fits of the PIMC values to a $a + bT^3$ model, with one fit being made to the full set of values and the other being made to a partial set of values (missing the two outlying points). The computations below 16.0 K are done at a temperature corresponding to an hcp crystal in reality for this molar volume. The experimental value and its corresponding PIMC value agree well within error bars.

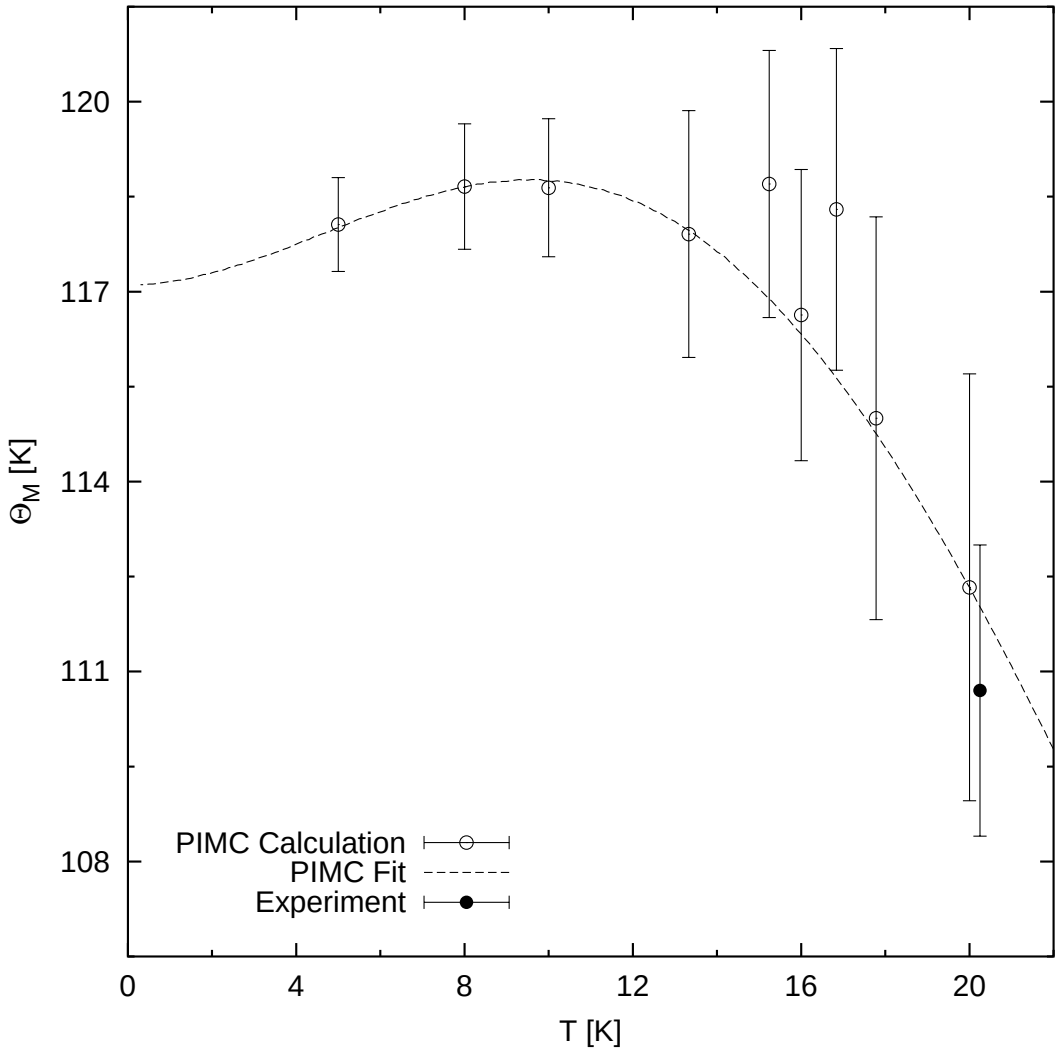

Figure 5.3: Comparison of Θ_M values as calculated by PIMC for fcc ^{4}He at $V = 10.98$ cm^3 [23] to the measured value from NSLS crystal 16, which has a molar volume of 10.951 cm^3. The values for the curve of the PIMC fit are values converted into Debye temperatures from a partial $\langle u^2 \rangle$ fit to a $a + bT^3$ model. The computations below 16.0 K are done at a temperature corresponding to an hcp crystal in reality for this molar volume. The experimental value and its corresponding PIMC value agree well within error bars.

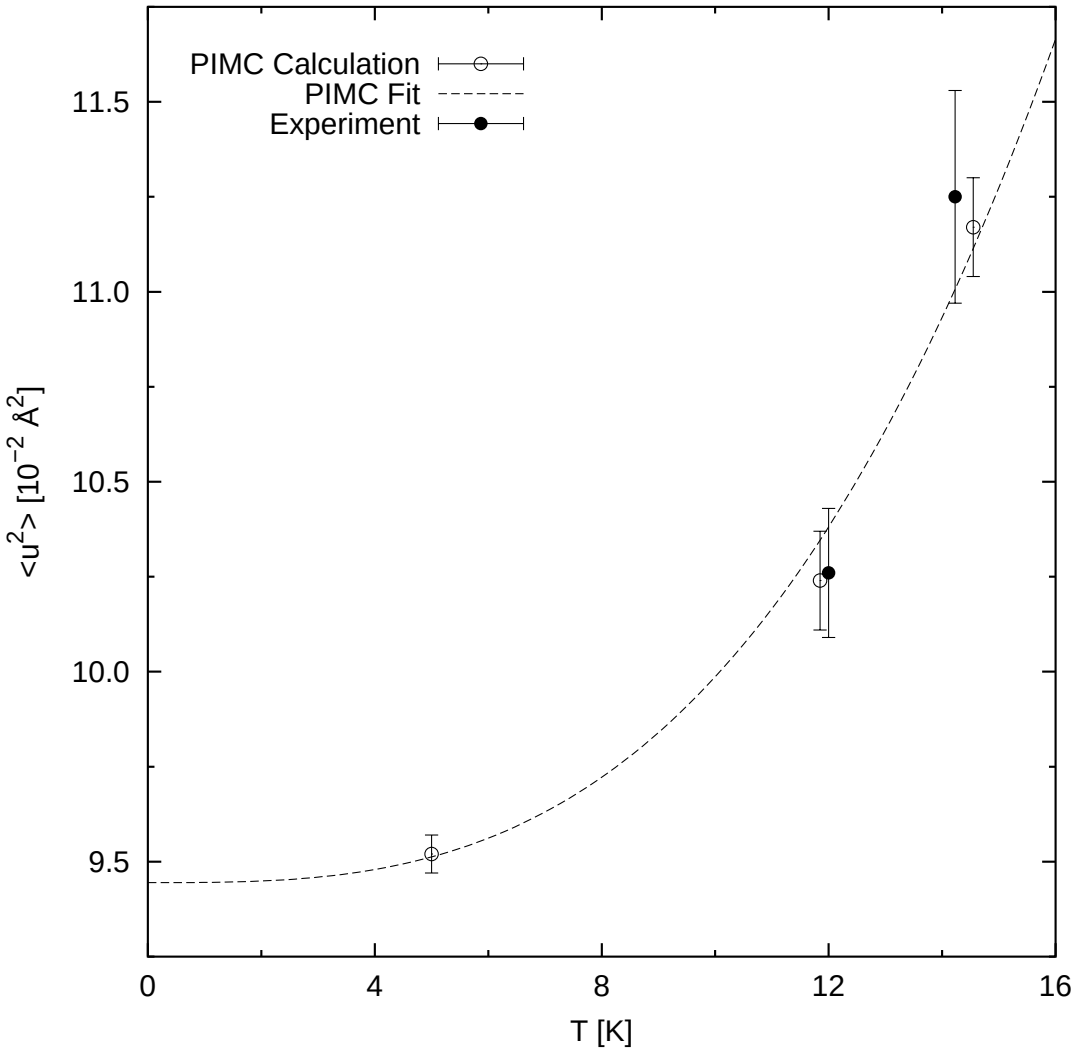

Figure 5.4: Comparison of $\langle u^2 \rangle$ values as calculated by PIMC for hcp ^{4}He at $V = 12.119$ cm^3 [23] to the measured values from NSLS crystal 18, which has molar volumes of 12.129 cm^3 for 12.00 K and 12.120 cm^3 for 14.23 K. The curve corresponds to a fit of the PIMC values to a $a + bT^3$ model. The experimental values and their corresponding PIMC values agree quite well within error bars.

If uncertainties are associated with the fit curves for the $\langle u^2 \rangle$ plots similar to the ones for the discrete PIMC values, the fits agree with the experimental values within the error bars. The partial fit curve for crystal 16 agrees better with the experimental value than the full fit curve.

Because of the many $\langle u^2 \rangle$ computations done for NSLS crystal 16, a graph of the resulting Debye temperatures is given in Fig. 5.3. The partial fit for the $\langle u^2 \rangle$ values was used to generate a Θ_M curve. This curve rises briefly then falls, as a function of temperature, and is used in Sec. 5.5 for comparison to all direct measurements, when they reduced to a single molar volume.

5.5 Comparisons

This section compares the values presented in this thesis with earlier measurements and extends comparisons with computations. In order to compare Θ_M values made at different temperatures and molar volumes, they can be adjusted to a common molar volume using the Grüneisen parameter presented in Eq. 5.2, so only a temperature dependence is left.

A graph of Θ_M versus V, where the values of Θ_M are calculated from all known direct measurements of $\langle u^2 \rangle$, is in Fig. 5.5. The measurements are at different temperatures, so direct comparison should not be made. A curve representing the predicted curvature of isothermal values for either helium isotope, from the measured Grüneisen parameter, is shown; it is shown going through the only two points taken at the same temperature, the ones by Stassis et al. [1].

The data are adjusted to common molar volume by use of the Grüneisen parameter, as described earlier, resulting in a graph of Θ_M versus T. It is worth noting that an analysis which converts $\langle u^2 \rangle$ values to equivalent Θ_M values is a highly sensitive way of displaying possible variations and trends in the direct data, so representing the data on a single graph can be illuminating. The graph, using a molar volume of 11.50 cm^3 as the reference, is shown in Fig. 5.6. This molar volume is a rough median value for the measurements presented in this thesis. The PIMC computational values shown are the six presented in Table 5.2. A curve for the ^{4}He PIMC Debye temperatures, derived from the partial PIMC fit to the NSLS crystal 16 $\langle u^2 \rangle$ values as shown in Fig. 5.2, is scaled to 11.50 cm^3 and shown. This curve is shown for both comparison and the fact that it shows the theoretical temperature dependence of the reduced values. There is an uncertainty associated with the curve, which is not shown.

From looking at the graph at the PIMC curve and ^{4}He measurements presented in this thesis,

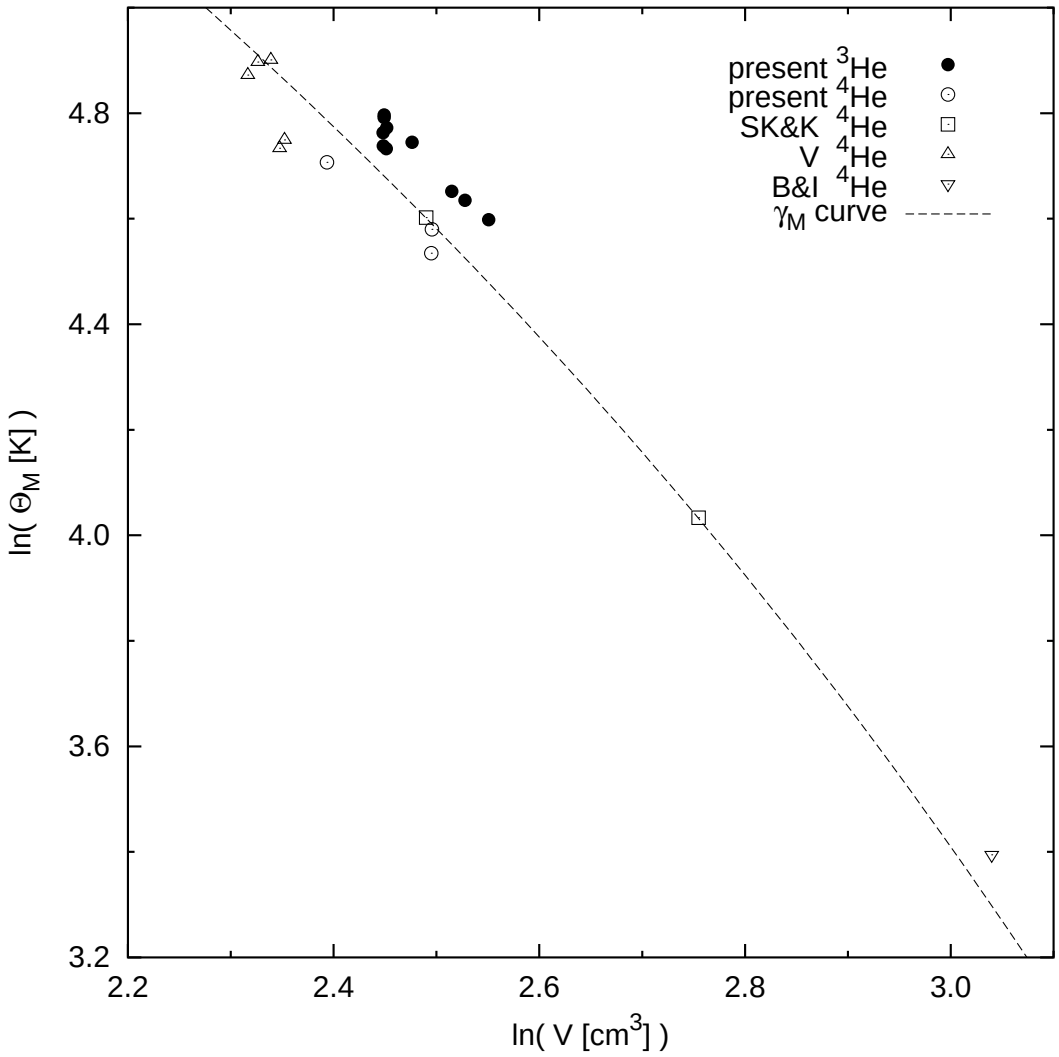

Figure 5.5: Natural logarithm of the Debye temperature versus natural logarithm of the molar volume for all known measurements of Θ_M for ^{3}He and ^{4}He. These data were taken at various temperatures, so direct comparison of them should not be done. Error bars are not shown, making the symbols clearer. The solid symbols represent ^{3}He values, while the open symbols represent ^{4}He values. The SK&K data are by Stassis et al. [1], the V data are by Venkataraman [3], and the B&I datum is by Burns and Isaacs [4]. The curve for the Grüneisen parameter, γ_M, is plotted to show the predicted relationship between the data if they were all taken at the same temperature.

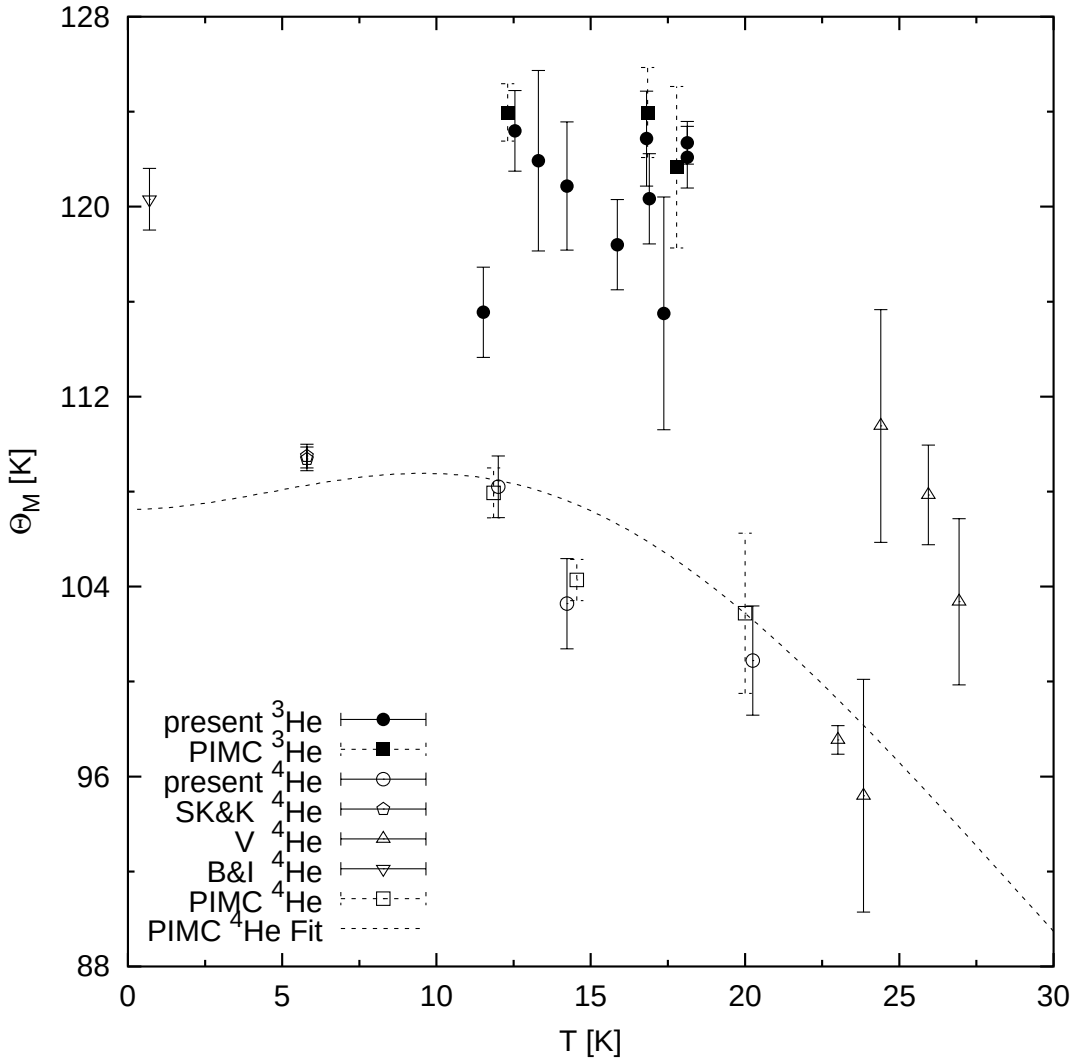

Figure 5.6: Debye temperature versus temperature of all experimental values, scaled to a molar volume of 11.50 cm^3 using the Grüneisen parameter. This molar volume is a rough median value for the measurements. The PIMC computational values shown are the six presented in Table 5.2. The PIMC fit for ^{4}He is the same as the one shown in Fig. 5.3, only scaled. As a guide to the phase of the experimental data points, those above 17.5 K correspond to fcc crystals, while those below correspond to hcp crystals.

the PIMC curve seems to have an offset making it slightly higher than the measurements. The three ^{4}He measurements decrease as a function of temperature, agreeing with the temperature dependence of the same region of the PIMC curve. If uncertainties similar to the ones shown for the PIMC values in Fig. 5.3 are applied to the PIMC curve, the curve agrees with the three ^{4}He measurements within the error bars, with the NSLS crystal 18 value at 14.23 K just barely agreeing.

If the ten ^{3}He measurements are considered, they have a decreasing temperature dependence, except for the NSLS crystal 3 value at 11.52 K and the two NSLS crystal 4 values at 18.13 K. This temperature dependence is similar to that of the PIMC curve. The crystal 3 value does not seem to fit with the rest very well, and is probably the most unreliable of the measurements presented.

The Burns and Isaacs datum does not agree very well with the PIMC curve or the neighboring experimental values. One possible explanation is that its molar volume is twice that of the reference volume, making the correction Eq. 5.2 applied to it the largest, although the molar volume is well in the range of the Grüneisen parameter used. Another is that the experiment, using a dilution refrigerator in a synchrotron beam, proved to be a physically difficult one to do [24].

If uncertainties similar to the ones shown for the PIMC values in Fig. 5.3 are applied to the PIMC curve, the data from Stassis et al. agree within error bars. A simple comparison of their measurements to the current measurements shows the same decreasing temperature dependence as before, although the PIMC curve in this region predicts an increasing temperature dependence.

If uncertainties are again applied to the PIMC curve, two of Venkataraman's five values agree with the curve, being those at 23.01 K and 24.40 K. The experiments that generated her data were the first successful work with essentially the same system used in this thesis. However, the growth of high quality samples and the methods of taking the data were not as developed at that time.

The T-dependent data can also be reduced to a molar volume of 11.50 cm^3, using the same Grüneisen parameter as before. This has been done for both sets of data, with the result that they both have a decreasing temperature dependence, which is in agreement with the corresponding regions of the PIMC curve.

5.6 Discussion

5.6.1 Temperature Dependence of the Debye Temperature

From Fig. 5.6, taking into account the preceding discussion of data inconsistencies, the temperature dependence of the measured Debye temperatures seems to be such that they decrease as the temperature increases, for both ^{3}He and ^{4}He. This is also evident in Tables 4.10–4.13, where each Θ_M value of the NSLS measurement sets 1A&B and 18A&B are at almost identical molar volumes and at different temperatures, with the Θ_M decreasing with temperature.

For a quasi-harmonic fcc crystal and a continuous n, the Debye moments of the distribution, $\omega_{\mathrm{D}}(n)$, compose a continuous curve that has a positive second derivative, with n at the minimum being between 0 and 2 [25]. From Eq. 2.68, it is seen that $\omega_{\mathrm{D}}(-1)$ determines the low temperature limit of Θ_M, while $\omega_{\mathrm{D}}(-2)$ determines the high limit. For this quasi-harmonic fcc crystal, $\omega_{\mathrm{D}}(-2)$ has a larger value than $\omega_{\mathrm{D}}(-1)$, making the high temperature limit of Θ_M larger than the low temperature limit. Also, this temperature dependence should be monotonic, with no local maxima or minima.

For a mildly anharmonic solid such as fcc neon, where the renormalized frequencies can be represented as a frequency shift from a quasi-harmonic model, the low temperature limit of Θ_M is smaller than the high temperature limit [26]. Also, the hcp solid with the closest c/a ratio to ideal is magnesium, and even its limiting cases for Θ_M have the same relationship as neon [27, 28]. The Debye moments used for neon and magnesium are derived from the one-phonon density of states obtained from a Born-von Kármán fit to measured phonon dispersion.

The behavior of the measured helium Θ_M values seems to run counter to this temperature dependence, at least locally. It is possible that the temperature dependence of Θ_M reverses itself at some point, increasing with temperature. However, due to the rather steep drop-off of Θ_M in the data measured, it is doubtful. Even if it did, it would not have approached its limit monotonically, still suggesting anharmonic effects. Since helium crystals of large molar volume melt at such a low temperature, the high temperature limit can never be measured. Increasing the pressure on the crystal in order to increase the melting temperature would diminish the anharmonic effects present in the helium, changing that which is interesting.

This backwards temperature dependence of Θ_M shown in this thesis is confirmed by PIMC

computations, and some evidence of this was seen by Venkataraman [3]. The conclusion one can draw from the reversed temperature dependence of Θ_M is that close-packed helium is so anharmonic that the one-phonon viewpoint of the vibrational excitations does not seem to be supported, causing this reversal. Currently, no quantitative values for multi-phonon contributions have been produced. Further theoretical and experimental work will be required for that.

Whether there is a local maximum to this temperature dependence at a low temperature, before Θ_M drops with temperature is unclear from the measured data. As seen on Fig. 5.6, the PIMC curve based upon the fit Eq. 5.4 predicts a maximum near 9 K. That PIMC fit to the computed $\langle u^2 \rangle$ values was an empirical one, and few low temperature points were used in the fit, so this maximum might not exist if enough computations were made.

5.6.2 Mass-Scaling of Phonon Frequencies

The ideal mass-scaling ratio for the Debye temperature at $T = 0$ is $\sqrt{4/3}$. The temperature dependence of the Debye temperature has a nontrivial dependence on mass due to the Debye integral, so at a finite temperature, a direct comparison is not strictly correct. Since the temperatures of the measurements are low, a qualitative comparison is made here.

If Fig. 5.6 is considered, the ^{3}He measurement values are roughly $\sqrt{4/3}$ times the ^{4}He measurement values. This makes the ideal mass-scaling factor reasonable for these data. However, the values do not disagree with the non-ideal mass-scaling values measured by others (as discussed in Sec. 5.3.3), since the error bars do not allow such a fine resolution.

5.6.3 Lindemann Ratio

One of the indicators used for determining the magnitude of the quantum nature of a crystal is the Lindemann ratio, $\sqrt{3\langle u^2 \rangle}/r$. The anharmonic nature of a crystal is directly linked to its quantum nature. For the ^{3}He measurements, this ratio ranged between 0.194 and 0.204, while for the ^{4}He measurements, it ranged between 0.182 and 0.190. Crystals with Lindemann ratios such as these are considered as having a large quantum nature. Direct comparisons between the two isotopes aren't possible since no measurements occur at the same volume and temperature for both. The best possible comparison is between NSLS 13 (^{3}He) and NSLS 18A (^{4}He), where both measurements were made at 14.23 K and the respective molar volumes are 12.365 and 12.120 cm^3. The resulting

Lindemann ratios are 0.2023 and 0.1902, a 6.2 percent difference that comes from ^{3}He having a smaller mass.

5.6.4 Anisotropic Effects

The measured data for hcp crystals were used to look for anisotropic effects. Unfortunately, no measurement had both pure a axis reflections and pure c axis reflections, which would have made a comparison easier. What was done instead was compare the reflections that were most weighted towards either axis. From these reflections, it was seen that the weighted reflections of one of the axes seemed to scatter randomly about a linear fit (made through all the data points), instead of all being on one side or the other. If there are any anisotropic effects in hcp He crystals (and there are probably some), they are too small to be resolved by these measurements.

5.6.5 Non-Gaussian Behavior of the Atomic Displacement

The data were used to look for non-Gaussian behavior in the atomic displacement, as evident in the modification of the Debye-Waller factor in Eq. 5.5, in an attempt to confirm the PIMC findings. Unfortunately, the simple plot used for the PIMC computations does not work with measurements, since I is measured, but not I_c. If a normal $\ln(I)$ versus Q^2 plot of the data is considered, the quadratic relation in Q^2 would appear as a noticeable curvature within the scatter of the points. However, this is not seen in the present data. It should be remembered that the data were analyzed using the assumption of a calculated free-atom form factor, which is the most strongly Q-dependent aspect of the data reduction.

References

[1] C. Stassis, D. Khatamian, and G. R. Kline, Solid State Commun. **25**, 531 (1978).

[2] G. L. Squires, in *Introduction to the Theory of Thermal Neutron Scattering* (Dover, New York, 1996), Chap. 3.

[3] C. T. Venkataraman, Ph.D. thesis, University of Illinois at Urbana-Champaign, 1996.

[4] C. A. Burns and E. D. Isaacs, Phys. Rev. B **55**, 5767 (1997).

[5] J. S. Dugdale and J. P. Franck, Proc. R. Soc. London, Ser. A **257**, 1 (1964).

[6] H. H. Sample and C. A. Swenson, Phys. Rev. **158**, 188 (1967).

[7] R. C. Pandorf and D. O. Edwards, Phys. Rev. **169**, 222 (1968).

[8] G. Ahlers, Phys. Rev. A **2**, 1505 (1970).

[9] W. R. Gardner, J. K. Hoffer, and N. E. Phillips, Phys. Rev. A **7**, 1029 (1973).

[10] R. A. Reese, S. K. Sinha, T. O. Brun, and C. R. Tilford, Phys. Rev. A **3**, 1688 (1971).

[11] V. J. Minkiewicz, T. A. Kitchens, G. Shirane, and E. B. Osgood, Phys. Rev. A **8**, 1513 (1973).

[12] J. Eckert, W. Thomlinson, and G. Shirane, Phys. Rev. B **16**, 1057 (1977).

[13] C. Stassis, G. Kline, W. Kamitakahara, and S. K. Sinha, Phys. Rev. B **17**, 1130 (1978).

[14] W. Thomlinson, J. Eckert, and G. Shirane, Phys. Rev. B **18**, 1120 (1978).

[15] J. Eckert, W. Thomlinson, and G. Shirane, Phys. Rev. B **18**, 3074 (1978).

[16] V. Ambegaokar, J. M. Conway, and G. Baym, J. Phys. Chem. Solids Suppl. **1**, 261 (1965).

[17] C. Seyfert, R. O. Simmons, H. Sinn, D. A. Arms, and E. Burkel, J. Phys.: Condens. Matter **11**, 3501 (1999).

[18] R. E. Slusher and C. M. Surko, Phys. Rev. B **13**, 1086 (1976).

[19] C. Seyfert, Ph.D. thesis, Universität Rostock, 1998.

[20] N. R. Werthamer, Solid State Commun. **9**, 2239 (1971).

[21] M. Järvinen and J. Soininen, Acta Crystallogr. Sect. A **43**, 694 (1987).

[22] D. M. Ceperley, Rev. Mod. Phys. **67**, 279 (1995).

[23] E. Draeger and D. M. Ceperley, Bull. Am. Phys. Soc. **44**, 655 (1999), to be published.

[24] C. A. Burns (private communication).

[25] T. H. K. Barron, A. J. Leadbetter, J. A. Morrison, and L. S. Salter, Acta Crystallogr. **20**, 125 (1966).

[26] J. A. Leake, W. B. Daniels, J. Skalyo, Jr., B. C. Frazier, and G. Shirane, Phys. Rev. **181**, 1251 (1969).

[27] R. Pynn and G. L. Squires, Proc. R. Soc. London, Ser. A **326**, 37 (1972).

[28] H. R. Schober and P. H. Dederichs, in *Metals: Phonon States, Electron States, and Fermi Surfaces*, Vol. 13a of *Landolt-Bornstein*, edited by K.-H. Hellwege and J. L. Olsen (Springer-Verlag, New York, 1981), p. 84.

Chapter 6

Conclusion

Debye-Waller factors for both ^{3}He and ^{4}He have been measured using X-rays. Analysis of the data provides values for the mean squared atomic deviation $\langle u^2 \rangle$. The ranges of molar volumes used for investigating ^{3}He and ^{4}He crystals were 11.52–12.82 cm^3 and 10.95–12.13 cm^3, respectively. The temperature ranges used were 11.5–18.2 K and 12.0–20.3 K, respectively. Data for both hcp and fcc phases were obtained.

The measured $\langle u^2 \rangle$ values agree quite well with path integral Monte Carlo computational values, provided those computations are extrapolated to infinite sample size.

Further analysis generates an equivalent Debye temperature, Θ_M. From the PIMC ^{4}He $\langle u^2 \rangle$ calculations, a fit was made, which was then used to generate a Θ_M curve. This curve, which has an maximum that may or may not actually exist, has a decreasing temperature dependence over the range of the measurements, and it agrees with the three measured ^{4}He values. The ^{3}He Θ_M measurements have a similar decreasing temperature dependence, with the exception of three of the ten values.

The ^{3}He and the ^{4}He measurements have roughly an ideal mass-scaling for the Debye temperatures of $\sqrt{4/3}$. Other techniques have been interpreted as showing possible slight deviations from $\sqrt{4/3}$, but such deviations may not be outside the respective experimental uncertainties.

Lindemann ratios measured for ^{3}He ranged between 0.194 and 0.204, while for ^{4}He they ranged between 0.182 and 0.190. For a pair of measurements done at comparable molar volumes and the same temperature, the Lindemann ratio for ^{3}He was found to be 6.2 percent larger than that of ^{4}He. The large values measured for the Lindemann ratios are consistent with the quantum nature of helium.

A temperature dependence of Θ_M was observed which is contrary to what is expected for an fcc quasi-harmonic crystal. An instance of this was seen by Venkataraman, who was unsure if it was real or due to an error. This inverted dependence is most likely due to the large anharmonic effects

present in low density helium, where the multi-phonon processes present in the crystal are being effectively ignored by the one-phonon model of the Debye temperature. Such contrary temperature dependence is also shown by a PIMC fcc model.

A future area of research could be to further investigate the reversed temperature dependence of the equivalent Debye temperature. Similar Debye-Waller measurements could be taken of helium at higher pressures, where helium is more classical. The temperature dependence can then be examined to see if it is reversed or not, where a higher temperature range of measurements can also be made (due to the higher melting temperature of helium crystals). A different, yet similar, type of measurement is to take Q-dependent Debye-Waller measurements of neon crystals, which have never been made, since neon is less quantum and solidifies in a convenient temperature range.

An investigation into whether a maximum in the Θ_M curve does indeed exist could be made. This would require measurements made at temperatures lower than those available to the equipment used for this thesis. Newer compression head refrigerators with better cooling power could be used, as could a dilution refrigerator made for use in a goniometer. More PIMC calculations should be done at these temperatures to see if the maximum was due to lack of enough data points.

Another possible experiment is a measurement of the Grüneisen parameter for Θ_M for helium. The Grüneisen parameter used in this thesis was the one measured for Θ_{C_V}. This newly measured γ_M could be compared to the existing γ_{C_V} to see if they agree. Since, in a one-phonon model, they are responsive to different moments of the frequency distribution, a comparison can possibly be used to better understand the underlying phonon excitations in quantum solid helium crystals.

Appendix A

Absorption Characteristics

Attenuation by a material is governed by

$$I = I_0 \, e^{-\mu x} \tag{A.1}$$

where I is the attenuated intensity, I_0 is the initial intensity, μ is the linear absorption coefficient for the material at a given energy, and x is the absorber's thickness.

The values of the linear absorption coefficients for the materials used as attenuators are given in Table A.1 for a photon energy of 16.00 keV. In the table, h is the thickness such that

$$\frac{I}{I_0} = \frac{1}{2} = e^{-\mu h} \, . \tag{A.2}$$

Table A.1: Linear Absorption Coefficients
Photon Energy is 16.00 keV

Material	$\mu[\text{cm}^{-1}]$	$h[\text{cm}]$
He (at STP)	3.8×10^{-5}	1.8×10^{4}
He (at 12 cm^3/mol)	7.1×10^{-2}	9.8×10^{0}
Be	4.85×10^{-1}	1.43×10^{0}
Al	1.749×10^{1}	3.963×10^{-2}
Mo	2.4055×10^{2}	2.882×10^{-3}
Cu	5.6098×10^{2}	1.236×10^{-3}

W. H. McMaster, N. Kerr Del Grande, J. H. Mallett, and J. H. Hubbell, Lawrence Livermore National Laboratory Report UCRL-50174 Section II Revision I, 1969.

Appendix B

General Crystal Properties

B.1 Crystal Lattices

These lattices are the bases of the crystal structures of He.

Assuming that the primitive cell vectors are $\mathbf{a}_1$, $\mathbf{a}_2$, and $\mathbf{a}_3$, the definition of the Euler angles are

$$\alpha \equiv \vartheta_{23}\,, \quad \beta \equiv \vartheta_{31}\,, \quad \text{and} \quad \gamma \equiv \vartheta_{12} \qquad \text{where} \qquad \cos(\vartheta_{ij}) = \frac{\mathbf{a}_i \cdot \mathbf{a}_j}{|\mathbf{a}_i||\mathbf{a}_j|}\,.$$

B.1.1 Cubic

$|\mathbf{a}_1| = |\mathbf{a}_2| = |\mathbf{a}_3| \equiv a \qquad \alpha = \beta = \gamma = 90^\circ$

Planar Spacing: $\qquad d_{hk\ell} = \dfrac{a}{\sqrt{h^2 + k^2 + \ell^2}}$

Cell Volume: $\qquad v = a^3$

B.1.2 Hexagonal

$|\mathbf{a}_1| = |\mathbf{a}_2| \equiv a \qquad |\mathbf{a}_3| \equiv c \qquad \alpha = \beta = 90^\circ \qquad \gamma = 120^\circ$

Planar Spacing: $\qquad \dfrac{1}{d_{hk\ell}^2} = \dfrac{4}{3}\left(\dfrac{h^2 + hk + k^2}{a^2}\right) + \dfrac{\ell^2}{c^2}$

Cell Volume: $\qquad v = \dfrac{\sqrt{3}}{2}\, a^2 c$

B.2 Crystal Structures

To convert an atomic volume from below into a molar volume, use

$$V = \left(0.6022045 \ \frac{\text{cm}^3}{\text{Å}^3}\right) v \qquad\qquad V \ [\text{cm}^3],\ v \ [\text{Å}^3]$$

where V is molar volume and v is atomic volume.

B.2.1 fcc

The fcc structure is one of the forms of both ^{3}He and ^{4}He.

This structure is actually a true Bravais lattice, but it is conventional to represent it in terms of a cubic lattice with a four atom basis, since the cubic lattice is much easier to deal with. Because of this, the "forbidden" peaks in the structure factor are not actually forbidden, but simply not there since the reciprocal lattice for fcc takes the form of a bcc lattice. If based on the cubic lattice, the atoms are at (0, 0, 0), ($\frac{1}{2}$, $\frac{1}{2}$, 0), ($\frac{1}{2}$, 0, $\frac{1}{2}$), and (0, $\frac{1}{2}$, $\frac{1}{2}$).

Atomic Volume: $v = \dfrac{a^3}{4}$

Nearest Neighbor Distance: $r = \dfrac{a}{\sqrt{2}}$

fcc Structure Factor:
$$\begin{cases} hk\ell \text{ all odd or all even} & F^2 = 4f^2 \\ hk\ell \text{ mixed} & F^2 = 0 \end{cases}$$

B.2.2 hcp

The hcp structure is one of the forms of both ^{3}He and ^{4}He, and is the form that Be takes.

This structure is a simple hexagonal lattice with a two atom basis. The atoms are at (0, 0, 0) and ($\frac{2}{3}$, $\frac{1}{3}$, $\frac{1}{2}$) within the unit cell.

Atomic Volume: $v = \dfrac{\sqrt{3}}{4}\, a^2 c$

Ideal c/a Ratio: $(c/a)_{\text{ideal}} = \sqrt{8/3} = 1.63299\ldots$

Nearest Neighbor Distance:
$$r = \begin{cases} a & \text{if} \quad c/a \geq \sqrt{8/3} \\ \sqrt{c^2/4 + a^2/3} & \text{if} \quad c/a < \sqrt{8/3} \end{cases}$$

hcp Structure Factor:
$$\begin{cases} h + 2k = 3n & \ell \text{ even} & F^2 = 4f^2 \\ h + 2k = 3n \pm 1 & \ell \text{ odd} & F^2 = 3f^2 \\ h + 2k = 3n \pm 1 & \ell \text{ even} & F^2 = f^2 \\ h + 2k = 3n & \ell \text{ odd} & F^2 = 0 \end{cases}$$

B.2.3 Wurtzite

The Wurtzite structure is the form that BeO takes.

This structure is a simple hexagonal lattice with a four atom basis, with two atoms being type A and the other two being type B. Within the unit cell, the A atoms are at (0, 0, 0) and ($\frac{2}{3}$, $\frac{1}{3}$, $\frac{1}{2}$), while the B atoms are at (0, 0, u) and ($\frac{2}{3}$, $\frac{1}{3}$, $\frac{1}{2} + u$).

This structure can be thought of as two hcp structures, one A and the other B, which have the same lattice parameters, and are superimposed on top of each other, except there is an offset of uc along the c-axis. Accordingly, the structure factor of Wurtzite has similarities to that of hcp.

Wurtzite Structure Factor ($W \equiv f_A^2 + 2f_A f_B \cos(2\pi u\ell) + f_B^2$):
$$\begin{cases} h + 2k = 3n & \ell \text{ even} & F^2 = 4W \\ h + 2k = 3n \pm 1 & \ell \text{ odd} & F^2 = 3W \\ h + 2k = 3n \pm 1 & \ell \text{ even} & F^2 = W \\ h + 2k = 3n & \ell \text{ odd} & F^2 = 0 \end{cases}$$

Appendix C

Be and BeO

The structure of beryllium and beryllium oxide is important in order to understand the majority of the background present. Table C.1 shows the structure and associated constants of both Be and BeO. Tables C.2 an C.3 show the predicted 2θ values for the important reflections of Be and BeO.

Table C.1: Be and BeO crystal characteristics

Crystal	Structure	a [Å]	c [Å]	u
Be	hcp	2.2856	3.5832	
BeO	Wurtzite	2.698	4.377	0.378

N. Schell, Ph.D. thesis, Ludwig-Maximilians-Universität, München, 1994.

Table C.2: Be reflections
Photon Energy is 16.00 keV

$hk\ell$	Q [Å^{-1}]	2θ [deg.]	$hk\ell$	Q [Å^{-1}]	2θ [deg.]
100	3.1743	22.576	104	7.6989	56.687
002	3.5070	24.979	203	8.2449	61.118
101	3.6264	25.844	210	8.3984	62.382
102	4.7303	33.919	211	8.5795	63.884
110	5.4981	39.637	114	8.9121	66.675
103	6.1441	44.528	212	9.1013	68.282
200	6.3486	46.094	105	9.3245	70.199
112	6.5213	47.424	204	9.4605	71.378
201	6.5863	47.926	300	9.5229	71.922
004	7.0140	51.256	213	9.9099	75.338
202	7.2529	53.135	302	10.148	77.480

Table C.3: BeO reflections
Photon Energy is 16.00 keV

$hk\ell$	Q [Å^{-1}]	2θ [deg.]
100	2.689	19.09
002	2.871	20.39
101	3.048	21.67
102	3.934	28.08
110	4.658	33.38
103	5.077	36.49

Appendix D

He Properties

D.1 Form Factor

There are no measured data for the atomic form factor of helium, so calculated values have to be used. Calculated data are fit to twelve parameters, according to

$$f(Q) = \sum_{i=1}^{6} a_i \, e^{-b_i (Q/4\pi)^2} \qquad\qquad Q\,[\text{Å}^{-1}]\,. \tag{D.1}$$

The values of the parameters for He for the Q range $0 \leq Q \leq 25$ are given in Table D.1.

Table D.1: He Form Factor Parameters

i	a_i	b_i
1	0.69475	5.83366
2	0.62068	12.87682
3	0.38661	2.53296
4	0.15223	28.16171
5	0.12661	0.97507
6	0.01907	0.25308

Z. Su and P. Coppens, Acta Cryst. A **53**, 749 (1997).

D.2 Thermodynamic Relations

The melting curve of helium has been the subject of several measurements. Fits have been made for several quantities using the data. The relationship used to fit the melting pressure, P_m, to the temperature, T, is the Simon equation,

$$P_m = a + bT_m{}^c \qquad\qquad P_m\,[\text{MPa}] \quad T_m\,[\text{K}]\,. \tag{D.2}$$

The values of the parameters used in this equation for He are given in Table D.2. The relationship used to fit the molar volume of the fluid, V_f, to the melting pressure, P_m, is

$$V_f = d' + b'(P_m + a')^{c'} \qquad\qquad V_f\,[\text{cm}^3/\text{mol}] \quad P_m\,[\text{MPa}]\,. \tag{D.3}$$

The values of the parameters used in this equation for He are given in Table D.3. The relationship used to fit the change in the molar volume due to melting, ΔV_m, to the melting pressure, P_m, is

$$\Delta V_m = A - B\log(P_m + C) \qquad\qquad \Delta V_m\,[\text{cm}^3/\text{mol}] \quad P_m\,[\text{MPa}]\,. \tag{D.4}$$

The values of the parameters used in this equation for He are given in Table D.4. From Eqs. D.3 and D.4, the bulk molar volume of the solid can be obtained along the melting curve.

The hcp-fcc-fluid triple point for both He isotopes have been measured, as well as the hcp-fcc transition. An approximate linear relation can be formed for the transition's lower pressures,

$$P_{tr} = A' + B'(T - C') \qquad\qquad P_{tr}\,[\text{MPa}] \quad T_m\,[\text{K}]\,. \tag{D.5}$$

The values for the triple point and the fit parameters are listed in Table D.5.

Table D.2: Parameters for the P_m–T Fit

Isotope	P_m range	a	b	c
^{3}He	7.5–343 [a]	2.467	1.969372	1.517083
^{4}He	3.6–343 [a]	−1.746	1.697979	1.555414
^{4}He	100–1000 [b]	−3.186	1.783518	1.54171

[a] R. L. Mills and E. R. Grilly, Phys. Rev. **99**, 480 (1955).

[b] R. K. Crawford and W. B. Daniels, J. Chem. Phys. **55**, 5651 (1971).

Table D.3: Parameters for the V_f–P_m Fit

Isotope	P_m range	a'	b'	c'	d'
^{3}He	4.9–349	0.1054	35.1242	−0.161532	−3.2482
^{4}He	3.4–349	1.4567	37.8289	−0.107253	−10.0712

E. R. Grilly and R. L. Mills, Ann. Phys. (N. Y.) **8**, 1 (1959).

Table D.4: Parameters for the ΔV_m–P_m Fit

Isotope	P_m range	A	B	C
^{3}He	14.3–349	1.19967	0.30825	−4.1758
^{4}He	17.2–349	1.26955	0.33439	−10.125

E. R. Grilly and R. L. Mills, Ann. Phys. (N. Y.) **8**, 1 (1959).

Table D.5: He hcp-fcc Transition Values

	Fluid Triple Point		Fit Parameters		
Isotope	T [K]	P [MPa]	A'	B'	C'
^{3}He	17.8	158.0	156.0	61.7	17.65[a]
^{4}He	14.9	111.6	174.5	55.0	15.8[b]

[a] M. G. Ryschkewitsch, J. P. Franck, B. J. Duch, and W. B. Daniels, Phys. Rev. B **26**, 5276 (1982).

[b] J. P. Franck, Phys. Rev. B **22**, 4315 (1980).

D.3 Mass

The atomic mass of helium, m, is needed to calculate equivalent Debye temperature. It is given in atomic mass units (amu), where

$$1 \text{ amu} = 1.660565(86) \times 10^{-24} \text{ g}. \tag{D.6}$$

The values for m are given for both helium isotopes in Table D.6.

Table D.6: He Isotope Masses

Isotope	m [amu]
^{3}He	3.0160293
^{4}He	4.0026032

Appendix E

hcp Elemental Crystals

This section presents previously measured properties of various elemental hcp crystals at 295 K. Table E.1 contains values for $\langle u^2 \rangle$ in the form of

$$B_a \equiv 8\pi^2 \langle {u_a}^2 \rangle \qquad \text{and} \qquad B_c \equiv 8\pi^2 \langle {u_c}^2 \rangle \,. \tag{E.1}$$

Fig. E.1 is a graph of $\langle {u_c}^2 \rangle / \langle {u_a}^2 \rangle$ versus c/a, with a circle marking the c/a value of 1.6310 for He.

Table E.1: hcp Elemental Crystals

Element	B_a [Å^2] [a]	B_c [Å^2] [a]	c/a ratio [b]
Be	0.599	0.541	1.568
Dy	0.81	0.89	1.5370
Er	0.57	0.73	1.5700
Gd	0.80	0.88	1.5904
Ho	0.96	0.97	1.5698
Lu	0.86	0.97	1.5846
Mg	1.34	1.58	1.6235
Sc	0.72	0.73	1.5936
Tb	0.67	0.71	1.5811
Y	0.83	0.80	1.5712
Zn	0.82	2.04	1.8563

[a] N. G. Krishna and D. B. Sirdeshmukh, Acta Crystallogr. Sect. A **54**, 513 (1998).

[b] W. B. Pearson, *Handbook of Lattice Spacings and Structures of Metals* (Pergamon, New York, 1967), Vol. 2.

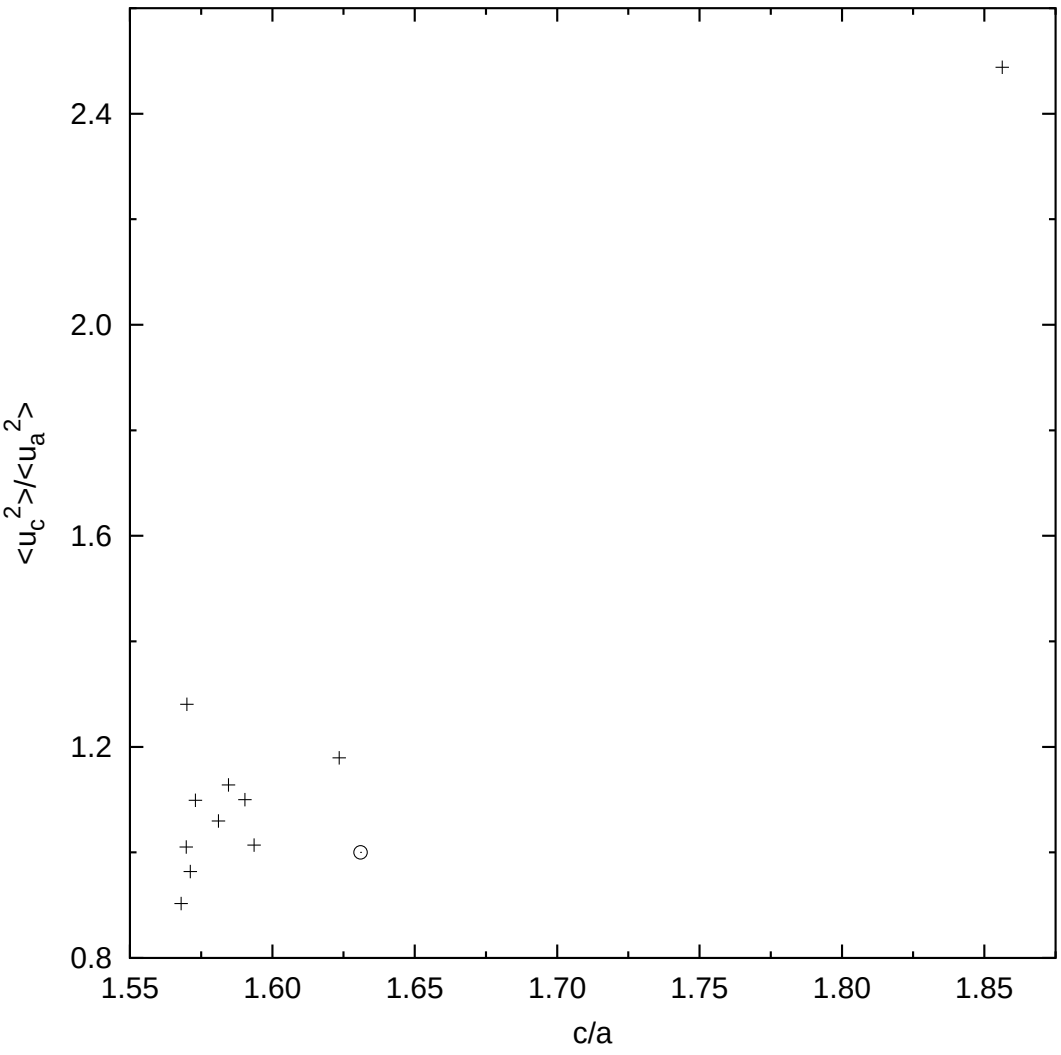

Figure E.1: A graph of $\langle {u_c}^2 \rangle / \langle {u_a}^2 \rangle$ versus c/a, for various hcp elemental crystals. The circle represents a c/a ratio of 1.6310 for He and a $\langle {u_c}^2 \rangle / \langle {u_a}^2 \rangle$ of 1.

Appendix F

Debye-Waller Data

This appendix contains all the Debye-Waller data discussed in this thesis.

The Q-dependent data presented here show the raw values of the integrated intensities of the scans, along with the corrections applied to them. The value I_{raw} corresponds to the raw integrated intensity, with only the deadtime correction, the monitor correction, the form factor multiplier from the structure factor, and the attenuator absorption correction applied to it. The value I_{final} comes from dividing I_{raw} by the squared form factor (f^2), and the Lorentz polarization factor (L). For the APS 1998 data, the volume correction for a small beam (C_{S}), as described in Section 4.1.6, is also divided out.

The T-dependent data presented here only show the final intensity. The intensity is corrected for the deadtime, the monitor reading, the form factor, and the Lorentz polarization factor. Since the same attenuator was used for all scans in a set, correcting for it was unnecessary. In practice, since the 2θ angle of the reflection will not change very much as the temperature is changed (the molar volume does not change very much with small temperature changes), the form factor and Lorentz factor corrections will not vary that much. For all the data presented here, exclusion of these corrections did not change the resultant data at all, within the precision used.

Table F.1: NSLS 1996 Q-dependent Measurement 1 A

$hk\ell$	Q [Å^{-1}]	I_{raw}	$f^2(Q)$	$L(\theta)$	I_{final}
100	2.4117	1.7559×10^3	2.2316	3.3999	2.3144×10^2
110	4.1788	1.1874×10^2	0.8931	2.0082	6.6204×10^1
200	4.8260	3.6360×10^1	0.6135	1.7599	3.3675×10^1
201	4.9927	1.5678×10^1	0.5562	1.7070	1.6512×10^1
210	6.3829	7.7625×10^{-1}	0.2442	1.3819	2.3003×10^0
211	6.5106	8.6144×10^{-1}	0.2265	1.3598	2.7967×10^0
300	7.2362	1.8577×10^{-1}	0.1484	1.2521	1.0000×10^0

Table F.2: NSLS 1996 Q-dependent Measurement 1 B

$hk\ell$	Q [Å^{-1}]	I_{raw}	$f^2(Q)$	$L(\theta)$	I_{final}
100	2.4123	1.5758×10^3	2.2311	3.3991	2.0778×10^2
110	4.1794	1.0746×10^2	0.8928	2.0079	5.9942×10^1
200	4.8261	2.5484×10^1	0.6135	1.7599	2.3603×10^1
201	4.9918	2.3197×10^1	0.5565	1.7072	2.4416×10^1
210	6.3832	1.2279×10^0	0.2442	1.3818	3.6394×10^0
211	6.5104	9.2023×10^{-1}	0.2266	1.3599	2.9870×10^0
300	7.2365	1.8573×10^{-1}	0.1483	1.2521	1.0000×10^0

Table F.3: NSLS 1996 Q-dependent Measurement 3

$hk\ell$	Q [Å^{-1}]	I_{raw}	$f^2(Q)$	$L(\theta)$	I_{final}
100	2.4120	1.6496×10^3	2.2313	3.3995	2.1748×10^2
101	2.7303	9.6757×10^2	1.9281	3.0127	1.6657×10^2
102	3.5170	2.9026×10^2	1.2907	2.3617	9.5221×10^1
200	4.8216	3.1862×10^1	0.6151	1.7613	2.9409×10^1
112	4.8982	2.6216×10^1	0.5881	1.7365	2.5673×10^1
201	4.9880	1.7919×10^1	0.5578	1.7084	1.8805×10^1
202	5.4581	9.2089×10^0	0.4223	1.5776	1.3824×10^1
203	6.1630	2.0918×10^0	0.2781	1.4224	5.2890×10^0
212	6.8723	3.8302×10^{-1}	0.1833	1.3026	1.6043×10^0
204	7.0318	3.7362×10^{-1}	0.1670	1.2797	1.7481×10^0
300	7.2311	1.8642×10^{-1}	0.1488	1.2528	1.0000×10^0

Table F.4: NSLS 1996 Q-dependent Measurement 4 A

$hk\ell$	Q [Å^{-1}]	I_{raw}	$f^2(Q)$	$L(\theta)$	I_{final}
111	2.5584	2.4941×10^3	2.0892	3.2094	3.7197×10^2
200	2.9547	1.5441×10^3	1.7285	2.7909	3.2008×10^2
220	4.1794	2.0943×10^2	0.8928	2.0079	1.1683×10^2
311	4.8997	5.7792×10^1	0.5875	1.7360	5.6664×10^1
222	5.1184	3.5086×10^1	0.5164	1.6695	4.0696×10^1
420	6.6079	1.7849×10^0	0.2139	1.3437	6.2091×10^0
422	7.2382	3.5362×10^{-1}	0.1482	1.2518	1.9062×10^0
511	7.6769	1.3812×10^{-1}	0.1152	1.1991	1.0000×10^0
333	7.6779	1.4135×10^{-1}	0.1151	1.1990	1.0240×10^0

Table F.5: NSLS 1996 Q-dependent Measurement 4 B

$hk\ell$	Q [Å^{-1}]	I_{raw}	$f^2(Q)$	$L(\theta)$	I_{final}
220	4.1794	2.1767×10^2	0.8928	2.0079	1.2143×10^2
311	4.8997	5.2924×10^1	0.5875	1.7360	5.1890×10^1
222	5.1184	3.5150×10^1	0.5164	1.6695	4.0771×10^1
420	6.6079	1.7016×10^0	0.2139	1.3437	5.9193×10^0
422	7.2382	3.4555×10^{-1}	0.1482	1.2518	1.8627×10^0
511	7.6769	1.4054×10^{-1}	0.1152	1.1991	1.0175×10^0
333	7.6780	1.3803×10^{-1}	0.1151	1.1990	1.0000×10^0

Table F.6: NSLS 1996 Q-dependent Measurement 12

$hk\ell$	Q [Å^{-1}]	I_{raw}	$f^2(Q)$	$L(\theta)$	I_{final}
100	2.3889	1.2207×10^4	2.2541	3.4317	1.5781×10^3
101	2.7066	8.1869×10^3	1.9499	3.0384	1.3818×10^3
110	4.1404	7.8246×10^2	0.9129	2.0255	4.2317×10^2
200	4.7793	2.6647×10^2	0.6306	1.7754	2.3802×10^2
201	4.9442	1.6816×10^2	0.5723	1.7220	1.7063×10^2
202	5.4118	8.6198×10^1	0.4340	1.5894	1.2495×10^2
210	6.3236	8.4953×10^0	0.2529	1.3925	2.4124×10^1
211	6.4493	8.4536×10^0	0.2348	1.3703	2.6271×10^1
300	7.1694	9.5847×10^{-1}	0.1542	1.2609	4.9293×10^0
302	7.6050	5.3896×10^{-1}	0.1200	1.2072	3.7201×10^0
220	8.2786	9.3398×10^{-2}	0.0820	1.1390	1.0000×10^0

Table F.7: NSLS 1996 Q-dependent Measurement 13

$hk\ell$	Q [Å^{-1}]	I_{raw}	$f^2(Q)$	$L(\theta)$	I_{final}
100	2.3583	4.2722×10^3	2.2843	3.4751	5.3818×10^2
101	2.6711	2.6120×10^3	1.9828	3.0776	4.2803×10^2
110	4.0893	2.1933×10^2	0.9398	2.0490	1.1390×10^2
200	4.7181	8.5191×10^1	0.6536	1.7963	7.2558×10^1
201	4.8826	5.4192×10^1	0.5935	1.7415	5.2436×10^1
202	5.3427	2.5834×10^1	0.4522	1.6074	3.5542×10^1
203	6.0329	5.3424×10^0	0.3003	1.4480	1.2286×10^1
210	6.2407	2.2419×10^0	0.2656	1.4077	5.9969×10^0
211	6.3645	2.1756×10^0	0.2469	1.3851	6.3626×10^0
300	7.0768	2.3830×10^{-1}	0.1627	1.2734	1.1501×10^0
302	7.5100	1.5437×10^{-1}	0.1267	1.2182	1.0000×10^0

Table F.8: NSLS 1996 Q-dependent Measurement 15

$hk\ell$	Q [Å^{-1}]	I_{raw}	$f^2(Q)$	$L(\theta)$	I_{final}
100	2.3337	2.7803×10^3	2.3088	3.5110	3.4298×10^2
200	4.6629	4.9492×10^1	0.6751	1.8156	4.0379×10^1
201	4.8274	3.0026×10^1	0.6130	1.7594	2.7839×10^1
300	6.9945	2.1931×10^{-1}	0.1707	1.2849	1.0000×10^0

Table F.9: NSLS 1996 Q-dependent Measurement 16

$hk\ell$	Q [Å^{-1}]	I_{raw}	$f^2(Q)$	$L(\theta)$	I_{final}
111	2.6099	1.2145×10^{3}	2.0402	3.1478	1.8910×10^{2}
220	4.2574	1.4504×10^{2}	0.8538	1.9738	8.6067×10^{1}
131	4.9943	3.9636×10^{1}	0.5557	1.7065	4.1798×10^{1}
222	5.2148	1.9932×10^{1}	0.4878	1.6421	2.4884×10^{1}
240	6.7314	1.5377×10^{0}	0.1990	1.3240	5.8362×10^{0}
242	7.3724	2.8158×10^{-1}	0.1372	1.2348	1.6626×10^{0}
242	7.3730	2.7061×10^{-1}	0.1371	1.2347	1.5984×10^{0}
242	7.3738	3.1884×10^{-1}	0.1370	1.2346	1.8844×10^{0}
333	7.8214	1.2556×10^{-1}	0.1061	1.1834	1.0000×10^{0}
333	7.8214	1.3426×10^{-1}	0.1061	1.1834	1.0694×10^{0}

Table F.10: NSLS 1996 Q-dependent Measurement 18 A

$hk\ell$	Q [Å^{-1}]	I_{raw}	$f^2(Q)$	$L(\theta)$	I_{final}
100	2.3781	1.5718×10^{3}	2.2647	3.4469	2.0135×10^{2}
$10\bar{1}$	2.6901	1.0710×10^{3}	1.9652	3.0565	1.7830×10^{2}
110	4.1145	9.6723×10^{1}	0.9264	2.0373	5.1245×10^{1}
$11\bar{2}$	4.8261	3.1184×10^{1}	0.6135	1.7599	2.8882×10^{1}
210	6.2844	1.2839×10^{0}	0.2588	1.3996	3.5444×10^{0}
211	6.4097	1.2625×10^{0}	0.2404	1.3772	3.8138×10^{0}
$21\bar{3}$	7.3353	1.7367×10^{-1}	0.1401	1.2394	1.0000×10^{0}

Table F.11: NSLS 1996 Q-dependent Measurement 18 B

$hk\ell$	Q [Å^{-1}]	I_{raw}	$f^2(Q)$	$L(\theta)$	I_{final}
100	2.3779	1.0195×10^{3}	2.2650	3.4472	1.3058×10^{2}
$10\bar{1}$	2.6892	7.2497×10^{2}	1.9660	3.0575	1.2061×10^{2}
110	4.1145	7.3894×10^{1}	0.9264	2.0373	3.9151×10^{1}
$11\bar{2}$	4.8249	2.5114×10^{1}	0.6139	1.7602	2.3240×10^{1}
210	6.2838	1.3454×10^{0}	0.2589	1.3997	3.7128×10^{0}
211	6.4091	1.2070×10^{0}	0.2405	1.3773	3.6447×10^{0}
$21\bar{3}$	7.3341	1.7381×10^{-1}	0.1402	1.2396	1.0000×10^{0}

Table F.12: NSLS 1996 T-dependent Measurement 3

T [K] ($\pm$0.01)	I	T [K] ($\pm$0.01)	I
11.91	1.5996	14.82	1.2539
11.93	1.5856	14.83	1.2507
12.89	1.4617	15.89	1.1119
13.83	1.3558	15.90	1.1211
13.84	1.3522	16.83	1.0000

Table F.13: NSLS 1996 T-dependent Measurement 18

T [K] ($\pm$0.01)	I	T [K] ($\pm$0.01)	I
12.00	1.4780	13.45	1.1707
12.29	1.4137	13.46	1.1791
12.55	1.3630	13.69	1.0977
12.97	1.2764	13.92	1.0644
12.99	1.2718	14.16	1.0306
13.19	1.2405	14.40	1.0000

Table F.14: APS 1998 Q-dependent Measurement 5

$hk\ell$	Q [Å^{-1}]	I_{raw}	$f^2(Q)$	$L(\theta)$	$C_{\text{S}}(\omega,\chi)$	I_{final}
100	2.3491	2.4157×10^{3}	2.2935	3.4885	1.0000	3.0193×10^{2}
200	4.6987	5.2988×10^{1}	0.6611	1.8030	1.0001	4.4453×10^{1}
300	7.0479	2.1141×10^{-1}	0.1655	1.2774	1.0001	1.0000×10^{0}

Table F.15: APS 1998 Q-dependent Measurement 12

$hk\ell$	Q [Å^{-1}]	I_{raw}	$f^2(Q)$	$L(\theta)$	$C_{\text{S}}(\omega,\chi)$	I_{final}
002	2.5586	4.8799×10^4	2.0891	3.2093	1.0061	7.2346×10^3
102	3.5163	1.6050×10^4	1.2912	2.3621	1.0004	5.2603×10^3
103	4.5324	3.4292×10^3	0.7284	1.8632	1.0000	2.5266×10^3
112	4.8954	1.5459×10^3	0.5890	1.7374	1.0023	1.5072×10^3
004	5.1185	1.4053×10^3	0.5164	1.6695	1.0194	1.5992×10^3
202	5.4563	5.5779×10^2	0.4227	1.5781	1.0068	8.3046×10^2
104	5.6571	4.2591×10^2	0.3753	1.5294	1.0010	7.4138×10^2
114	6.6046	5.1157×10^1	0.2144	1.3442	1.0000	1.7754×10^2
105	6.8371	3.2672×10^1	0.1871	1.3079	1.0039	1.3302×10^2
213	7.4412	6.4570×10^0	0.1318	1.2264	1.0008	3.9908×10^1
006	7.6779	6.1962×10^0	0.1151	1.1990	1.0409	4.3124×10^1
205	8.0098	1.8502×10^0	0.0954	1.1642	1.0005	1.6657×10^1
$\bar{1}16$	8.0476	1.8320×10^0	0.0934	1.1605	1.0254	1.6490×10^1
214	8.1766	8.3098×10^{-1}	0.0868	1.1483	1.0012	8.3251×10^0
116	8.7379	2.6929×10^{-1}	0.0636	1.1015	1.0014	3.8409×10^0
304	8.8592	1.4185×10^{-1}	0.0595	1.0927	1.0155	2.1496×10^0
215	9.0319	1.0333×10^{-1}	0.0541	1.0809	1.0009	1.7647×10^0
107	9.2774	5.1306×10^{-2}	0.0474	1.0656	1.0160	1.0000×10^0

Appendix G

Procedures

This appendix contains detailed accounts of the procedures used during the experiment. The procedures are in the preferred chronological order.

G.1 Beamline Alignment

The optics of the beamline are set up by the beamline personnel. They set the energy of the photons and focus the beam on the position intended to be the center of the diffractometer's rotation. What is left to align is everything in the experimental hutch, such as the diffractometer, the slits, and the ionization chambers.

One of the tools needed for this job is "burn paper", which is a paper with a special coating that changes color where X-rays strike it. Another helpful tool is the use of CCD cameras in conjunction with a fluorescent screen, since the screen glows when struck with X-rays, allowing someone see where the beam is in real time.

Once the optics are set up correctly, the diffractometer needs to be aligned first. This is with the normal assumption that the diffractometer circles are aligned with respect to one another already; if they aren't, the manufacturer usually has to do this. The first thing to do is to make sure that the diffractometer is perpendicular to the beam (see Fig. 3.6). This is best achieved by using the 2θ arm and burn paper. The arm is set to 180° and a burn is taken. Then the arm is set to 0°, with another burn being taken. The distance horizontally between marks should be zero, and if it is not, one can twist the diffractometer until it is.

The next thing to do is make the beam pass through the center of rotation of the diffractometer. A specially made metal pin is mounted onto the ϕ circle and is watched through a telescope that is part of the diffractometer. The pin is rotated in χ while periodically adjusting the height of the pin until the tip is the center of rotation. Once this is done, the X-ray beam is let into the hutch

and is centered by either moving the diffractometer or steering the beam using the beamline optics. Burn paper is used to check the positioning, with the final result being that the beam is centered on the tip of the pin.

At this point, the slits are put into the path of the beam. They are closed down until the desired size of the beam is achieved, keeping the center of the beam at the pin's tip. The ionization chambers are also put into the beam path; they are fairly simple to align since the windows are so large.

The software positions of the motors ω, χ, and ϕ need to be set in the software. For the 0° position of ω, the χ circle needs to be vertical, which can be checked with a level. For the 90° position of χ, the ϕ stage needs to be horizontal, which can again be checked with a level. The value of ϕ is completely arbitrary, and is set to be exactly the counter value.

Setting the software value of 2θ is more crucial that that of the other motors, since its value determines the planar spacing of a reflection. The first thing is to mount the scatter slit, the flight tube, and a pair of motorized slits onto the 2θ arm. A PIN diode detector is mounted behind the slits, which are set wide open. The PIN diode is able to take the full intensity of the incident beam without being harmed. The 2θ arm is then put into the horizontal orientation, with burn paper mounted onto the front of the scatter slits. The beam shutter is opened, creating a mark on the burn paper. Ideally, the mark is at the vertical center of the scatter slit. If it isn't, the 2θ position is moved in the direction that would accomplish this, followed by another burn. This is repeated until the mark is at the center of the scatter slit. At this point the detector should register counts from the beam striking it. This centered position is set as zero for the 2θ software value. Each slit pair is then centered about this position by finding the zero position of each slit blade; this is done by noting the full count rate with the slits wide open, moving one blade inward until the rate is exactly one half, setting that position in the software to zero, moving it back out again, and then doing the same for the other blade. After this is done, the slits are only moved such that both blades move at the same time and in opposite directions; the slit pairs will either open or close, keeping the center constant.

The next thing to do is to mount the Displex onto the ϕ circle. None of the radiation shields are attached at this point, leaving the sample cell in plain sight. Now the sample cell has to be centered within the ϕ circle. While rotating the Displex in ϕ, the cell is watched through the

telescope to see if it stays at the same position, or if it moves back and forth, being out of center in the ϕ circle. If the cell is out of center, the x-y stage on the Displex is adjusted until the cell's position does not move as the Displex is rotated.

The last thing to do is to set the lengthwise center of the cell to the beam position. This is checked by mounting burn paper on the cell, and exposing it to the X-ray beam. To move the cell, the stage's z position is changed.

G.2 Gas System Preparation

G.2.1 Strain Gauge Cell Calibration

Before the sample gas is prepared, the strain gauge cell (SGC) needs to be calibrated. The strain gauges mounted on the cell are assembled into a Wheatstone bridge and a voltage is applied to both ends of the bridge. There is a potential difference across the bridge which changes as the strain in the cell increases due to increased gas pressure in the cell. The relation between voltage and pressure is linear, where the correspondence constant is arbitrary. Strain is inherent in the bridge due to the gauges being mounted onto a cylinder's curved surface, resulting in a constant component to the pressure-voltage relationship.

The way to find the parameter values of the linear relationship between voltage and gas pressure is to measure it. This is accomplished by pumping the system to maximum pressure, and then reading the voltage from the strain gauge meter and the pressure from the high precision Heise gauge. Measurements are repeated at intervals by lowering the pressure with a blow-off valve until the pressure goes to near zero.

Once all the measurements are taken, a linear fit is done. An example of experimental data and a linear fit is given in Fig. G.1.

G.2.2 Sample Gas Preparation

One of the more important concerns of the experimental setup is the purity of the sample gas. Before the sample cell is filled with the sample gas, a procedure has to be followed that prepares the gas system, which depends on whether the sample is ^{3}He or ^{4}He. The ^{3}He case is just an extension of the ^{4}He case, so I will consider ^{4}He first.

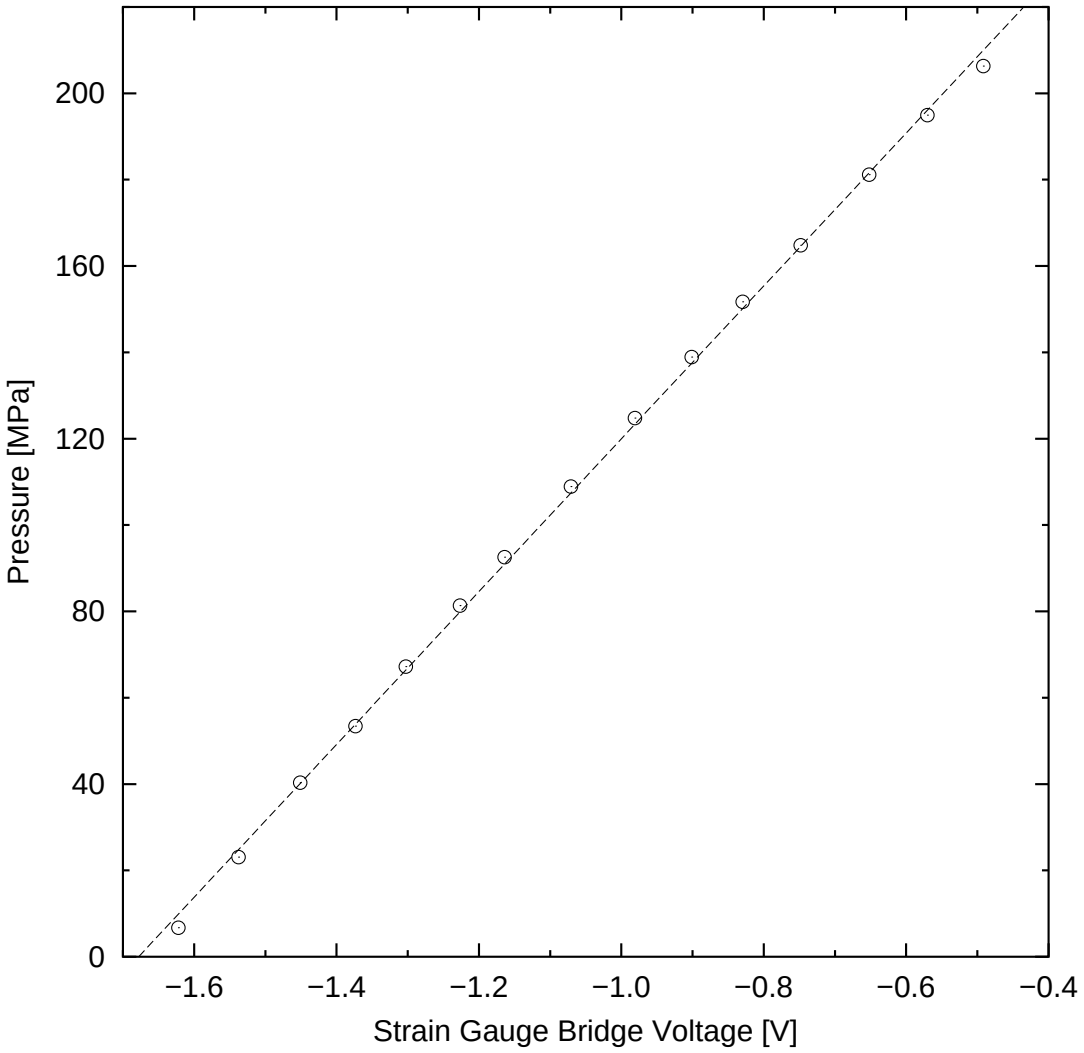

Figure G.1: A sample SGC calibration graph. It show the relationship of the voltage read from the strain gauge cell to the measured system pressure. The line is from a linear fit.

The first thing to do is pump out the system for at least a few hours, in order to get all the impurities (such as water) out of the system that may have crept in while in storage. The entire pressure system, all the way up to the helium bottle's valve, is pumped out. The system is then pressurized with high purity ^{4}He to the maximum pressure of the compressor. One lets it sit for maybe 15 minutes, then releases the gas to a pressure that is slightly above room pressure, so as to not allow anything back into the system. One then waits for 15 more minutes. This purging process is done up to five times. After the purging, the cold trap is filled with liquid nitrogen and the system is pumped up with ^{4}He again, to the desired pressure.

For the case of ^{3}He, a few more details must be attended to. Before the pumping out of the system, the ^{3}He and ^{4}He bottles need to be connected to each other and also to the fore of the compressor, so that the bottles don't need to be swapped after the system is purged. The pumping out and purging process is the same as for ^{4}He. The system is then pumped out again, then purged with ^{3}He at least once. At this point, with the pressure at a minumum, the cold trap is filled with liquid nitrogen. The system is then pressurized with ^{3}He to the desired pressure.

The whole process can take several hours. The reason for the 15 minute wait between the pumping up and the release of the helium is because of the small inner diameter of the tubing to the SGC, the PGC, and the sample cell. It can take several minutes for the gas to flow in and out of those areas. The reason one needs to wait until the final pump before the cold trap is filled, is that one wants to trap all impurities before they go into the sample cell, but if the trap is filled earlier, the trap fills up with contaminants that would otherwise leave in the purging.

For a ^{4}He sample, there should be no impurities in the sample cell at this point. For ^{3}He, the only impurities in the sample cell will be some residual ^{4}He, which will not freeze in the cold trap. In this case, the resulting crystal will have a small amount of the ^{4}He in it; if too much ^{4}He is in the crystal, serious problems of growing a good single ^{3}He crystal arise, as well as altering the experimental results from pure ^{3}He.

G.2.3 Pressure Stability

A major concern of the experiment is the pressure stability because it affects the quality of the crystal, once grown. If the pressure changes (most likely drops), the molar volume of the crystal changes, changing the parameters of the crystal itself, which is especially undesirable while in the

middle of a measurement. The pressure change can have an even worse effect of causing a good crystal to worsen.

One cause of instability is a leak in the system. This leads to the need of the pressure system being very leak tight. Another cause of instability is fluctuations of the temperature in the hutch, where most of the pressure system resides. A cause of this can be the opening and closing of the hutch door, if the temperatures inside and outside the hutch differ.

G.3 Orientation Access

After the Displex is mounted on the diffractometer, the orientational limitations of each of the four circles of the diffractometer need to be found. This is a two person job, where one person changes the motor positions while the other person watches the diffractometer. At the end of the job, the hard limits need to be set, which involves moving small pegs along the circles so they will come into contact with a limit switch when the motor is at the limiting angle. The software limits also need to be set.

Since the Displex juts out of the bottom of the ϕ circle around 20 cm, with two electrical connectors, two high pressure helium fittings (for the Displex), a vacuum fitting, and the sample gas line all coming out of it, there are many ways for the Displex to run into the diffractometer. The Displex limits values of ϕ and χ. As the Displex is rotated in ϕ, the connectors revolve around the base; at certain values of χ, the connectors will run into the diffractometer. This effectively means that the range in χ depends on the value of ϕ. The value of ϕ normally used is one where all the connectors clear the diffractometer, although it may be needed to be changed in the course of looking for a reflection. The next limitation of the motion in χ is the high pressure helium lines. These lines go between the Displex head and the compressor, and are very heavy and inflexible. Even if they are strung from the ceiling and have spiral plastic tubing segments, these lines will exert a strong pull on the Displex head itself when χ is changed too much, creating too much tension. Therefore, χ has to be limited to values where the tension is not too great. This discussion was based on the assumption that the diffractometer in general allows free movement over all χ values; if the χ circle is of the split ring type, there is a gap missing at the top to allow the beam to pass, limiting the allowable range of χ even further.

The theoretical limits for ω are $\pm 90^{\circ}$, although this is more like $\pm 85^{\circ}$if the χ circle is not the

split ring type. However, due to the close proximity of equipment, this range is more limited in real life. On the upstream side of the Displex, there is probably a flight path, slits, and an ionization chamber all very close; running into an of these would be devastating, since it would throuw off the entire alignment.

The 2θ arm has a flight path from the detector up to the scatter slits, and this could also come into contact with the χ circle. A collision of this sort makes the 2θ value inaccurate, as well as misaligning the detector slits. This type of collision depends on the position of both 2θ and ω, making it hard to compensate for.

The detector slits should never be closed completely, since the blades will come into contact. This can cause the center of the slit pair to change. Opening the slits too wide is also bad, since the motors lose steps when the slits stop opening, also making the center inaccurate.

G.4 Deadtime Measurement

This procedure was done only for the detector used to take the rocking curve data. It did not need to be done with the ionization chamber monitors, since the nonlinear range for them was not reached.

For detector count rates that are slightly into the nonlinear range of a detector, the deadtime correction is of the form

$$n_{\text{true}} = -\frac{1}{\tau}\ln(1-\tau\, n_{\text{obs}}) \simeq \frac{n_{\text{obs}}}{1-n_{\text{obs}}\,\tau} \tag{G.1}$$

where τ is the deadtime of the detector, n_{obs} is the measured count rate, and n_{true} is the true count rate.

The measurement of the detector's deadtime is done by measuring the count rate with both the detector and a flux monitor. This is done for the two cases of when the attenuator is in place and when the attenuator is removed. After the measurements, the detector count rates are normalized by dividing them by the monitor count rates. These measurements are done at several different base intensities by varying the incident flux.

Several definitions need to be made. The normalized count rate where the attenuator is not in place is n_{NO}. The normalized count rate where the attenuator is in place is n_{AO}. The true count rate for the no attenuator case is n_{NT}. The true count rate for the attenuator case is n_{AT}. Using

the ratios

$$R_{\mathrm{O}} \equiv \frac{n_{\mathrm{AO}}}{n_{\mathrm{NO}}} \qquad \text{and} \qquad R_{\mathrm{T}} \equiv \frac{n_{\mathrm{AT}}}{n_{\mathrm{NT}}}\,, \tag{G.2}$$

Eq. G.1 becomes

$$R_{\mathrm{O}} = R_{\mathrm{T}} + \tau(1 - R_{\mathrm{T}})\, n_{\mathrm{AO}}\,. \tag{G.3}$$

This is a linear relationship of the form

$$R_{\mathrm{O}} = M n_{\mathrm{AO}} + B\,, \tag{G.4}$$

where the slope (M) and the offset (B) are

$$M = \tau(1 - R_{\mathrm{T}}) \qquad \text{and} \qquad B = R_{\mathrm{T}}\,. \tag{G.5}$$

If M and B are solved for τ, the result is

$$\tau = \frac{M}{1 - B}\,. \tag{G.6}$$

So, in order to calculate the deadtime τ, a linear fit of the measured data needs to be made, where the slope and offset are plugged into the last equation.

Only one attenuator can be used, where the best results come from an attenuator which has an absorption being roughly 0.2. The best way to get a good deadtime value is to take measurements with several different attenuators at each different intensity. The values measured for an attenuator can be paired with the values of a weaker attenuator, with the weaker set being used as the "no attenuator" values. This will give many cross checks.

The way to have an adjustable incident intensity is to position the detector at a location of a beryllium powder ring. By moving the detector either closer to or further from the ring maximum, a variable source, which is stable, is created. The maximum intensity used with no attenuator present should correspond to the maximum count rate used during the experiment.

G.5 Attenuator Measurement

Accurate measurement of the absorptions of the attenuators is important since these values are critical when determining $\langle u^2 \rangle$ values. This section assumes that all measurements made with the detector are corrected for the dead time.

The process of measuring the absorption of an attenuator is simple. A detector downstream of the attenuator and a monitor upstream of the attenuator are used. With the attenuator removed and the beam shutter opened, the detector and the monitor count for a certain gate period, with the detector count then being divided by the monitor count (normalization). This same process is done a second time while the attenuator is in place. The absorption is then found by dividing the normalized detector count when the attenuator was in place by the count when the attenuator wasn't in place. This process is repeated for all the attenuators used.

The detector used for the rocking curve measurements was the detector normally used for these measurements. This might seem to be at cross purposes, since the reason attenuators are used is that the rocking curve detector's dynamic range is not as good as the range of peak intensities; the attenuators are used to scale the brighter reflections down into the detector's range. The way to get around this conundrum is to only use attenuators with small enough absorptions that can be measured with the detector, and then use a multiple of them, instead of one thick piece. The individual attenuator pieces used for this thesis never had an absorption less than 10^{-3}.

The measurement assumes that a reasonable number of photons are striking the detector when there is no attenuator present, but not too many such that the detector is saturated. The incident beam can't be used, since it will destroy the detector. There is also the problem that the photon flux after the monitor needs to be constant. The detector can be brought to the fringes of the incident beam, so only a small portion of the photons are detected; this method is bad since the stability of the fraction of the photons hitting the detector changes as the beam moves slightly over time. If a crystal is in the sample cell, a reflection could be used by going to the reflection's position and using the peak's intensity for the measurement; this is not ideal, since this implies that the crystal is stable, and that is a bad assumption to make for helium crystals. The best method is to move the detector to one of the beryllium powder rings' positions (see Appendix C), and use it as the stable flux source.

Once the beryllium ring is found, the count rate needs to be set to the maximum value for the

detector when the attenuator is not present, giving the best statistics. This fine control is done by moving either closer to or further from the peak of the beryllium ring. If the ring is not strong enough, a different ring may be needed.

G.6 Background Measurement

G.6.1 Scanning Measurement

Before the run begins, a background scan over 2θ's range while the Displex is in the horizontal position ($\chi = 180^{\circ}$) needs to be taken. This records any diffraction taking place other than that from helium crytals. This should be done when there is liquid helium in the cell, with the temperature just above freezing; the conditions should be as close to actual data taking conditions as possible. Also, the detector slits should be opened wide horizontally and narrow vertically, such as 1 mm vertical by 8 mm horizontal. A sample scan can be seen in Fig. G.2.

It needs to be remembered that the detector will only see what the two sets of slits on the detector arm allow it to see the immediate vicinity of the sample crystal. Because of the way the two sets of slits are set, the only places diffraction can come from are the sample cell itself and anything that has frozen on the outside of the cell. The expected 2θ peaks corresponding to Be and BeO powders will be present, with the positions being predictable since the crystalline structures and lattice parameters for Be and BeO are known (see Appendix C). It is useful to index the expected Be and BeO peaks against the actual peaks, so as to make sure that there are no extra peaks.

The reason that this scan needs to be made is to have a rough map of potential problems in 2θ in case one of the desired helium reflections is at the same 2θ value as a peak on this scan. This is invaluable at high Q where the helium peaks are of the same magnitude as the background peaks. In practice, the Be and BeO peaks will be in the same place at different runs, but the strength of the diffuse background can vary widely, and strange peaks in the background occasionally occur.

G.6.2 Picture Taking

Another type of beryllium background measurement involves taking a picture of the background rings. A Polaroid [1] is mounted on the incident end of the detector arm, with the arm being at

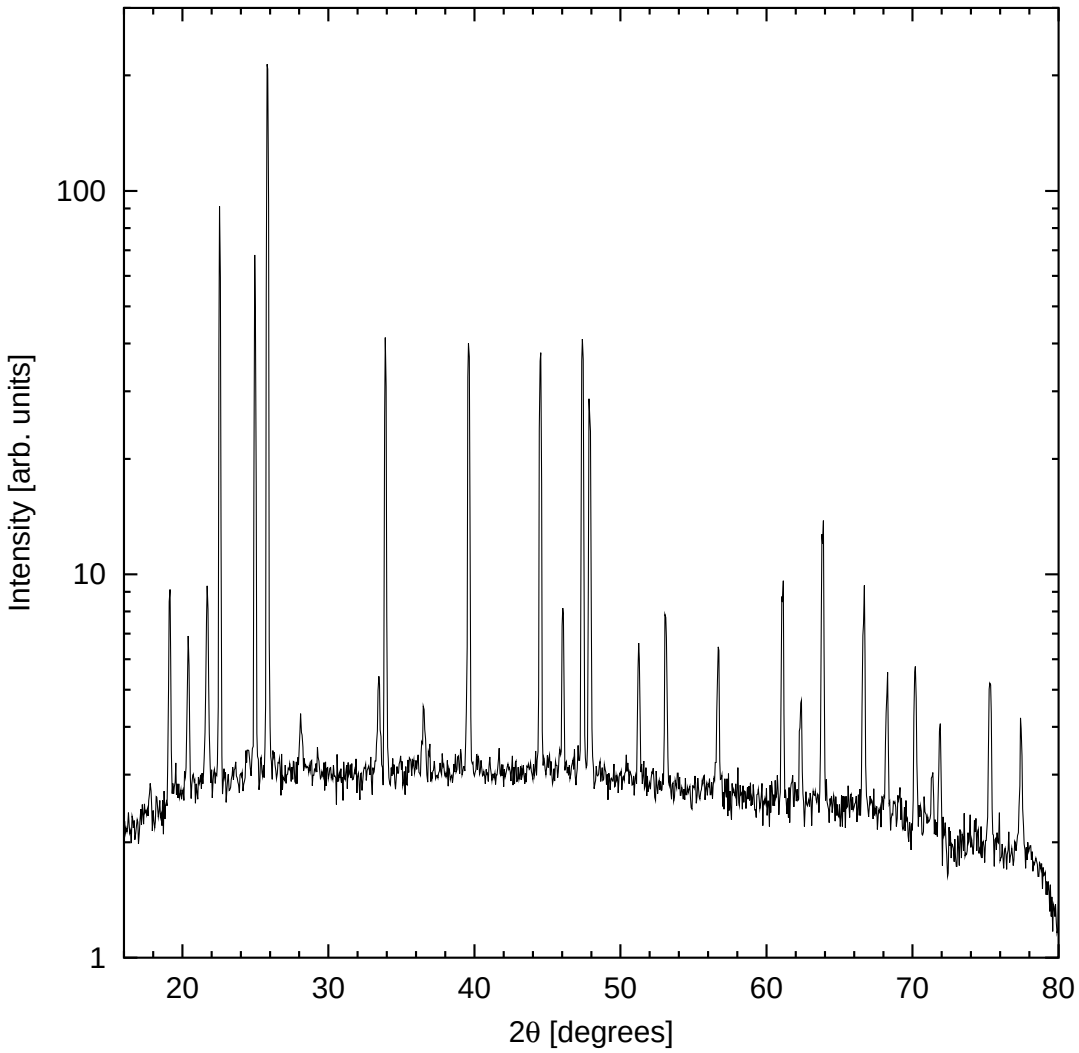

Figure G.2: Background Scan for the 1996 NSLS beamtime. The intensity scale is logarithmic so the weaker peaks can be seen easier. The peaks correspond to Be and BeO reflections for 16.0 keV photons.

roughly 20°. The beam shutter for the hutch is opened for a few minutes, exposing the Polaroid, and is then closed. The Polaroid film is removed and developed. The picture should be of white rings on a black background, with the rings appearing to be doubled.

The doubling of the rings is due to the fact that the beam passes through the beryllium cell wall twice. The physical separation of these two walls creates two separate cones of radiation, with the upstream cone belonging to the first cell wall. These slightly offset cones will strike the Polaroid twice, creating the doubled ring.

Simple geometry is used to get the approximate 2θ angles of the rings. The distance from the center of the sample cell to the Polaroid needs to be known. Using a compass, one finds the center of the rings. The distances of the rings from their center are then measured. A rough value for 2θ is generated using

$$\tan(2\theta) \approx \left(\frac{\text{ring-to-center distance}}{\text{cell-to-picture distance}}\right).$$

By comparing these 2θ values to the theoretical values for Be reflections (see Appendix C), each ring should be able to be matched with a reflection. BeO rings normally aren't strong enough to appear, so they are ignored.

The background scan (described in the last section) can be useful when used with the Polaroid, when the ring on the picture is matched with a peak on the scan, using the determined reflection indices. The scan gives the relative magnitudes of the rings, which a Polaroid can't. The scan also gives actual 2θ values for each of the rings, instead of estimated values.

This picture will be used later to help index crystal peaks. Similar pictures will be made after crystals are grown, where reflections will also show up. In order to roughly identify the 2θ values of the crystal peaks, the indexed Be rings are used as guides.

G.7 Crystal Growth

When growing the crystal, it is hoped that it will be single and perfect. This does not always happen, although the crystal may still be usable: this depends on how bad (as defined later) the crystal is.

The growth of a good crystal is somewhat of an art, with the procedures used being based on many trials and errors. What works at one beam time seems not to work at the next beam time.

There is also no way to grow a crystal that is oriented in a particular direction; the direction a crystal takes is random (with a slight exception for hcp, which is explained later).

G.7.1 Considerations

To understand how a crystal used for this thesis was grown, the thermal gradient in the cell needs to be understood. In the Displex setup, the fill line is a direct connection from the sample cell to the outside, making it a conduit of heat to the sample cell. On the other end of the cell, the Displex cold finger absorbs heat from the sample cell. This causes a thermal gradient along the cell's axis, with the temperature increasing the further along the cell from the cold finger. For the rest of this section, the **z** direction is defined as along the cell axis, with the positive direction being away from the cold finger.

Assuming that the temperature at any point on the cell is wholly dependent on its z position, there will be a z value of the cell where the temperature is at helium's freezing point as the temperature is being lowered. This point's z value will increase with time, moving away from the cold finger, and any helium between this point and the cold finger will be frozen. This shows that the crystal is grown in a gradual process from one end of the cell to the other, which has the capacity to grow a nice crystal. In order to increase the thermal gradient along the cell, a current can be passed through the fill line heater, causing the fill line to warm up further; this can be useful at times.

If the temperature along the cell's cross-section at any z position is uniform, the crystal could grow unevenly and crookedly, increasing the chance a fractured crystal will form. This is avoided by having a uniform wall thickness for the cell and making sure nothing touches the cell along the walls, which would cause a hot or cold spot.

There is a side effect of the heat gradient when a hcp crystal is grown. An hcp helium crystal grows with its c-axis perpendicular (within a few degrees) to the thermal gradient and thus also to the cell axis. This limits the possible crystal orientations to two degrees of freedom, simplifying the indexing of the complex hcp crystal.

When growing any crystal, the slower it is done, the better the chance in creating a single crystal. Therefore, a bad growth plan is simply turning on the Displex, letting the temperature drop immediately to its minimum.

G.7.2 Freezing and Melting Signature

When the crystal forms, there is a signature on the logs that records the event, thus giving the freezing temperature. One uses the pressure values from the strain gauge cell and the temperature values from sensor B.

The molar volume of the liquid at freezing is larger than the molar volume of the solid. So when the solid forms, less volume is used, causing the pressure of the remaining gas to drop. Since the SGC is very sensitive, it is able to detect a pressure drop as small as this.

As a crystal is grown, the cold finger removes heat from the helium sample. Once solid starts to form at the freezing temperature, the heat removed is the heat of melting for the helium, causing the temperature to stay at freezing until the crystal is done growing. On the log, the temperature drops until the solid starts to form. At that point the temperature becomes constant for a short period (a temperature plateau) while the crystal grows, after which the temperature begins dropping again.

These two effects happen simultaneously, with the pressure dropping at a constant rate during the freezing process. The pressure drop is the freezing sign watched for. Once it occurs, the temperature plateau is watched, with it's temperature value being the freezing temperature.

If the liquid helium is extremely pure, it can supercool to a temperature below equilibrium freezing. At some point, the crystal will then begin to form, with the temperature quickly jumping back up to the freezing temperature. The pressure initially drops quickly before decreasing at a linear rate as the crystal forms. Figure G.3 shows the freezing signature of a ^{4}He crystal which supercooled before freezing.

From the freezing temperature of the crystal, the thermodynamic relations (see Appendix D.2) can be used to get the pressure of the system.

G.7.3 Annealing

One way to try to heal a badly fractured crystal is to try to anneal it. This is done by bringing the temperature of the crystal to just below freezing, and letting it sit. Hopefully the pieces of the crystal, being soft, will merge together into a larger, nicer crystal.

This is nice in theory, but hard to get to work in practice. If the crystal is very bad, it can take forever to anneal to a better version. Even after annealing, more times than not, it is still a multicrystal, with the crystals now only slightly out of alignment; sometimes these crystals are

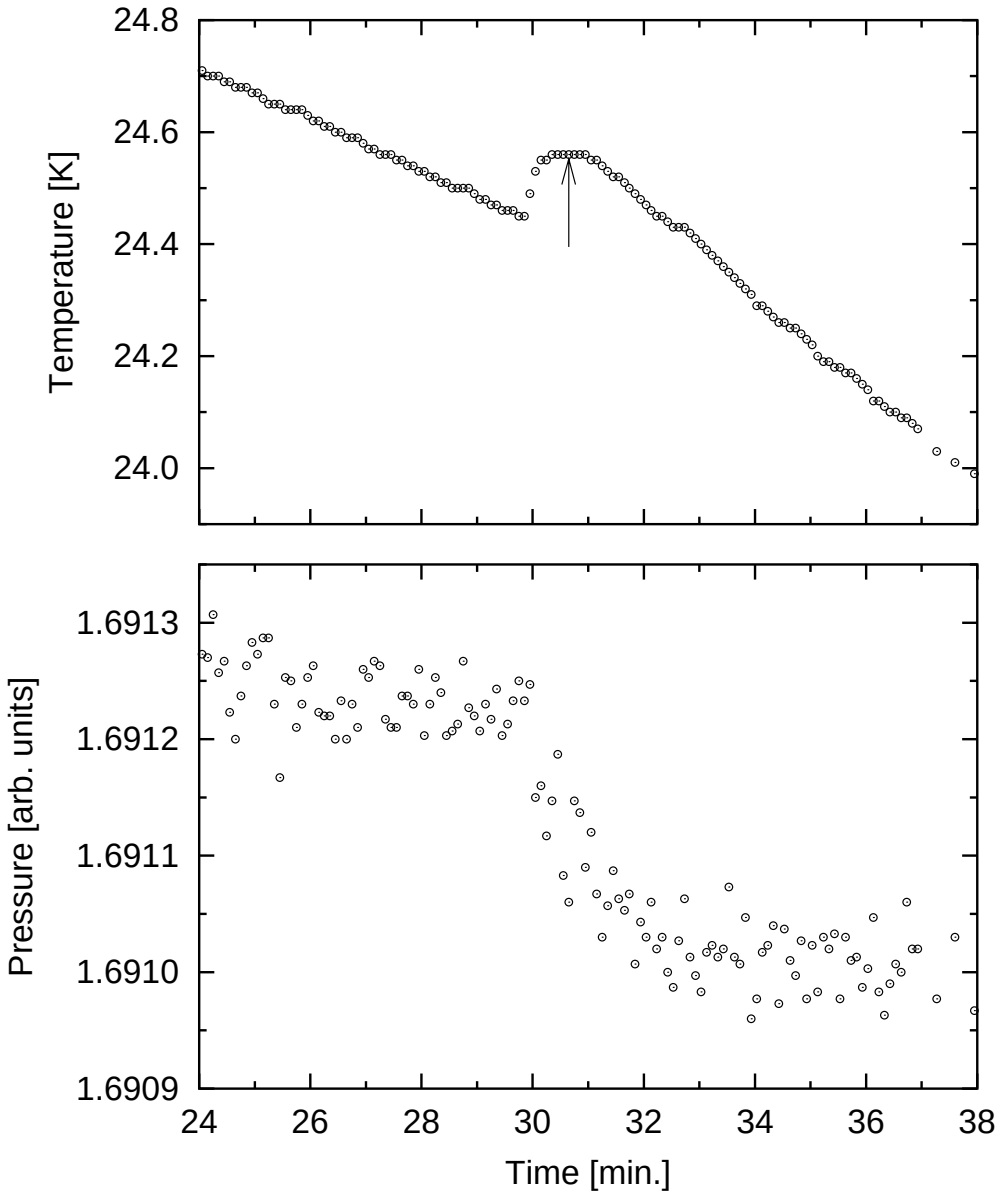

Figure G.3: Freezing signature for a ^{4}He crystal which supercooled. The top graph shows the temperature of the crystal. The arrow points to the temperature plateau, corresponding to the freezing temperature of the crystal. The bottom graph shows the pressure of the helium in the system.

usable.

Part of the problem is that the crystal is never one temperature, since there is always a thermal gradient across the sample cell. So, it is impossible to have the whole crystal just below the freezing temperature to anneal.

G.7.4 Actual Growth Practice

There are several methods described here for growing crystals. Not all methods used are described here, since some methods don't seem to work every time.

The normal method used is to lower the temperature of the helium liquid to a few degrees above freezing. The temperature controller is then programmed to ramp the temperature down slowly, at maybe 3 K/hour. Normally this grows a good crystal. The problem with this method is that the temperature reduction is actually in small steps, making the logged temperature value zigzag. This can mask the freezing signature when looking for its temperature plateau, since each temperature step makes its own plateau. The key to overcoming this is to either take very small steps or to not grow crystals very slowly.

When it comes to growing an hcp crystal, it sometimes helps to increase the temperature gradient across the sample cell, since hcp crystals prefer to grow with the c-axis perpendicular to the thermal gradient. This is done by allowing some current through the fill line heater.

Another way that has been shown to grow good crystals is to quickly grow a crystal; this crystal will be bad, but that does not matter. The temperature is allowed to go to 0.25 K below the freezing point. Current is passed through the fill line heater, warming up the cell and melting the crystal. After raising the temperature around 5K above melting, the heater is turned off, and the crystal is allowed to freeze again. This time, the freezing process is very gradual, since the set point of the Displex is just below freezing. This method creates a good freezing signature, since the transition is very smooth. The reason for going so far above the freezing temperature is to make sure that the crystal has completely melted, leaving nothing to act as a seed.

G.7.5 Crystal Care

Once a crystal good enough to use is grown, it has to be treated carefully, in order to keep it from losing its quality.

The temperature of the crystal should not be changed unless necessary, since a change can cause the crystal to degrade or even alter its orientation. A sudden temperature change can be disastrous. When a temperature dependent measurement needs to be made, temperature changes should be made very slowly.

Another concern is a change in pressure. It can make the crystal fracture. It can also move a crystal boundary near the path of the X-ray beam, decreasing (or increasing) the intensity of diffracted peaks. These pressure changes can come from the change in the amount of helium frozen, or from the change of the pressure of the gas in the gas handling system.

As time goes by, the crystal will keep changing and moving slowly. After each day of a crystal's existence, it is a good idea to re-center all the peaks, since their positions will be slightly different. Sometimes the moving of the peaks is quicker than normal, requiring the re-centering be done every few hours; when this happens, something drastic is probably about to happen, such as the peaks simply vanishing as the crystal realigns.

G.8 Crystal Orientation and Peak Hunting

Orienting the crystal is a tedious and time consuming process. Since a characterized helium crystal can't be brought to the beamline, orienting has to be done while online. Orienting becomes more complicated when the crystal is fractured, making the process harder. If the crystal is very bad, orienting it is impossible. The quality of a crystal depends on the number of crystal fractures and the sub-crystals' relative orientations. The orientation of the crystal is determined using a computer through the creation of an orientation matrix.

This experiment needs as many reflections found as possible. Finding a reflection means centering on the associated peak and recording its position. Sometimes finding a peak is impossible due to the peak being too weak; or it is at an orientation which is inaccessible to the experimental setup, due to physical limitations.

The usefulness of the orientation matrix of a crystal is that it can be used to find peaks quickly and easily. However, in order to create a matrix, several peaks need to be found. Since the use of the matrix helps find peaks, and finding peaks improves the matrix, they are done almost simultaneously, with the reflections being found in order from low Q to high Q. At the end of this process, a high quality orientation matrix is finished, which is used to find every peak possible.

The low Q peaks are extremely bright and relatively easy to find, which is good, since they have to be found without any help from a matrix. Once enough reflections are found, the matrix is created on a computer. This matrix is rather inaccurate, but good enough to help find the next larger Q reflection. Once this reflection is found, the matrix is redone using the additional information, making it more accurate, which makes it easier to find the next reflection. This process is done over and over, until all the available reflections are found; without this method, it would be virtually impossible to find high Q reflections, since they are so weak in intensity.

G.8.1 Considerations

There is crystal movement and annealing to consider with helium crystals. When peaks are found, several things might happen over time. The peak positions could slowly start changing, and they have to be followed by recentering on them (sometimes this has nothing to do with the crystal, but is caused by the loss of steps by the stepper motor that moves 2θ, ω, χ, or ϕ). The peak shapes are many times less than ideal, which is not a problem, but they sometimes change shapes over time. This can cause the center to move or cause the integrated intensity to change; sometimes the intensity of the peak suddenly increases or decreases. There is no way to stop these things except grow a better crystal, since these afflictions seem to endlessly haunt bad crystals.

One reason for the movement of peaks is that the crystal can slowly rotate, due to the cylindrical symmetry of the cell and the fact that the crystal is relatively soft. Another cause of these problems is that the boundary between sub-crystals moves, as one grows and the other shrinks. If the crystals have vastly different orientations, the integrated intensity will change; if the crystals are slightly different in orientation, the shape or intensity of the peak may change, but normally the integrated intensity of the peak stays the same.

Since the crystals grown can come in all types of qualities, from perfect to very bad, there has to be some sort of criteria that determine whether a crystal is acceptable or not. This is important, since it's easy to spend a large amount of time on a bad crystal, only to have the resulting data make no sense.

If the crystal is fragmented and has regions that are aligned very differently in the X-ray beam path, the problem of identifying which peaks belong to which crystal arises. It is fairly simple to check for the existence of this problem when a Laue rotation picture of the crystal is taken. On

the picture, if there are multiple spots at the same radial distance from the center of the beryllium rings with different shapes and sizes, this most likely exists; the same is true if the spots seem to come in matching sets periodically about the circle. If a narrow ω range was used when taking the picture, this makes few spots appear, making it harder to judge the crystal's quality. Fragmentation shouldn't be too much of a problem if one of these sub-crystals has peaks that are much brighter than the peaks from the other sub-crystals, and if the peaks aren't bad, which is discussed later.

If enough reflections can be found in order to create a matrix, the qualities of the peaks needs to be considered. In order to do an integrated intensity scan, a rocking curve (scan in ω) has to be done. Since ω changes during the scan, it does not matter too much if the peak is wide or imperfect in ω; the integrated intensity is found by simply summing the area under the scan. However, if the peak has extremely long tails or is extremely bumpy and wide, there will be problems in taking the scans. Since the entire peak is needed for integration, it's arbitrary where to stop taking data when the tails are very long, since the level of the background takes a long time to reach. With such a scan, the amount of background is not known. This makes subtraction harder, which must be done using background scans taken when the crystal is melted.

The last thing to consider when determining the crystal's quality is the profile of a χ scan. Since χ is stationary during a rocking curve, the χ scan width shouldn't be very wide. The width of the peak is caused by fragments of the crystal having slightly different orientations, with the peaks being at slightly different χ values. If the peak is larger than a degree, it probably won't yield great data. Normally, with peaks that big, the reflection has several sub-peaks to it, and the tails never really seem to die off. There is also the danger with χ that the scanned peak is far enough away from a different peak which is not be seen during a scan, but is close enough to confuse searches for the peak corresponding to a certain sub-crystal. This case gets even worse for different reflections, since the distance of the peaks in χ from one another changes, and they can actually overlap. If the χ scan is not fairly clean, it is a smart idea to just start again.

G.8.2 Crystal Orientation Matrix

The goal of orientation is to find enough peak centers (and their associated angular values) that a crystal orientation matrix can be set up. The matrix will then give the motor coordinates of any other reflection specified. The matrix is manipulated through computer software, since it can be

rather complex.

Ideally, three correctly identified reflections are used for creating a matrix. No two of these reflections should be colinear through (0 0 0). These three reflections will determine values for the crystal's lattice parameters and Euler angles (see Appendix B.1). If they come out different from what is expected, chances are that either the indices entered for one of the reflections are wrong, or the reflections are coming from two different crystals.

Only two reflections can be used to create the matrix, if the Euler angles and the estimated lattice parameters are given. In this case, the reflections only determine the crystal orientation. This is simpler since only two reflections need to be found, but the three reflection method is superior since it automatically shows you if the peaks found are usuable.

In practice, two reflections are first found using the brute force method (described in Appendix G.8.3). A matrix is then made from the motor values and the theoretical crystal structure information. This helps finding a third reflection, which should be bright and have a low Q. It still needs to be found using the same brute force method as before, since this rough matrix gives only approximate coordinates for the reflection. Once the third reflection is centered, all three reflections are used to create a new matrix based only on the direct experimental data. The validity of the new matrix needs to be checked, comparing the resultant crystal characteristics against the expected ones. If there is a problem, it has to be fixed.

At this point, the matrix is hopefully good enough to start predicting the next higher Q reflection's position. The motors should be moved to the position that the matrix predicts for the next reflection. The fine centering procedure (described in Appendix G.8.3) should then be done, until the peak is found and centered. A new matrix is then made, utilizing this new reflection, which is more refined than the last. This process is repeated for more reflections, although a new matrix doesn't need to be made after every peak once the matrices become somewhat accurate.

At some point, the reflections are so weak that even with a good matrix, a good deal of tweaking with the motor values is needed before any sign of a peak is seen. At these large values of Q, small background peaks can be easily mistaken as reflections if they are close to the predicted position.

There is a way to get certain high Q peaks quickly, in order to make a better matrix faster. It starts with a low Q peak, of some order m as expressed by $(mh\ mk\ m\ell)$, which has related n-order

peaks of the form ($(n/m)h$ $(n/m)k$ $(n/m)\ell$), some of which are allowable by the structure factor; both n and m are non-zero integers. An n peak has the same χ value as the m peak. The ω and 2θ values for the n peak are derived from the m peak by the relations

$$\omega_n = \omega_m + \delta \qquad \text{and} \qquad 2\theta_n = 2\theta_m + 2\delta\,,$$

where δ is an angular parameter. This means that the n peak can be found by making a radial scan; a scan where, for each step, 2θ moves twice the angular distance that ω moves. An easier way to find these peaks is to consider Bragg's Law; since the n and m peaks come from the same sets of planes, the lattice spacing d used for both peaks is the same. This means that

$$d = \frac{m\lambda}{2\sin(\theta_m)} = \frac{n\lambda}{2\sin(\theta_n)} \qquad \text{resulting in} \qquad \sin(\theta_n) = (n/m)\sin(\theta_m)\,,$$

which gives θ for the n peak. The resulting values for 2θ and ω are then

$$2\theta_n = 2\arcsin((n/m)\sin(2\theta_m/2)) \qquad \text{and} \qquad \omega_n = \omega_m + (1/2)(2\theta_n - 2\theta_m)\ .$$

Once the peak is then found, it has to be fine-centered.

This last method can't be used to create an initial matrix from only one peak which was found with the brute force method. As mentioned before, when created with two or three reflections, the matrix can only use reflections that are not colinear through (0 0 0). This means that n and m order peaks of the same lattice spacing can't both be used; the peak with the highest Q should be used. Once a matrix is created, both peaks can then be used.

G.8.3 Finding and Centering on Reflections

The whole brute force method of both rough and fine centering works for low Q only. This is because it depends on taking pictures of the reflections, and these pictures capture only low Q reflections. For higher Q reflections, the crystal orientation matrix is used to get a rough idea of the peak's center in terms of the motors; once the motors are set to the approximate position, the method for fine centering is followed.

Rough Centering

A Laue rotation picture is first taken of the crystal. A Polaroid [1] is mounted on the front end of the detector arm, making sure it is straight and noting the orientation in which it is mounted. 2θ is then set at around 20°, and ω is set to the lower bound of the scan. The shutter to the hutch is opened, exposing the Polaroid to the diffracted X-rays. ω is moved to its upper bound and then back. Depending on the flux of the incident beam and the speed of the motors moving ω, ω might have to be moved back and forth several times. Once this is done, the shutter is closed and the film is developed.

The Laue picture used is generated from the rotating crystal method (with stationary film) [2]. Since the X-ray beam is monochromatic and the sample is not polycrystalline, the chance of Bragg's Law being met for some set of planes is small. To compensate for this, the sample crystal is rotated, allowing the angle between the beam and the lattice planes of the crystal to vary. At different times and for different planes, Bragg's Law is met, creating a spot on the film if the Polaroid is in the diffracted beam's path.

The picture should show beryllium rings with small white spots, which correspond to reflections. Knowing the 2θ values of the beryllium rings from the background picture taken earlier (see Appendix G.6.2), the beryllium rings act as a guide for getting an approximate 2θ value for any given spot. Also, knowing the pressure of the system, either directly from the Heise gauge or indirectly through the freezing temperature and the use of thermodynamic relations, a molar volume can be determined. Assuming that the phase of the crystal is known, this molar volume can be used to get approximate lattice parameters for the crystal, which are then used to generate a table of expected 2θ values for the reflections. With this information, it shouldn't be hard to identify the reflections that spots correspond to, unless the solid is close to an fcc-hcp transition line, where the phase may need to be determined from the spot patterns. Once a spot is associated with a reflection, the 2θ angle of this reflection is approximately known, and 2θ should be set accordingly.

The spot of the desired reflection needs to be on a line running from the center of the rings to the top of the picture (corresponding to the plane of the detector itself) or it won't be seen by the detector. The moving the of the spot to that line is done by moving χ. Using a protractor and the beryllium rings as guides, the angle between this line and the reflection is measured. This

resultant angle is the value that χ needs to be moved in order to get the reflection in the plane of the detector. It is important to remember the orientation of the picture as it is mounted, and to mount the Polaroid straight, in order to move χ in the right direction and by the right amount.

The last angle needed is the ω angle, but since the crystal was rotated in ω as the Polaroid was exposed, the correct value could be any value of the rotation. There is a small chance that a change in χ moved the reflection out of the ω range, but this is a small chance, and it can be checked by simply taking a new picture at the new χ value.

When trying to find the correct ω, the detector slits are opened wide, the beam is let into the hutch, and a ω scan is taken over the entire range that was used for the picture. Hopefully, a peak of some size will be seen. Since the scan is in ω, not 2θ, any peak seen should be from the helium crystal. If a peak is seen, ω is set to that value.

If a peak is not found, another way to find a rough value for ω is to put a fluorescent screen at the entrance to the detector arm, mount a CCD camera that is aimed at the screen, turn off the lights in the hutch, and then let the beam into the hutch. ω is varied over its range while the fluorescent screen is watched. Hopefully, a bright flash will be seen where ω fulfill the Bragg conditions; ω is then set to this value. This method can sometimes be helpful.

If the correct ω value is still not found, the next thing to do is make sure the peak is lined up in χ correctly. This is done by taking another photo and checking the spot's position. Another scan in ω is done, looking for a peak. If one is still not found, both 2θ and χ need to be tweaked, taking ω scans after each tweak. Eventually, the peak is found, and ω is set to that value.

At this point, the reflection is roughly centered.

Fine Centering

This procedure assumes that the peak of the desired reflection has been found, most likely during an ω scan. It is assumed in the following discussion that anytime a peak is scanned, the corresponding motor of the scan is set to the location of the peak's maximum.

The detector slits should be opened wide at this point, such as 2 mm vertically and 5 mm horizontally, with no attenuators in use yet. During the course of centering, the intensity will increase in magnitude enormously. Attenuators will have to be inserted in order to keep the detector from saturating, since oversaturation is harmful to the detector and the resulting output

is unreliable. This will probably need to be done several times. With low Q peaks, a small change in a motor's position can instantly cause a several order of magnitude change in intensity, causing the experimenter to quickly close the beamline shutter.

The first thing to do is to a quick scan in 2θ, again looking for a peak. The peak is very sharp since 2θ directly depends on the lattice spacing; the peak should be around 0.05 degrees wide. This should be done first, since a sharp gain in intensity normally results.

The next thing to do is take a χ scan, which is useful in determining the quality of a crystal. Typically, peaks in χ are on the order of a degree. If the crystal is fractured, it will normally appear in χ as two or more peaks; it is important to take a wide scan, since a larger peak may be off to side of the current peak, which would indicate that the current peak belongs to a smaller sub-crystal. Going to the larger peak is not automatically the thing to do, since the two sub-crystals are misaligned enough such that the integrated intensity scans will probably not catch the intensity of both peaks. If this is the case, the crystal might need to be abandoned. Even if the peak is singular, if it is much wider than a degree, the crystal is probably worthless; normally, peaks this large are actually the sum of several peaks, indicating a highly fragmented crystal.

An ω scan is then taken. Normally, this peak's width is around 0.1 degrees for a single crystal, and can be quite large if the crystal is fractured, being around a degree. A misshapen peak is not a real problem, since it gets integrated when the measurement data is analyzed. If the peak is misshapen, one thing to watch for are tails that seem to go forever; the width of the peak needs to be small since the time it takes to make high quality rocking curves increases linearly with the width of the peak. If the tails are very long, the crystal promises to be a great deal of trouble.

The final step calls for narrowing the detector slits for the final centering, to around 0.5 mm by 0.5 mm. Three scans are then made, one for 2θ, χ, and ω as before, centering after each. The resultant centered position is then the final value of the reflection's position, to be used in the orientation matrix.

G.9 Data Taking

Integrated intensity measurements are done by making a scan in ω; such a scan is called a rocking curve.

For a given crystal and temperature, it is normal to take measurements for all found peaks. If

there is not enough time, the best strategy is to take data for the highest and lowest Q reflections, giving a wide range in Q, which gives the best slope for a linear fit.

Before taking the measurement for a reflection, the peak should be quickly recentered, in case the position shifted. After this, the detector slits are opened wide (around 2 mm vertical and 5 mm horizontal), which is required when taking an integrated intensity scan [3].

A quick scan in ω is taken in order to judge the limits of the peak, so the width of the final rocking curve can be set. It is important to get all of the tails and some of the flat background; this linear background is useful when the time comes to remove it. Also, an attenuator should be inserted that allows the intensity at the peak's center to be just under the detector's maximum desirable count rate; the signal should not be suppressed more than needed.

The rocking curve is then taken. The scan is taken with steps of 0.001 degrees for a narrow peak, and with larger steps for wider peaks. The time gate used is around 2 seconds for low Q peaks, 5 seconds for middle Q peaks, and 10 seconds for high Q peaks.

G.10 Background Measurement For Individual Scans

After the data measurements are all done and the crystal is melted, background measurements of the cell need to be made at the same positions that the data scans were made. The measurements need to be taken at just above melting temperature for the crystal, so as to not melt anything else that may have crystalized inside or outside of the cell. Ideally, the background measurements are taken immediately after the crystal is melted, so as to capture the exact conditions for the data measurement. Over time, there is a possibility that something could freeze on the surface of the cell or some other unforseen circumstance that would make the conditions different later.

A quick preliminary scan should be made. This is done in order to see if the background is completely linear at that position, and also to make sure that the measured peak was not actually a background peak. If the background is nonlinear at that position, a more detailed scan mimicking the peak measurement is taken; this background scan is subtracted from the measurement scan later.

References

[1] Polaroid 57, high speed, 4x5 instant sheet film.

[2] B. E. Warren, in *X-ray Diffraction* (Dover, New York, 1990), Chap. 7.

[3] B. E. Warren, in *X-ray Diffraction* (Dover, New York, 1990), Chap. 4.

Vita

Dohn Arms was born on December 15, 1970, in Melbourne, Florida. He received his secondary education at Eau Gallie High School in Melbourne, Florida, graduating in May 1988. He enrolled at the University of Florida in August 1989, and worked at Los Alamos National Laboratory during the summer of 1992. He received a B. S. in Physics with a minor in Mathematics from the University of Florida in May 1993, and was accepted into the honor society of Phi Beta Kappa. He joined the Physics department of the University of Illinois, Urbana-Champaign as a graduate student in August 1993, and held a teaching assistantship for two years. In May 1995, he received an M. S. in Physics from the University of Illinois, and held a research assistantship thereafter. He is a member of the American Physical Society. He has been a user at several scattering facilities: the Advanced Photon Source at Argonne National Laboratory, the National Synchrotron Light Source at Brookhaven National Laboratory, the European Synchrotron Radiation Facility (Grenoble), DORIS at the Deutsches Elektronen-Synchrotron (Hamburg), and ISIS at Rutherford Appleton Laboratory (Chilton, UK).

He is coauthor of several papers:

M. W. Grant, P. F. Lyman, J. H. Hoogenraad, B. S. Carlsward, D. A. Arms, L. E. Seiberling, and F. Namavar, "Fabrication and Characterization of Thin Self-Supporting Germanium Single-Crystals", J. Appl. Phys. **73**, 2486 (1993).

A. Lacerda, R. Movshovich, M. F. Hundley, P. C. Canfield, D. Arms, G. Sparn, J. D. Thompson, Z. Fisk, R. A. Fisher, N. E. Phillips, and H.-R. Ott, "Doping and Pressure Studies on YbBiPt", J. Appl. Phys. **73**, 5415 (1993).

R. Movshovich, A. Lacerda, P. C. Canfield, D. Arms, J. D. Thompson, and Z. Fisk, "Investigations of the Nature of the 0.4 K Phase Transition in YbBiPt", Physica B **199**, 67 (1994).

C. Seyfert, D. A. Arms, H. Sinn, R. O. Simmons, and E. Burkel, "Phonon Spectroscopy in Solid Helium Using X-rays", Czech. J. Phys. **46 (Suppl. 1)**, 471 (1996).

M. Schwoerer-Böhning, A. T. Macrander, and D. A. Arms, "Phonon Dispersion of Diamond Measured by Inelastic X-Ray Scattering", Phys. Rev. Lett. **80**, 5572 (1998).

M. Schwoerer-Böhning, A. T. Macrander, P. M. Abbamonte, and D. A. Arms, "High Resolution Inelastic X-ray Scattering Spectrometer at the Advanced Photon Source", Rev. Sci. Instrum. **69**, 3109 (1998).

C. Seyfert, R. O. Simmons, H. Sinn, D. A. Arms, and E. Burkel, "Study of the Lattice Dynamics of Hexagonal Close-packed ^{3}He and ^{4}He Using Inelastic X-ray Scattering", J. Phys.: Condens. Matter **11**, 3501 (1999).